MODELING AND SIMULATION OF FREQUENCY DEPENDENT IMPEDANCE OF CONDUCTORS IN WIDE-BAND GAP APPLICATIONS FOR POWER ELECTRONICS

by

MARSHAL C. OLIMMAH

ANDREW LEMMON, COMMITTEE CHAIR
TODD FREEBORN
ALEXEY VOLKOV

A THESIS

Submitted in partial fulfillment of the requirements
for the degree of Master of Science in the Department of
Electrical and Computer Engineering
in the Graduate School of
The University of Alabama

TUSCALOOSA, ALABAMA

2020

ABSTRACT

Recent advancement in power electronics requires the design and development of more energy-dense and efficient converter systems, with enhanced power handling capability as well as higher switching operation. The demand and implementation of wide-bandgap semiconductor to meet the above need is on the rise. However, achieving these goals comes with challenges for the power electronic application and system designers. Several problems arise due to the densification of these systems in conjunction with the use of wide-bandgap semiconductors. The high-switching speed of these semiconductors in conjunction with the presence of parasitic elements introduces consequences which can impact power electronic system behavior and lead to system anomalies.

This thesis studies the effect of these parasitic elements and identifies skin and proximity effects as the root cause of their frequency-dependence. FEA analysis using COMSOL is used to extract basic conductor impedance parameters across frequency and to show their dependence on frequency. Analysis of the electromagnetic fields inside and around the conductors is also conducted. The resulting predictions are validated through empirical measurements using an impedance analyzer. These results indicate that skin effect alone is responsible for the frequency-dependence of conductor impedance when operated in isolation. On the other hand, both the skin and proximity effects contribute to the frequency-dependence of conductor impedance for the case of closely-spaced conductors. Implementing design schemes for power modules which accounts for these phenomena will result in increased system efficiency, reduced parasitics, and

reduced thermal load. Finally, a simple mathematical model is developed that provides good prediction of impedance across frequency with only a few parameters.

LIST OF ABBREVIATIONS AND SYMBOLS

Si	Silicon
$R_{DS(on)}$	On-state Resistance
MOSFET	Metal-Oxide-Semiconductor Field Effect Transistor
WBG	Wide-Band-Gap
SiC	Silicon-Carbide
GaN	Gallium Nitride
HEMT	High-Electron-Mobility Transistor
MCPM	Multi-chip Power Module
EMI	Electromagnetic Interference
EMC	Electromagnetic Compatibility
PCB	Printed Circuit Board
IGBT	Insulate-Gate Bipolar Transistor
C_{GS}	Gate-Source Capacitance
C_{DS}	Drain-Source Capacitance
C_{GD}	Gate-Drain Capacitance
IPES	Integrated Power and Energy System
AC	Alternating Current
DC	Direct Current
Z	Complex Impedance [Ω]
R	Resistance [Ω]

L	Inductance [H]
C	Capacitance [C]
ω	Angular frequency [rad/s]
VLSI	Very Large-Scale Integration
FEA	Finite Element Analysis
PEEC	Partial Element Equivalent Circuit
ZA	Impedance Analyzer
VNA	Vector Network Analyzer
EMF	Electromotive Force
B	Magnetic Flux Density [Wb/m^2]
H	Magnetic Field Intensity [A/m]
E	Electric Field Intensity [V/m]
D	Electric Flux Density [C/m^2]
J	Current Density [A/m^2]
Q	Electric Charge [Coulombs]
δ	Skin depth [m]
AWG	American Wire Gauge
IED	Infinite Element Domain
ω_c	Cross-over Frequency

ACKNOWLEDGEMENTS

I am truly grateful to my research advisor, committee chair, teacher and mentor, Dr. Andrew Nathan Lemmon. In my years working with him, he has instilled much knowledge, discipline and accountability in me. He has become one of my revered people on earth, of which there are a few. The lab working environment is beautiful and in great shape, thanks to his nurturing of a positive environment and enhanced productivity.

I will also like to thank members of my defense committee for their help and guidance. Specifically, Dr. Alexei Volkov, for steering me in the right path in the development of Bessel functions. Thank you, Dr. Todd Freeborn for your continued collaboration with members of our lab, we have all in one way or another, benefitted from your presence and counsel.

To my coworkers, thank you all for just being the best versions of yourselves. Chris, our tested, trusted, and reliable lab manager, thank you for all you do for us. No one does it better than you. Blake, thank you for the early groundwork which resulted in this thesis. Brian, thank you for your assistance, you always come through whenever your help is needed. Ali, thank you for being a good friend and for always putting up a smiling face. To Sergio, thank you making me love coffee once again, Colombian coffee is truly the best. Jared, thank for our unbelievable talks and exchange of viewpoints in the office. Jamie, thank you for always seeing the positive side of everything. Jin, thank you for helping me make sense of common-mode modeling. Dylan, thank you for being a part of us and for your sense of humor. Finally, thank you to my parents, Chiemelia & my siblings (Bobby, Jeffery, and Sheila). Your love, prayers and support keep me going as I one day hope to attain a PhD. I appreciate you all.

CONTENTS

LIST OF TABLES

LIST OF FIGURES

CHAPTER 1:

INTRODUCTION

The main goal of any power electronics system is to control the flow of electrical energy from an electrical source to an electrical load with the expectation of high efficiency, high power density, low cost, and minimal complexity. Power electronics is the technology associated with the efficient conversion, control, and conditioning of electrical power from its available input form into the desired output form [1]. Power electronics has penetrated almost all fields where electrical energy is present; these applications include renewable energy, automotive, aerospace, military defense, and utility systems.

The key components of any power electronics system are high-power semiconductor devices including transistors and diodes. These power devices are used as electrical rectifiers or switches within power converters. The complex operation of these semiconductors together with passive elements like inductors, resistors, and capacitors are used to satisfy various converter requirements involving voltage, current, and frequency [2].

Power converters must meet stringent performance requirements such as high reliability, low electromagnetic interference (EMI), fast transient response, and high efficiency. Power converters rely heavily on the fast switching capabilities of semiconductor power devices in order to deliver reliable and efficient power processing. Efficiency values as high as 99% have been recently reported in the literature [3], [4]. These performance achievements have been made possible by recent advancements in converter topology and semiconductor technologies. The achieved performance of a power converter, to a great extent, depends on the type of

semiconductor switch used in the converter. Therefore, to meet the need for efficient power management and conversion, power electronic circuits require high-performance switching devices to redirect and control energy flow

1.1. Advantages of Wide-Band Gap Devices

As with other areas of engineering, power electronics and power systems are subject to pressure for increased performance and efficiency. In applications such as aviation, data centers, medical imaging, electric vehicles, and military defense, there is increasing demand for greater efficiency and power density of the associated power electronic systems [5].

A high-performance power switch should possess low switching loss, good thermal characteristics, high-frequency capability, high-voltage blocking capability, and low on-state resistance. Other important characteristics of a high-performance power switch include: ease of control, ease of protection under abnormal modes of operation, and high-temperature capability [6]. Silicon (Si) based power semiconductors such as the Insulated-Gate Bipolar Transistor (IGBT) are the predominant power switches used in power electronics applications today. The ubiquitous use of Si based power devices, which have dominated the field of power electronics for many years, is due to their high reliability, reasonable performance, and low cost. However, due to the increasing demand for high-efficiency, high-voltage, and high-power-density power electronics, Si power devices are inadequate to handle present and future demands. The performance limitations of these devices arise due to the inherent limitations of the underlying materials [7]. For example, the maximum junction temperature of Si devices (150℃) hinders the use of these devices in high-power-density and high-temperature applications [7]. Si IGBTs can block voltage over 5 kV, conduct current over 1000 A, and are also very reliable [7]. However, these devices suffer from excessive switching losses, mainly due to the relatively slow decline of

the collector current during the turn-off transitions [8], [9]. This “tail current” effect limits the switching frequency to values below 20 kHz for converters that employ these devices. This constraint, consequently, limits the efficiency and power density of systems that are designed around these devices [7].

Applications that require semiconductor devices to operate at elevated junction temperatures, elevated switching frequencies, and elevated voltage levels are rapidly increasing. As such, Silicon-based devices are not able to meet these stringent requirements without costly auxiliary equipment or the use of complex topologies [10].

On the other hand, semiconductor devices based on Wide-bandgap (WBG) materials such as Silicon Carbide (SiC) and Gallium Nitride (GaN) are believed by many to be the future of power electronic applications. WGB Semiconductors created from these materials offer lower power loss, operate at higher switching frequency, and are more energy efficient compared to their Silicon counterparts [11]. WBG-based power converters are particularly advantageous in applications such as electric ground vehicles, electric aircraft, and electric ships, where power delivery and increased efficiency are necessary but space availability and weight budgets are limited [12].

Today, there is an increasing number of commercially available WBG semiconductor devices on the market. SiC Schottky power diodes were the first WBG devices to be commercially released in 2001 [13]. These devices have achieved widespread acceptance due to their superior price/performance ratio compared to Si PIN diodes [5]. The first SiC MOSFETs were commercially released by CREE in 2011 [14]. Commercial adoption of these devices has accelerated rapidly over the past several years, particularly in automotive [15] and renewable energy applications [16]. GaN high-electron-mobility transistors (HEMTs) are another type of

WBG device that are also commercially available. These devices are primarily used for radio frequency (RF) amplifier applications at high frequencies [5]. GaN HEMT devices are also gaining momentum in low-power (< 500 W), low voltage (< 600 V) power electronic applications [17]. These devices offer lower power loss and higher power density than both Si and SiC devices [11]. SiC MOSFET devices, however, provide better performance for medium voltage (600 V - 22.5 kV) and high power (> 1 MW) applications [17]. For high-temperature operation, both SiC and GaN devices can theoretically withstand elevated temperatures up to ~600℃ [18]. This makes WBG-based semiconductors a more appealing choice than Si devices for high-temperature applications.

As shown in Table 1, the band gap energy of SiC and GaN is approximately three times higher than that of Si. This difference results in significant changes in other material properties, such as thermal conductivity, breakdown field strength, and electron drift velocity. These differences in material properties enable the design of high-performance power switches, which exceed the capabilities of Si devices. These high-performance power switches in turn enable significant improvements in converter performance compared to designs based on Si switches. Consequently, adoption of these semiconductors into modern power electronics systems has been rapidly accelerating in recent years. A summary of some of the material properties of Si, SiC, and GaN [7], [10], [11], [19] is given in Table 1.

TABLE 1
MATERIAL PROPERTY COMPARISON BETWEEN SI, SIC AND GAN

Parameter	Si	4H-SiC	GaN	Unit
Thermal Conductivity	150	490	130	[W/m-K]
Breakdown Field	0.3	3	3.5	[MV/cm]
Junction Temperature	150	~600	~1600	[℃]
Bandgap Energy	1.1	3.3	3.4	[eV]
Electron Mobility	1450	900	2000	[cm^2/V-sec]
Electron Drift Velocity	1	2.7	2.5	[cm/s $\times 10^7$]
Thermal Expansion	2.6	4.2-4.7	5.6	[$\times 10^6$]/℃
Dielectric Constant	11.8	9.7	9	

With the use of WBG-based semiconductors, power electronics systems can operate efficiently at elevated switching frequencies. With attainable switching frequencies above 100 kHz, switching power losses in SiC-based converters can be reduced by 5-10 times compared to Si-based converters [20]. One of the most important driving factors for the adoption of SiC power semiconductors is the reduction of switching losses attained by fast switching. The high-signal edge rates exhibited by WBG devices yield reduced switching losses and improved converter efficiency as compared to Si-based solutions [12]. For example [21] reported switching loss reduction of more than a factor of ~7 for a SiC JFET compared to a traditional Si-IGBT with similar ratings.

To achieve significantly higher current and higher power handling capability, it is necessary to combine many power semiconductor devices in parallel within a packaging structure [17], [22], [23]. This packaging structure is known as a multi-chip power module

(MCPM). MCPMs are designed to manage the mechanical, electrical, and thermal considerations which arise as a consequence of these packaging arrangements [22]–[24].

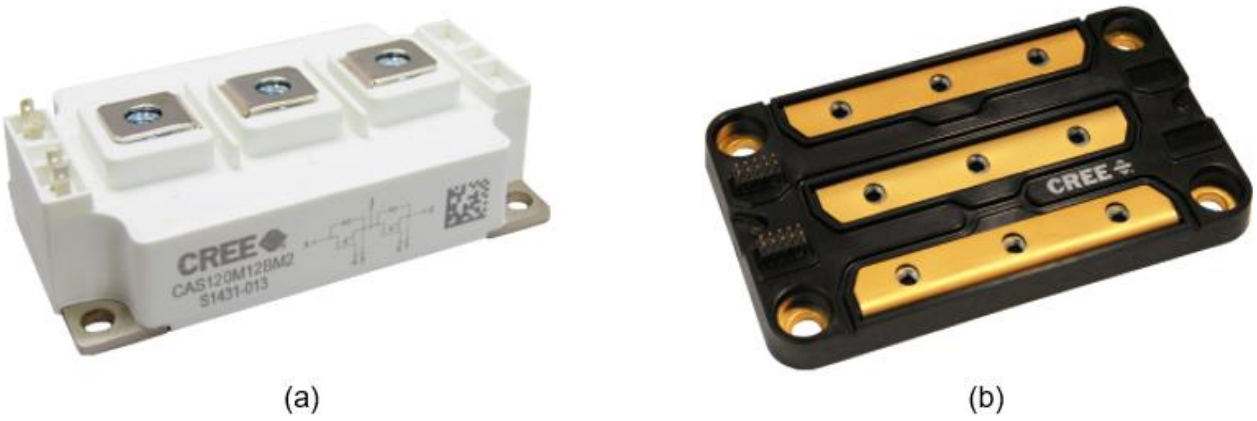

Figure 1: (a) Cree/Wolfspeed MCPM, CAS120M12BM2, and (b) Cree/Wolfspeed MCPM, CAS325M12HM2

Figure 1(a) shows a commercially available SiC MOSFET half-bridge MCPM manufactured by CREE/Wolfspeed, which is rated at 1200 V, 120 A and has an $R_{DS(on)}$ of 13 mΩ [25]. Figure 1(b) shows another SiC MOSFET half-bridge MCPM manufactured by CREE/Wolfspeed, rated at 1200 V, 325A and with an $R_{DS(on)}$ of 3.6 mΩ. This power module boasts a low commutation loop inductance value of 5 nH, ease of paralleling, and high temperature operation up to 175℃ [26].

Finally, the adoption of SiC devices make it possible to significantly increase the power density of systems employing this technology. Power density is widely recognized as one of the limiting factors for modern power electronic systems. The enhanced power density of SiC-based systems make it possible to shrink the size of some applications by an order of magnitude [18].

1.2. Challenges of Wide-Bandgap Technology

As mentioned in the previous section, one of the most important driving factors for the adoption of SiC power semiconductors is the reduction of switching losses attained by fast switching. Due to fast switching, higher signal edge rates are exhibited by WBG devices, which leads to reduced switching losses and increased efficiency. However, operating at elevated switching frequencies also creates a paradigm shift in the adoption of WGB semiconductor devices in power electronics applications. The fast switching characteristics of WBG semiconductor devices which makes them desirable, also creates challenges in their adoption in power electronics systems. WBG semiconductors devices cause applications to operate in the "Near-RF" domain as shown in Figure 2. By operating in this domain, the devices begin to behave more like RF devices rather than power devices. Lumped element analysis which were previously valid with the use of Si-based power devices, become increasingly invalid as the frequency of operation increases, as shown in Figure 2. Operation in this "Near-RF" domain also introduces additional high-frequency content that must be carefully managed to preserve proper application operation.

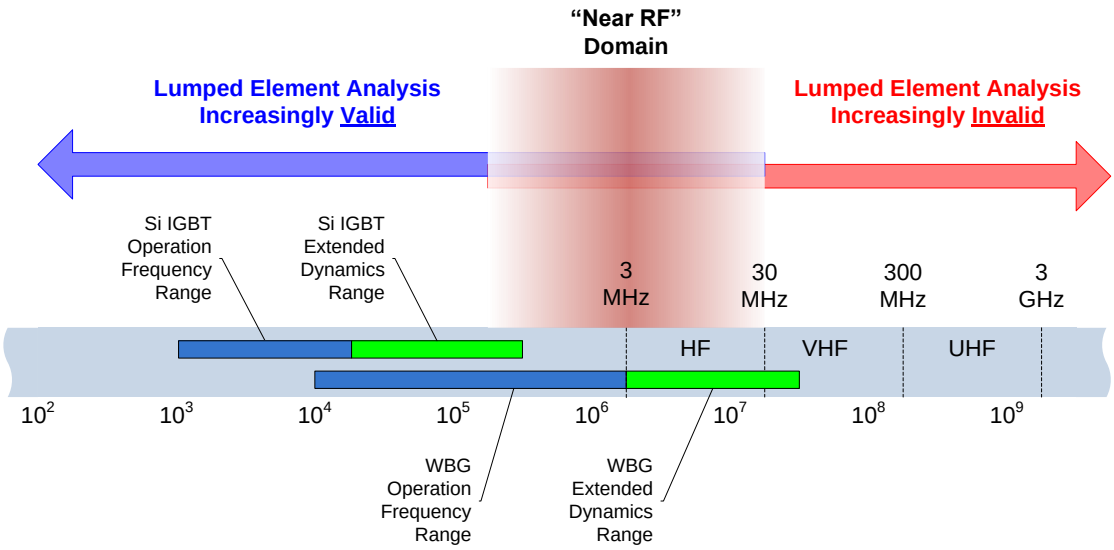

Figure 2: Operating frequency range of wide-bandgap devices [12]

One direct implication of fast switching is the excitation of resonances in parasitic impedances. These resonances are the root cause of increased EMI in WBG applications [12]. The excited resonances may be associated with impedances in the MCPM packaging structure and gate drive, in the grounding paths through heat sinks and external loads, or within EMI filtering components themselves [12]. The influence of the parasitic elements within the MCPM is especially important with regard to switching characteristics. These parasitics contribute substantially to the ringing or oscillation that is commonly observed in WBG switching waveforms. The ringing induced by parasitic elements affects the overall performance of WBG-based power converters. This may counteract the benefits obtained from high-speed switching performance [27]. Example of these parasitics include the intrinsic parasitic capacitances of the MOSFET (C_{gs}, C_{ds}, and C_{gd}) and the parasitic inductances of the packaging and interconnections. Parasitic capacitance can produce spikes during switching; slow down voltage transients; and increase electromagnetic interference (EMI) emissions due to resonance with stray inductance [22]. During turn-on, the switching speed of advanced power modules can also be limited by the gate-drain capacitance (C_{gd}) of the semiconductor [22]. The in-module stray parasitic inductance can also play a significant role in the turn-on and turn-off characteristics of WBG power devices. The high di/dt and dv/dt which are produced by fast switching of the WBG devices can deteriorate their EMI performance [28].

In addition, the very high slew-rates achievable with today's WBG devices can cause reliability and conformance (EMI) problems in practical applications [23]. High slew-rate is the primary contributor to the increased susceptibility of WBG circuits to shoot-through in the half-bridge topology [23]. During fast-switching, even the smallest parasitic inductance in combination with high di/dt leads to serious voltage spikes and ringing, which can result in

increased switching losses or may even damage the devices. Several parasitic inductance reduction schemes have been described in the literature. These strategies include improving PCB layout and design [29]; minimizing loop length and distance between capacitor and switch [30], [31]; and magnetic flux cancellation [32].

Conductors make up a significant portion of the geometry of most power converters. These conductors are found within the MCPMs, within the buswork and cabling, and within the printed circuit boards that make up the system. Due to the dense nature of modern converters, the conductors carrying high-frequency currents are often packed close to one another. Eddy currents may be induced along these conductive structures in such a way that the resulting current is forced to small region beneath the conductor surface [33]. These effects are particularly more pronounced at high frequency. Examples of eddy current effects include high surface current density, high electrothermal heating on certain conductor locations [33], and the frequency-dependence of conductor inductance and resistance [34][35].

1.3. Research Motivation and Objectives

In order to fully exploit the advantages of wide band-gap semiconductor technology in power electronics, critical parasitics must be minimized to the extent possible and accurately modeled. One important category of parasitics that has received limited treatment in the literature is that associated with frequency-dependent impedance (inductance and resistance) of conductive structures. Therefore, the primary contribution of this thesis is a set of tools and techniques to assist in modeling the parasitics of conductive structures with specific emphasis on parasitic inductance.

Additionally, the impedance of conductive structures is known to be frequency dependent. However, conductors in power electronics systems are often modeled in a simplistic

manner that neglects this behavior and treats the conductor impedance as a lumped element with a frequency-independent value. While some frequency-dependent analytical models of conductor impedance have been published [34], [36], [37], these models are generally complex and difficult to use. Therefore, this thesis seeks to provide a simple mathematical model that captures the frequency-dependent characteristics of conductor impedance for arbitrary shapes and cross-sections. The simple parameters of this mathematical model can be used directly in circuit simulation software in place of the frequency-independent impedance elements that are commonly used.

The tools and techniques provided by this thesis will enable application designers to develop models of power electronic converters with increased accuracy. These models are expected to be useful in developing a deeper understanding of application performance, and in predicting subtle frequency-dependent behaviors that are not possible to predict in simulation without such tools. These features are likely to be needed for the design and optimization of high-performance WBG applications, which are characterized by significant high-frequency artifacts.

1.4. Impedance Definitions

Throughout this thesis, impedance terms will be used frequently. This section provides specific definitions, background, and equations which will be used in the subsequent treatment.

Impedance is defined as a frequency-dependent measure of the opposition to current flow in an electric circuit. Due to this frequency-dependence, impedance is observed in alternating current (AC) circuits. The term complex impedance may also be used interchangeably. Impedance is a two-dimensional quantity which consists of resistance (real component) and reactance (imaginary component). Resistance is caused by electrons in the conductor colliding

with ionic lattice of the conductor. This means that a portion of the electrical energy is converted into heat. The resistivity of the conductor material can be used to determine the resistance of a given conductor of known dimensions. The reactance or imaginary component of the impedance is an additional opposition to the movement of the electric charges which arises from the changing electric and magnetic fields in a given circuit. Reactance is the non-resistive component of impedance in an AC circuit, which arises from the effect of inductance and capacitance. Reactance causes current and voltage to be out of phase. By sign convention, the resistance is always positive, while the reactance can assume both positive and negative values. Resistance dissipates electrical power in the form of heat while the reactance stores energy in the magnetic or electric field depending on the type of reactance component (inductor or capacitor) present. Capacitors are used to temporarily store the electrical energy in the form of an electric field. This means that, with an ideal capacitor, the voltage lags the current by 90 degrees as shown in Figure 3(a). In the case of an inductor, energy is stored in the form of a magnetic field. This means that, with an ideal inductor, the current lags the voltage by 90 degrees as shown in Figure 3(b).

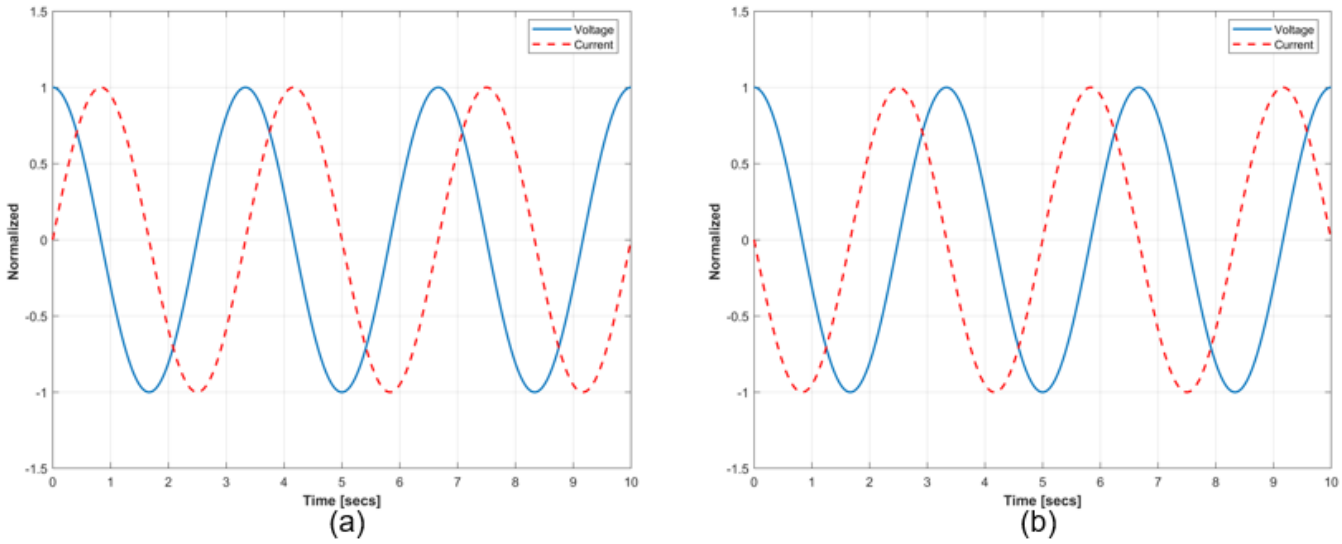

Figure 3: (a) Capacitor case: voltage lagging current and (b) Inductor case: current lagging voltage

The calculation of impedance and resistance values are the same and based on Ohms law. Like electrical resistance, impedance is also measured in Ohms (Ω). Mathematically, the phase difference is represented using complex numbers. Complex impedance (Z) can therefore be expressed in both rectangular and polar form, as given in Equation (1) and Equation (2), respectively:

$$Z = R + jX \tag{1}$$

$$Z = |Z|\angle\theta \tag{2}$$

where Z is the complex impedance, R represents the resistance of the circuit, and X represents the equivalent reactance of the circuit. For a capacitor, the complex impedance is given as:

$$Z_C = -j\frac{1}{\omega C} \tag{3}$$

and complex impedance for an inductor is given as:

$$Z_L = j\omega L \tag{4}$$

where Z_C and Z_L are the capacitive reactance and inductive reactance, respectively; C represents the capacitance in Farads (F); L represents the inductance in Henry (H); and ω represents the angular frequency of the signal in radians/second.

From the above formulas, several factors are directly implied: First, the resistance of ideal capacitors and inductors is always zero. Second, the inductive reactance for an ideal inductor is positive for all frequencies and inductance values, while the capacitive reactance of an ideal capacitor is negative for all frequencies and capacitance values. Third, the absolute value or effective impedance of an ideal inductor always increases with frequency, while the absolute value or effective impedance of an ideal capacitor always decreases with frequency. Another closely related term to impedance is admittance. Admittance is defined as the reciprocal or inverse impedance. It is a measure of how easily a circuit or device allows the flow of current. Mathematically, admittance is given by:

$$Y = \frac{1}{Z} \tag{5}$$

where Y is the admittance in Siemens (S).

1.5. Thesis Organization

This thesis is organized into the following chapters. Chapter 2 provides background and literature review for the two primary mechanisms that underly the frequency dependence of conductors, namely the skin and proximity effects. Chapter 3 introduces the general concept of inductance and provides a theoretical and mathematical background for the computation of impedance parameters for conductors of arbitrary cross-section. Chapter 4 provides a Finite Element Analysis (FEA) study for several example conductors and provides an estimation of the frequency-dependent impedance for each example. Chapter 5 provides empirical validation of the simulation predictions presented in Chapter 4 using frequency-domain measurements. Chapter 6 first provides a new modified mathematical model for representing frequency-dependent inductance in a simplified and computationally efficient manner, which is suitable for implementation in circuit simulation software. Chapter 7 concludes this thesis and provides a summary of the contributions of this work.

CHAPTER 2:

LITERATURE REVIEW

In order to study and model the impedance of conductive structures within MCPMs and converters employing WBG technology, it is necessary to provide background and review to aid in the systematic study of these conductors.

2.1. Frequency-Dependent Conductor Impedance

Accurate, frequency-dependent models of conductor impedance in WBG-based power electronic systems are particularly important. Presently, most conductor models utilize static, lumped impedance parameters with values that are frequency independent. However, this approach presents a problem at high frequency because these parameters are not fixed but vary with frequency. Static, lumped-impedance models become inadequate to accurately capture transient behavior at high-frequency. For example, in a shipboard Integrated Power and Energy System (IPES) study, A. Colavitto et.al. present the impact of high-frequency disturbances and their effects on power systems [38]. The authors argue that the variation in system parameters (i.e. inductance, resistance, capacitance and conductance) with frequency is one of the first challenges in systems affected by harmonic disturbance. Therefore, when analyzing the system behavior over a wide frequency range, the conventional lumped parameter models become inapplicable [38]. Furthermore, in the area of power transmission and distribution, the frequency-dependence of resistance and inductance cannot be neglected. This is because these sensitivities attenuate and distort the propagation of voltage and current waves [39].

Presently, there are several models aimed at representing the inductance and resistance of conductors as a function of frequency [40], [41]. Although these models are accurate, they are very difficult to implement in circuit simulators such as SPICE. Other models represent frequency-dependent conductor impedance with networks of frequency-independent lumped elements. These models include the ladder model [36], [37], [42], the volume filament model [43], [44], and compact circuit models [45], [46]. These models can be directly used in SPICE solvers. However, both the volume filament model and the ladder model incorporate large numbers of circuit elements and are expensive in terms of computational time [34]. On the other hand, the compact circuit model uses an iterative process to identify the best circuit element parameter values. Since the compact model is based on a semi-empirical formula for calculating circuit elements, it is not suitable for predicting circuit element values for conductors of arbitrary shapes [34].

Eddy currents have been identified as the primary cause of the frequency-dependent nature of the impedance of conductive structures. A detailed review of eddy currents and the associated impacts on conductors in power electronic systems is presented in the next section.

2.2. Eddy Current Background and Review

The laws of static electric and magnetic fields are useful for predicting the behavior of many systems. Dynamic effects which are not fully described by the static magnetic and electric field relationship require a more complete formulation. Two important dynamic effects include the generation of an electric field by a time-varying magnetic field, and the complementary effect whereby a time-varying electric field produces a magnetic field [40]. According to Faraday's law of induction, a time-varying magnetic field passing through an open surface will induce an electric field around a closed-loop contour that encircles the surface. This contour can

be thought of as either a conducting material or an imaginary contour of non-conducting material [47][33]. If this contour lies within a conductive structure, voltage gradients will also be induced within this structure, giving rise to distributed currents circulating in various paths [33]. These distributed currents are referred as eddy currents. Eddy currents are therefore loops of distributed electrical current which are induced within conductive structures by a changing magnetic field in proximity to the conductor [48]. Eddy currents, like currents moving through a closed loop filament, produce several different effects. First, eddy currents produce forces arising from the interaction of the inducing and the induced field; second, eddy currents produce heat due to ohmic losses incurred when charge carriers interact with the conductor lattice; and third, eddy currents produce a magnetic reaction field [33].

2.2.1. Eddy Current Review

The manifestations of eddy currents are useful in some applications. For example, D. Chen et al. demonstrate the use of pulsed eddy current (PEC) signals for the evaluation of metallic plate thickness in [49]. These authors used reflection type PEC probes comprised of an exciter coil and a sensor coil. According to the authors, the PEC method offers advantage in terms of cost savings and simplicity compared to other classical thickness evaluation methods.

In another recent paper, A. K. Singh et al. present another application of eddy currents in braking technology [50]. The eddy current braking (ECB) system presented in this paper is based on the principles of Lenz's law. The authors argue that ECB offers multiple advantages over traditional friction brakes such as fast-response time, reduced wear, reduced sensitivity to fading, faster control dynamics, reduced fuel consumption, and dynamic stability. The applications of eddy current braking include high speed railways [51], [52]; automobiles [53], [54]; rotary dampers [55][56]; energy absorption systems in aircraft [57]; and air bearing systems [58]. Other

applications in which eddy currents are useful include induction furnaces, magnetic levitation systems, biomedicine applications, and squirrel cage rotors for asynchronous machines [33].

Although eddy currents are useful in several important applications, these currents produce undesirable effects in other applications. According to M. Motalleb et al., the concentration of eddy currents can cause high local losses and overheating in the metallic parts of transformers [59]. Similar eddy current effects appear throughout the conductive structures found within power electronic applications [60], [61].

Eddy currents are associated with two important phenomena within conductive structures: the skin effect and the proximity effect. In power electronic converters employing WBG technology, the skin and proximity effects are especially pronounced for two reasons. First, these systems are operated at elevated switching frequencies and exhibit additional unintended high-frequency behavior due to the fast-switching action of WBG semiconductors. Second, the semiconductor devices and conductive structures within such systems are usually confined within a small space, which places many conductors close to one another. A brief review of the skin and proximity effects is provided in the following sections.

2.2.2. Skin Effect Background and Review

The skin effect describes the tendency of an alternating current to become distributed within a conductor such that the current density is highest near the surface of the conductor and decreases progressively toward the center of the conductor [48][35]. With direct current (DC), the current in a conductor is evenly distributed over the cross-section. However, when alternating current (AC) flows through a conductor, a time-varying magnetic field is induced, which in turn induces an electric field within the conductor. Due to this time-varying field, the current in the conductor becomes unevenly distributed over the cross-section [34]. As a result, the current

density near the surface of the conductor is greater than the current density at the center of the conductor. For very high frequency applications, this crowding is so extreme that nearly all the current flows in a thin layer close to the surface of the conducting material. This gives rise to an important parameter called skin depth. Skin depth is defined as the depth within the conductor at which the current density falls to e^{-1} of its value at the surface [48]. The mathematical definition of skin depth is given by:

$$\delta = \frac{1}{\sqrt{\pi f \mu \sigma}} \tag{6}$$

where δ represents the skin-depth in meters (m), f represents the frequency in hertz (Hz), μ represents the permeability in Henry/meter (H/m), and σ represents the conductivity in Siemens/meter (S/m).

For systems involving high-frequency signals, the impact of skin effect cannot be overlooked. For example, S. Mei et al. argue that neglecting or ignoring skin effect underestimates the propagation delay of very large scale integrated (VLSI) circuits by almost 20% [34]. The skin effect is also an important consideration for power electronic systems based on WBG power semiconductors [62].

2.2.3. Proximity Effect Background and Review

The proximity effect is another phenomenon that is closely related to the skin effect. The proximity effect describes the presence of eddy currents that are induced by magnetic fields associated with neighboring current-carrying conductors. The proximity effect may occur whenever two or more conductors carrying high-frequency currents are closely spaced. In a recent paper, T. Asada et al. describe the sensitivity of proximity effect to the separation distance between conductors [63]. These authors argue that, with increasing separation distance between conductors, the influence of proximity effect is dramatically reduced. With a separation distance

of 0.2mm, the proximity current reaches nearly 70% of the applied current. With separation distances of 1mm and 2mm, the proximity current reduces to about 40% and 20% of the applied current respectively. In another recent paper, Y. Alkraimeen et al. argue that the proximity effect is the predominant factor that determines the damping of high-frequency transient behavior in transformers [64]. Above the kHz range, the proximity effect cannot be ignored [39], especially in WBG-based converter systems within which many conductors carrying high-frequency signals are tightly packaged.

2.2.4. Conductor Impedance Models

The skin and proximity effects dramatically change the effective resistance and inductance of conductors at high frequency [34], [35], [48]. Models that represent the change in conductor resistance at high frequency due to the skin and proximity effects are available in the literature. For example, A. Pagnetti et al. and W. Kuhn et al. model these effects through a simple expression that scales the DC resistance in proportion to the root of frequency [39], [65]. On the other hand, models that represent the change in inductance at high frequency due to the skin and proximity effects are not available in the literature. In general, the frequency dependence of inductance has received limited treatment in the literature, especially for conductors of arbitrary shapes and sizes.

Presently, there are well established analytical skin effect models, especially for an isolated cylindrical conductor of circular cross-section [40]. This is due to the fact that the current distribution is symmetric about the wire axis, which makes the required analysis straightforward [66]. However, there are no available analytical models that describe the proximity effect. In the case of proximity effect, the current distribution is not symmetric about the wire axis, which makes the required analysis difficult. Therefore, one of the principal goals

of this thesis is the development of a simple mathematical model that captures the influence of both the skin and proximity effects with reasonable accuracy. This mathematical model is presented and implemented in the form of an equivalent circuit model in Chapter 6.

In order to model and explain the frequency-dependence of conductor impedance, some method of impedance estimation for physical conductor geometries is needed. A variety of techniques that can be utilized for this purpose are outlined in the next section.

2.3. Impedance Estimation Techniques

There are two primary methods used by practitioners for estimating the impedance of electrical conductors: the analytical method and the empirical method. The analytical method involves the utilization of physics-based relationships and sophisticated software to predict the conductor impedance from physical geometry. Examples of the analytical method include the partial element equivalent circuit (PEEC) method and the finite element analysis (FEA) method. The empirical method involves the use of instrumentation to measure the impedance of the device under test (DUT). In general, simulation results from the analytical methods cannot be trusted without some form of validation. Therefore, empirical measurements are often used to validate impedance estimates provided by analytical means. This leads to increased confidence of the resulting impedance model. Examples of instruments that may be used to implement the empirical method include: LCR meters, impedance analyzers (ZAs), vector network analyzers (VNAs), time-domain reflectometry (TDR) instruments, and radio-frequency current-voltage (RF-IV) instruments [17][67]. The tree diagram of Figure 4 provides a summary of the common impedance estimation techniques.

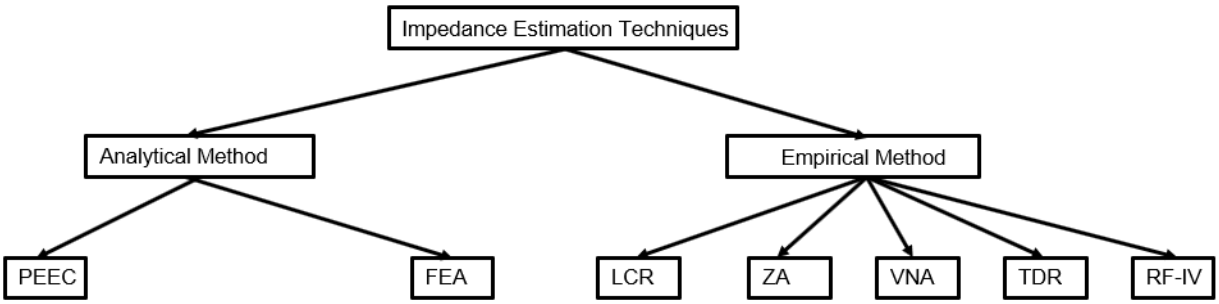

Figure 4: Impedance estimation techniques [67]

2.3.1. Analytical Method Review and Background

Partial element equivalent circuit (PEEC) and finite element analysis (FEA) are the most widely used analytical methods for impedance estimation. In the PEEC method [68]–[74], inductance and capacitance values are calculated using Maxwell's integral equations instead of differential equations, based on geometry and material information [70]. The PEEC method does not use Maxwell's equations directly to solve electromagnetics problems; instead, this method represents the electric and magnetic field interactions as capacitance and inductance elements, respectively.

Using the PEEC method, many small segments of the geometry under consideration are transferred from the electromagnetic domain to the circuit domain. This allows conventional circuit solvers to solve and analyze the resulting equivalent circuit. For modeling conductors, self-partial inductance and resistance values are attributed to each segment or portion of the conductor. The values of self-partial inductance and resistance assigned are uniquely determined by the geometry of the particular part of the conductor in question [74]. The influence of neighboring conductors is also taken into account by means of mutual-partial inductances between the conductors [74]. Because the outcome of this method is represented in the circuit domain, the resulting model can be readily simplified by omitting parameters of negligible value. This model simplification process reduces simulation cost, especially for complex system simulations. Model simplification is also useful when a large number of design iterations are involved [70]. PEEC models can be employed in both the frequency domain and the time domain [68]. The PEEC method has been successfully applied to estimate the impedance of conductive structures within power electronics systems. For example, W. Teulings et al. utilized the PEEC method to estimate the stray inductance of PCB tracks and component leads in [74].

The other popular analytical method is FEA. The FEA method is the most widely used analytical method for estimating impedances and solving electromagnetic problems. This method can also be applied for understanding and quantifying other physical phenomena such as wave propagation, fluid dynamics, and thermal transfer. Within the field of power electronics, the FEA method has been applied successfully in the impedance estimation of interconnects, transformer windings, and induction machines [60], [75]–[82]. Using the finite element method, the object or system under study is decomposed into a geometric model which consists of thousands or millions of simple, small parts. These decomposed or subdivided parts are referred to as finite elements. Physical relationships, such as Maxwell's equations, are then applied individually to each of the finite elements to determine the behavior of the overall system.

The FEA method is frequently used within the field of power electronics to understand physical phenomena and to estimate the impedance of conductive structures. For example, M. Mermet-Guyennet et al. employed FEA to analyze the current density distribution in fast-switching SiC components in [82]. These authors successfully employed FEA to evaluate the influence of skin effect and to estimate the parasitic impedance of the device under study. In a related study, B. Mouawad et al. employed commercial FEA software to estimate the parasitic impedance of the interconnect structures within a 2.5 kV SiC-based MCPM [83]. Because the FEA method solves the basic physics equations at a granular level, it can predict detailed physical interactions and electromagnetic field behavior which may be lost using the PEEC method. However, FEA is generally more computationally intensive than PEEC for a given problem. Nevertheless, given the usefulness of FEA for analysis of complex structures and the affordability of computing power, the use of FEA is more widespread than the use of PEEC.

2.3.2. Empirical Method Review and Background

Unvalidated results from analytical impedance estimation methods should not be trusted due to the large number of parameters involved in the simulation environment as well as the possibility of unknown sensitivities [79]. It is thus necessary to empirically validate simulation results obtained from the analytical methods described in the previous section. In other cases, impedance measurements can be directly used to inform the develop of equivalent circuit models for conductive structures. Common techniques for estimating impedance parameters through empirical measurements are described in the following sections.

2.3.2.1. Inductance-Capacitance-Resistance (LCR) Meters

LCR meters are used to measure the impedance of devices and components in a simple fashion [80], [84]–[87]. With these instruments, the DUT is subjected to an AC voltage stimulus. The applied voltage stimulus and the resulting current through the DUT are measured. The impedance magnitude and phase can be calculated from these measured quantities and translated to lumped L, C, and R values. The stimulus signal of the LCR meter generally operates at a fixed frequency. While the frequency of the stimulus may be configurable, the instrument usually does not have a provision for automatically sweeping the stimulus signal frequency. As a result, LCR meters typically provide individual parameter values as shown in Figure 5. This makes LCR meters unsuitable for frequency-dependent impedance measurements, as it is cumbersome to perform repeated measurements while manually varying the stimulus signal frequency. Nevertheless, LCR meters are useful performing quick estimates of individual component values and can often provide accurate results. For example, K. Bertling et al. utilized an LCR meter to estimate equivalent circuit model parameters for a Silicon-on-Sapphire (SOS) MOSFET in [84]. In this paper, the authors demonstrate that the measurements obtained from the LCR meter are in

good agreement with measurements obtained from a vector network analyzer (VNA) for the same device.

Figure 5: Keysight E4980A precision LCR meter [85]

2.3.2.2. Impedance Analyzers (ZAs)

The Impedance Analyzer (ZA) is another instrument that is used to measure the impedance of various components and structures [70], [79], [88]–[92]. The ZA offers several features that provide additional flexibility compared to the LCR meter for general purpose impedance measurements. For example, the stimulus signal frequency of the ZA can be automatically swept across a user-specified range, which provides a convenient means for evaluating the frequency dependence of DUT parameters. In addition, the accuracy of ZA measurements is generally at least an order of magnitude better than the accuracy of LCR meter measurements [85], [92]–[95]. Finally, most ZAs can apply a voltage or current bias to the DUT during measurement. Figure 6 shows an example impedance analyzer instrument, which is manufactured by Keysight Technologies [92].

Figure 6: Keysight E4990A impedance analyzer [92]

ZAs have been successfully employed in the measurement of many types of structures within the field of power electronics. For example, A. Lemmon et. al, utilized a ZA to perform frequency-domain analysis of the parasitic interconnect impedances within a SiC MOSFET half-bridge MCPM in [79]. X. Gong et al. also employed a ZA to estimate the parasitic impedance parameters for a motor drive inverter in [91]. In this paper, the measured impedance parameters were used directly to develop an equivalent circuit model for the system under consideration. Of all the measurement instruments, the ZA is the simplest to use, since impedance parameters can be obtained directly from the measured data [17].

2.3.2.3. Vector Network Analyzers (VNAs)

The vector network analyzer is another frequency domain measurement instrument [96]–[104]. The VNA is widely used for RF design applications at frequencies up to the GHz range [97], [103]. The VNA instrument computes scattering parameters (S-parameters), which can be converted to impedance parameters using standard expressions [103]. In computing the S-

parameters, the instrument treats port variables as traveling waves, rather than voltage or current, thereby overcoming certain difficulties usually encountered in the estimation of model parameters at RF frequencies [100]. Figure 7 shows an example VNA, which is manufactured by Keysight Technologies [105].

Figure 7: Keysight E5080B vector network analyzer [105]

Because the S-parameters measured by this instrument must be converted to Z-parameters for impedance estimation, some additional complexity is introduced. Although VNAs are capable of measuring at higher frequencies than is possible with ZAs, the impedance measurement range of VNAs is generally limited [67]. Although the VNA measurement technique involves additional complexity, it has nevertheless been used to estimate the impedance of complex structures within the field of power electronics. For example, A. Lemmon et al. successfully employed a VNA to estimate the impedance of the interconnect structures within a 10-kV SiC MOSFET half-bridge power module in [91]. In a similar study, E. McShane et. al successfully used a VNA to estimate the parasitic impedances within a Silicon MOSFET in a TO-247 package [103].

2.3.2.4. Time Domain Reflectometry (TDR) Instruments

One additional empirical impedance estimation method is time domain reflectometry (TDR) [77], [106]–[109]. The TDR instrument measures reflections which occur when the stimulus signal interacts with boundaries between transmission media such as circuit boards, cables, and connectors, etc. The TDR technique involves injecting a pulse with fast rising and falling edges into the DUT. The TDR instrument then compares the measured reflections from the unknown transmission environment to those associated with known, standard impedance interfaces. Figure 8 shows a simplified block diagram of the TDR instrumentation setup.

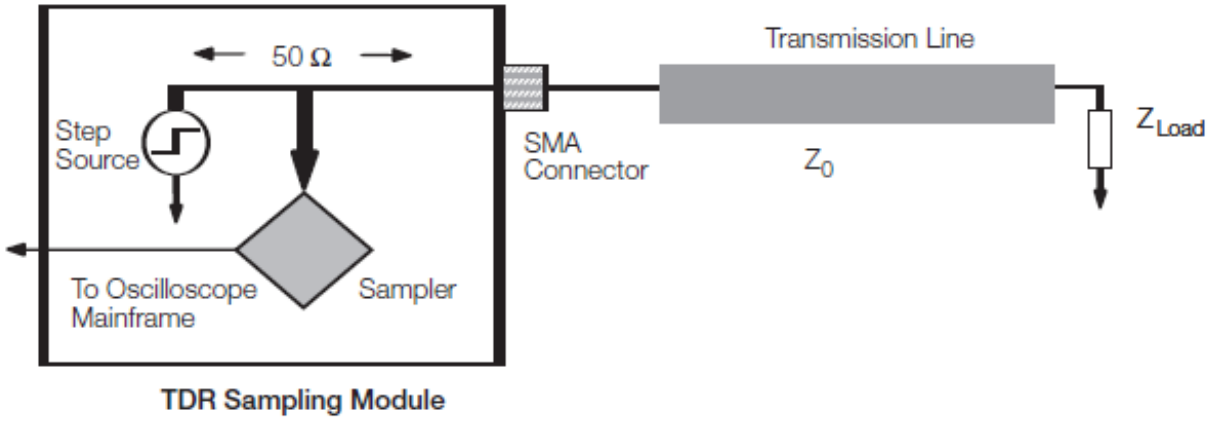

Figure 8: Block diagram of TDR Circuit [109]

One major drawback of commercial TDR instruments is that they are normally designed for DUTs with a characteristic impedance of $50\ \Omega$. This is because the primary application for TDR instruments is the identification and localization of faults within high-frequency coaxial cables [110]. The accuracy of impedance estimates obtained via the TDR technique can be degraded when there is a significant difference between the measured impedance of the DUT and the expected characteristic impedance value ($50\ \Omega$) [106]. In addition, the TDR technique requires special software as well as special hardware (TDR/sampling head) to perform impedance

estimation [111]. The TDR technique can also not be used to evaluate the frequency-dependence of the DUT impedance, since the analysis is performed in the time domain. Nevertheless, the TDR technique has been employed to estimate the impedance of complex structures in power electronics applications. For example, H. Zhu et al. utilized the TDR technique to estimate the impedance of the interconnect structures within a Si IGBT power module in [108].

CHAPTER 3:

IMPEDANCE AND ELECTROMAGNETICS OF CIRCUITS

WBG semiconductor devices enable short switching times and operation at increased frequencies compared to Si devices. As a result of this fast switching action, the optimum performance of WBG-based converters is crucially confined by the influence of system parasitics. Therefore, the impact of the parasitic effects (resistive and inductive) within the power loop of conductive structures within WBG-based converter systems cannot be overlooked. At high frequency, the current distribution in the conductors become inhomogeneous. This inhomogeneous distribution of current at high frequency is responsible for the frequency-dependent nature of resistance and inductance and other undesirable effects already described in Chapter 2.

With regard to resistance, skin effect increases the resistance of a conductor in proportion to the root of frequency as compared to the DC resistance. This frequency-dependent model for conductor resistance is well established in the literature [39][66]. However, in the case of inductance, the frequency-dependence varies with the geometry of the conductive structure present. For example, the frequency-dependent inductance of a circular loop conductor is expected to behave differently from that of a rectangular loop. In the case of the rectangular loop, the proximity of the return path plays a significant role in the frequency-dependent nature of the conductor inductance.

It is thus necessary to provide a detailed treatment of inductance as well as some background material on electromagnetics in support of the major tenets of this thesis. This

information will aid in understanding the magnetic and electric field interactions around the conductors under consideration. Accordingly, the next section includes a detailed discussion of inductance and provides the necessary background information on electromagnetics.

3.1. Inductance

Inductance is the tendency of an electrical conductor to oppose the change of electric current flowing through it. Whenever electric current flows through a conductor, it induces a magnetic field around the conductor. The magnetic field strength depends on the magnitude of the electric current. Therefore, whenever there is a change in the magnitude of the electric current through a conductor, the magnetic field around that conductor also changes. According to Faraday's law of electromagnetic induction, a changing magnetic field in proximity to a coil of wire will cause an electromotive force (EMF) to be induced in the coil. Due to this EMF, the coil inductance opposes an increase or decrease in the electric current flowing through it.

There are several methods for calculating the loop inductance of a conductor carrying current. These methods include the vector magnetic potential, Ampere's law, Neumann integral, and the energy storage method. The aforementioned methods require computation of the flux through the open surface that is enclosed by the loop [47]. Consider the conductor loop shown in Figure 9. A current is injected into the loop by cutting a small gap in the conductor and injecting the current such that it flows in an anti-clockwise direction as shown in Figure 9. The current in the loop will produce a magnetic flux in the cross-hatched region marked S which is bounded by the conducting loop.

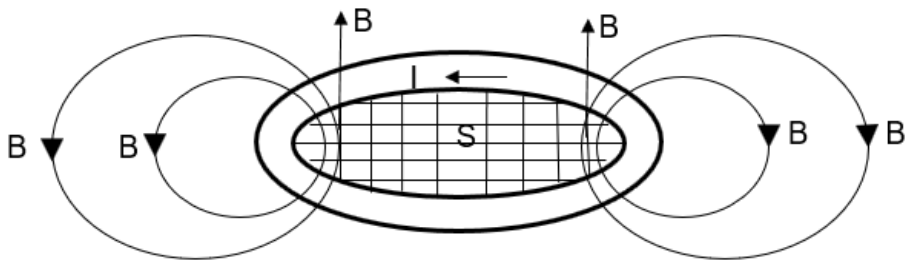

Figure 9: Conductor loop carrying current

Inductance has several definitions depending on the type of formulation used. From an energy point of view, inductance is described as the magnetic energy storage capability of the conductor. Therefore, the magnetic energy stored in a given region of volume due to a system of current loops is given by:

$$W_M = \frac{1}{2}\int_v B \cdot H \, dv = \frac{1}{2} LI^2 \tag{7}$$

where W_m represents the magnetic energy in Joules (*J)*, B represents the magnetic flux density in Webers per square meter (Wb/m^2), or Telsa (*T*), H represents the magnetic field intensity in amperes per meter (A/m), I represents the current passing through the conductor in amperes (*A*), and L represents the inductance in Henries (*H*). From Equation (7), the inductance can be re-written as given in Equation (8):

$$L = \frac{2W_M}{I^2} = \frac{\int_v B \cdot H \, dv}{I^2} \tag{8}$$

The inductance of a conductor can also be defined in terms of the magnetic flux penetrating the surface of the conductor loop. Mathematically, the magnetic flux penetrating the current loop is given by:

$$\Phi = \int_s B \cdot ds \tag{9}$$

where Φ represents the magnetic flux in Webers (Wb), and B represents the magnetic flux density in webers per square meter (Wb/m^2), or Telsa (T). Using this formulation, the inductance can be expressed in terms of the magnetic flux penetrating the current loop:

$$\mathrm{L} = \frac{\Phi}{I} = \frac{\int_s B \cdot ds}{I} \tag{10}$$

where L represents the inductance in Henries (H), Φ represents the magnetic flux in Webers (Wb), I represents the current passing through the conductor in amperes (A), and B represents the magnetic flux density in webers per square meter (Wb/m^2). If the surrounding medium is linear, homogenous and isotropic, the total magnetic flux threading the current loop is directly proportional to the current which produced it. Therefore, the inductance of the loop is a function of the loop shape, the loop dimensions, and the material properties of surrounding medium.

The induced electromagnetic fields from a conductor affect the movement of electrons in the conductor as well as the movement of electrons in any nearby conductors. Therefore, inductance can be separated into mutual-inductance and self-inductance. Mutual inductance arises from the induced voltage in one circuit due to the current flowing in another nearby circuit [47], [112], [113]. The self-inductance of a conductor arises from the effects of electromagnetic fields generated by the conductor itself [40], [47], [113]. Self-inductance can further be separated into two components, namely internal self-inductance and external self-inductance [40], [47], [66], [114]. Internal self-inductance considers the total magnetic energy stored inside the conductor boundaries [39], [40], [47], [114]. Whenever a conductor carries current, a magnetic field is generated both inside the conductor as well as outside the conductor. Therefore, some of the magnetic energy is stored within the conductor. The stored magnetic field inside the

conductor gives rise to its internal self-inductance, which is often called simply the internal inductance. The external self-inductance, which is often called simply the external inductance, considers the magnetic energy stored outside the conductor boundaries [40], [47]. The total self-inductance of a conductor loop includes the contribution of both the internal inductance and the external inductance. This relationship is represented by Equation (11).

$$L_{loop} = L_{internal} + L_{external} \tag{11}$$

The tree diagram of Figure 10 provides a summary of the various components of inductance described in this chapter.

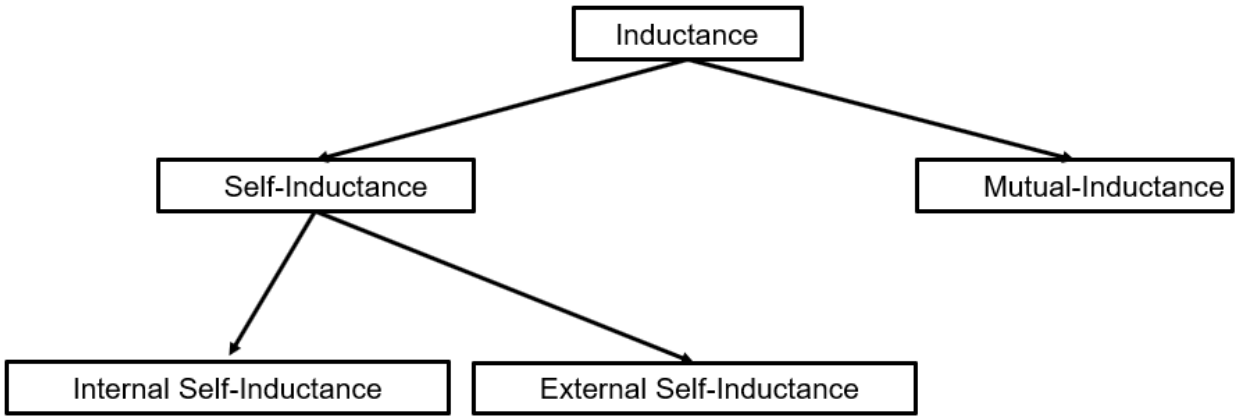

Figure 10: Classification of Inductance

3.2. Electromagnetics Fundamentals

To understand and explain the frequency-dependence of the impedance of conductive structures in WBG-based converters, a thorough understanding of electromagnetics is required. Accordingly, the relationships that provide the foundation of electromagnetics are given in detail in this section.

The design and analysis of electrical systems typically depend on modeling circuit interactions through lumped-elements equivalent circuits. In these lumped-type circuit models,

the energy storage elements (inductors and capacitors) as well as the dissipative elements (resistors), are connected to each other and to active elements by conducting paths of negligible impedance. In addition, one critical assumption is made in the formulation of such models. Specifically, the geometric dimensions of the circuit in question are assumed to be much smaller than the wavelengths of the signals contained therein. This is referred to as the so-called “long wavelength” approximation. Under this assumption, the fields around the elements are quasistatic. In other words, the spatial distribution of these fields is approximately the same as that of static fields, even though the actual fields may vary rapidly with time [40]. Due to the quasistatic nature of these fields, they may be approximated from static field equations. However, there are other important dynamic effects which are not described by static field relationships. These dynamic effects, which are usually associated with time varying problems or cases in which the long wavelength approximation does not hold, require a complete formulation. This is the case for the skin and proximity effect phenomena described in Chapter 2.

As a rule, a resultant wave phenomenon occurs whenever there are at least two forms of energy present in a medium. The presence of one form of energy which is time-varying in nature, leads to a time rate of change in the other energy form. For example, in a sound wave, the initial pressure variation in air (potential energy) at a location gives rise to a motion of air molecules (kinetic energy) which varies both in time and space [40]. The motion of the air molecules subsequently causes pressure variation at new locations in the air mass, which create new loci of potential energy, and so on. Another example is the presence of the electric and magnetic fields in circuits. Electric and magnetic fields interact in a similar, mutually reinforcing manner as they propagate away from an emissions source and into the far-field. The interaction between these fields at high frequency also gives rise to the phenomena known as the skin and proximity effects

within conductive structures. Fundamentally, electromagnetic (EM) fields must satisfy the four basic relationships known as Maxwell's equations, which are described in the following section.

3.2.1. Maxwell's Equations for Electric and Magnetic Fields

Maxwell's equations include four foundational relationships for electromagnetics: Gauss' law for electric fields, Gauss' law of magnetism, Faraday's law of induction, and Ampere's law. These equations are used to describe and represent electric and magnetic fields; how they affect each other; how these fields are affected by charges and currents; and how charges and currents are also affected by the fields.

There are four basic physical terms used to describe electromagnetic fields. These physical terms are electric field intensity E in (V/m) , magnetic flux density B in (Wb/m^2), electric displacement or electric flux density D in (C/m^2), and magnetic field intensity H in (A/m). A complete list of Maxwell's equation is provided in Table 2.

TABLE 2
MAXWELL'S BASIC EQUATIONS

$$\nabla \cdot E = \frac{\rho}{\varepsilon_0} \tag{12}$$

$$\nabla \cdot B = 0 \tag{13}$$

$$\nabla \times E = -\frac{\partial B}{\partial t} \tag{14}$$

$$\nabla \times B = \mu_0 J + \frac{1}{c^2}\frac{\partial E}{\partial t} \tag{15}$$

Equation (12) is derived from Gauss's law for electric fields, which describes the strength of the electric field around a point charge. Equation (13) is derived from Gauss's law of magnetism, which describes the strength of the magnetic field around any material present within

a defined boundary. Equation (14) is derived from Faraday's law of induction, which describes how a time-varying magnetic field induces an electric field and vice-versa. Finally, Equation (15) is derived from Ampere's law, which describes how a time-varying electric field generates a magnetic field, while accounting for displacement current.

Because most engineering problems use sinusoidal fields, a more convenient formulation of these expressions may be found by leveraging the concept of the complex exponential ($e^{j\omega t}$). Representing sinusoids with the complex exponential form is advantageous because the derivatives and integrals of the complex exponential are in fact proportional to $e^{j\omega t}$. These terms may be canceled from the resulting expressions. Accordingly, Maxwell's equations of Equation (14) and Equation (15) can be changed to complex exponential form or phasor-domain form by replacing the differential term $\partial/\partial t$ with $j\omega$. Therefore, in regions of space where no charges or currents exist, the final form of Maxwell's equations is given in Table 3 [115].

TABLE 3
MAXWELL'S BASIC EQUATIONS WITHOUT CHARGE

$$\nabla \cdot E = 0 \tag{16}$$

$$\nabla \cdot B = 0 \tag{17}$$

$$\nabla \times E = -j\omega B \tag{18}$$

$$\nabla \times \mathrm{H} = J + j\omega D \tag{19}$$

For a complete derivation of Maxwell's equations, please refer to Appendix A.2 of this thesis.

3.2.2. Field Penetration (Skin-Depth) into Conductor

The existence of fields around a current-carrying conductor implies there are also field penetrations into the conductor. This field penetration is useful for predicting the frequency-dependence of conductor impedance. Equation (18) can be used in the derivation of the field penetration into a conductor. For the cylindrical conductor cross-section shown in Figure 11, the skin-depth (δ) is defined as the depth within the conductor at which the current density falls to e^{-1} of its value at the surface [48].

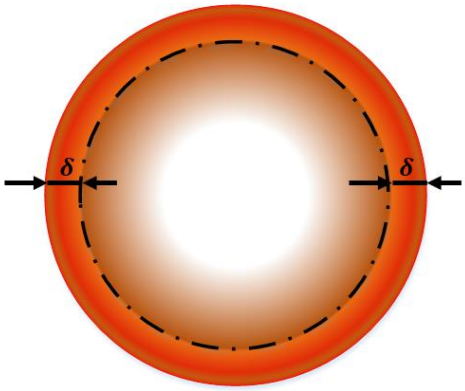

Figure 11: Current distribution in a cylindrical conductor

The field penetration or skin-depth into a conductor is given mathematically in Equation (20) as:

$$\delta = \frac{1}{\sqrt{\pi f \mu \sigma}} \tag{20}$$

where δ represents the skin depth in meters (m), f represents the frequency in Hertz (Hz), μ represents the permeability of the medium in H/m, and σ represents the conductivity of the conductor in siemens per meter S/m. For a complete derivation of Equation (20), please refer to Appendix A.3 of this thesis. A system of equations describing the electric field E, the magnetic field H and the magnitude of the current density J, for a conductor of arbitrary shape is given in [40] as:

$$E_z = E_0 e^{-x/\delta} e^{-jx/\delta} \quad (21)$$

$$H_y = H_0 e^{-x/\delta} e^{-jx/\delta} \quad (22)$$

$$J_z = J_0 e^{-x/\delta} e^{-jx/\delta} \quad (23)$$

where $E_0, H_0, and\ J_0$ are the magnitudes of the electric field, magnetic field and current density at the conductor surface. Equation (21), Equation (22), and Equation (23), demonstrate that the magnitudes of the fields and the current density decrease exponentially with penetration into the conductor.

3.3. Impedance of Conductors

In order to systematically study the skin and proximity effects, two primary example conductor shapes will be used in this thesis. The test cases include a circular loop conductor and a rectangular loop conductor with a very close return path. The circular loop conductor will be used to demonstrate skin effect; while the rectangular loop conductor will be used to demonstrate the combined influence of the proximity effect and the skin effect. Knowledge gained from both test cases can be extended to conductors of arbitrary shape and cross-section. To properly contextualize these test cases, a brief study of field penetration into an infinite plane conductor is necessary. This study serves as a basis of the analytical formulation that will be employed in the following test cases. Also, the skin-effect model for plane conductors is well developed in the literature [40], [66].

3.3.1. Internal Impedance of Plane Conductors

For any conductive structure, the internal impedance is defined as the ratio of the surface electric field to the current which concentrates at the surface of the conductor. Internal impedance is given mathematically as [40]:

$$Z_s = \frac{E_{z0}}{J_{sz}} = \frac{(1+j)}{\sigma\delta} \tag{24}$$

where Z_s represents internal impedance for a unit length and width in (Ω), E_{z0} represents the electric field intensity at the surface in (V/m), J_{sz} represents the total current density flowing past a unit width of plane surface in (A/m^2), σ represents the conductivity in (S/m), and δ represents the skin-depth in (m). The current density J_0 is related to E_{z0} by the equation:

$$E_{z0} = \frac{J_0}{\sigma} \tag{25}$$

where E_{z0} represents the electric field intensity at the surface in (V/m), J_0 represents the current density at the surface of the conductor in (A/m^2), and σ represents the conductivity of the conductor in (S/m). Recalling Equation (1) and Equation (4), the complex impedance for a resistor in series with an inductor in cartesian form is given by:

$$Z_s = R_s + j\omega L_i \tag{26}$$

Comparing Equation (24) and Equation (26), it is apparent that the resistance (R_s) and internal reactance (ωL_i) of a conductor can be individually represented as:

$$R_s = \frac{1}{\sigma\delta} = \sqrt{\frac{\pi f \mu}{\sigma}} \tag{27}$$

$$\omega L_i = \frac{1}{\sigma\delta} = R_s \tag{28}$$

where R_s represents the conductor resistance in (Ω), σ represents the conductivity in (S/m), δ represents the skin-depth in (m), f represents the frequency in (Hz), μ represents the permeability of the medium in H/m, L_i represents the internal inductance of the conductor in (H), and ω represents the angular-frequency in (rad/s). Equation (28) demonstrates that the resistance and the internal reactance of plane conductors are equal at any frequency [40]. This simply means that the resistance of the plane conductor is not affected by the attenuation of fields or the

exponential decrease in current density within the conductor volume. Therefore, the resistance of the plane conductor is the same value at high frequency as it is at DC. In this case, the current is assumed to be uniformly distributed over the skin depth δ [40].

3.3.2. Impedance Approximations for Round Wires

In contrast to infinite plane conductors, the impedance of finite, practical conductors demonstrates significant frequency dependence. This dependence has been quantified in the literature for wires having circular cross section of finite radius. For this type of conductor, the skin effect causes a significant difference between the internal impedance at DC and the internal impedance at high frequency. As will be shown, the resistance increases with frequency in a predictable fashion, while the inductance decreases with frequency, also in a predictable fashion.

3.3.2.1. Low-Frequency Approximation

At low frequency, the internal impedance of round wires is given as [40]:

$$Z_i \approx \frac{1}{\pi {r_0}^2 \sigma}\left[1 + \frac{1}{48}\left(\frac{r_0}{\delta}\right)^2\right] + j\frac{\omega\mu}{8\pi} \tag{29}$$

where Z_i represents the low-frequency approximation of internal impedance in (Ω/m), r_0 represents the radius of the wire cross-section in (m), σ represents the conductivity in (S/m), δ represents the skin-depth in (m), ω represents the angular-frequency in (*rad/s*), and μ represents the permeability of the medium in (H/m). Comparing Equation (29) with Equation (26), it is apparent that the low-frequency resistance (R_s) and internal reactance (ωL_i) for round wires can be individually represented as:

$$R_{lf} \approx \frac{1}{\pi {r_0}^2 \sigma}\left[1 + \frac{1}{48}\left(\frac{r_0}{\delta}\right)^2\right] \tag{30}$$

$$(L_i)_{lf} \approx \frac{\mu}{8\pi}\ H/m \tag{31}$$

where R_{lf} represents the low-frequency approximation of resistance in (Ω/m), and $(L_i)_{lf}$ represents the low-frequency approximation of internal inductance in (H/m). Therefore, for a round cross-section copper conductor with permeability (μ) of $4\pi \times 10^{-7}\ H/m$, the low-frequency internal inductance is approximately 50 nH per meter [40]. In addition, Equation (31) shows that this low-frequency approximation for internal inductance is frequency-independent. This represents the major limitation of this approximation - it is not adequate for predicting the inductance across a wide frequency range.

3.3.2.2. High-Frequency Approximation

At high frequency, the internal impedance of round wires is given as:

$$(Z_i)_{hf} = \frac{j(j)^{-1/2}}{\sqrt{2}\pi r_0 \sigma\delta} = \frac{(1+j)R_s}{2\pi r_0} \quad \Omega/m \tag{32}$$

where $(Z_i)_{hf}$ represents the high-frequency approximation of internal impedance in (Ω/m), r_0 represents the radius of the wire cross-section in (m), σ represents the conductivity in (S/m), δ represents the skin-depth in (m), and R_s represents the resistance at the surface in (Ω/m). Comparing Equation (32) with Equation (26), it is apparent that the high-frequency resistance (R_s) and internal reactance (ωL_i) for round wires can be represented as:

$$R_{hf} = (\omega L_i)_{hf} = \frac{R_s}{2\pi r_0} \qquad \Omega/m \tag{33}$$

By subject of formula, the high-frequency internal inductance can be represented as:

$$(L_i)_{hf} = \left(\frac{\mu}{16\sigma\pi^3 f {r_0}^2}\right)^{1/2} \qquad H/m \tag{34}$$

where R_{hf} represents the high-frequency approximation for resistance in (Ω/m), σ represents the conductivity in (S/m), f represents the high-frequency in (Hz), μ represents the permeability of the medium in (H/m), r_0 represents the radius of the wire cross-section in (m), R_s represents the surface resistance in (Ω), $(L_i)_{hf}$ represents the high-frequency internal inductance in (H/m), and $(\omega L_i)_{hf}$ represents the high-frequency internal reactance in (Ω/m). Equation (33) implies that the internal reactance and the internal resistance of round wires are equal only at high frequency.

3.3.3. Arbitrary Frequency Internal Impedance Expression

Equation (29) and Equation (32), which represent the low-frequency and high-frequency internal impedance approximations for round wires, respectively, are not sufficient to describe the internal impedance of round conductors across frequency. A more detailed expression which defines the internal impedance for round wires across a wide range of frequencies is given in Equation (35) as [40]:

$$Z_i = R + j\omega L_i = \frac{jR_s}{\sqrt{2}\pi r_0}\left[\frac{Ber\ q + j\ Bei\ q}{Ber' q + j\ Bei\ q}\right] \tag{35}$$

where the parameter q is a dimensionless quantity, which is defined in Equation (36).

$$q = \frac{\sqrt{2}\, r_0}{\delta} \tag{36}$$

Also, the Bessel functions for a complex argument with constituent parts *Ber* and *Bei* are defined as:

$$J_0(j^{-1/2}x) = Ber(x) + j\ Bei(x) \tag{37}$$

where the function $J_0(x)$ represents the Bessel function of the first kind and zero order, $Ber(x)$ represents the real part of $J_0(j^{-1/2}x)$, and $Bei(x)$ represents the imaginary part of $J_0(j^{-1/2}x)$. The function $J_0(x)$ is defined in Equation (38) as:

$$J_n(x) = \left(\frac{x}{2}\right)^n \sum_{k=0}^{\infty} \frac{-1^k x^{2k}}{2^{2k}(k!)(n+k)!} \tag{38}$$

where n represents the Bessel function order, x represents the function or argument, and k represents the summation index terms starting from zero. Similarly, the differential form of equation (37) is given as:

$$Ber'\, x + j\, Bei' x \;=\; \frac{d}{dv}\left(Ber(x) + j\, Bei(x)\right) =\; j^{-1/2} J'_0(j^{-1/2}x) \tag{39}$$

where $Ber'\,(x)$ represents the real part of $j^{-1/2}J'_0(j^{-1/2}x)$, and $Bei'\,(x)$ represents the imaginary part of $j^{-1/2}J'_0(j^{-1/2}x)$. An in-depth treatment of Bessel functions is beyond the scope of this thesis. For a comprehensive detailed treatment of Bessel functions, please refer to [40]. Nevertheless, Bessel functions provide a useful means for predicting the impedance of practical conductors across frequency. Accordingly, the resistance and internal reactance of round wires for arbitrary frequency is given by Equation (40) and Equation (41), respectively [40].

$$R = \frac{R_s}{\sqrt{2}\pi r_0}\left[\frac{Ber\; q\; Bei' q - Bei\; q\; Ber' q}{(Ber'\, q)^2 + \,(Bei'\, q)^2}\right] \Omega/m \tag{40}$$

$$\omega L_i = \frac{R_s}{\sqrt{2}\pi r_0}\left[\frac{Ber\; q\; Ber' q + Bei\; q\; Bei' q}{(Ber'\, q)^2 + \,(Bei'\, q)^2}\right] \Omega/m \tag{41}$$

The range of validity for the low-frequency approximations of conductor resistance and internal reactance given in Equation (30) and Equation (31), respectively, can be assessed by normalizing the generalized expressions of Equation (40) and Equation (41) by the corresponding DC values of these quantities [40]. These normalized representations are given as:

$$R_{lf-norm} = \; R/R_0 \tag{42}$$

$$L_{i-lf-norm} = \; L_i/(L_i)_0 \tag{43}$$

$$\omega L_{i-lf-norm} = \omega L_i / R_0 \quad (44)$$

where $R_{lf-norm}$ represents the low-frequency normalized AC resistance of Equation (40), R represents the AC resistance of Equation (40), R_0 represents the DC resistance of Equation (30), $L_{i-lf-norm}$ represents the low-frequency normalized internal inductance of Equation (41), L_i represents the internal inductance of Equation (41), $(L_i)_0$ represents the DC internal inductance of Equation (31), $\omega L_{i-lf-norm}$ represents the low-frequency normalized internal reactance of Equation (41), and ωL_i represents the internal reactance of Equation (41). Figure 12 provides a plot of the low-frequency normalized quantities defined in Equation (42), Equation (43), and Equation (44) as a function of frequency. In this plot, the frequency axis is represented as the ratio of conductor radius to skin depth (r_0/δ). It is noted that this ratio is small at low frequency because the skin depth is large; whereas this ratio grows quickly as frequency increases due to the accompanying reduction in skin depth.

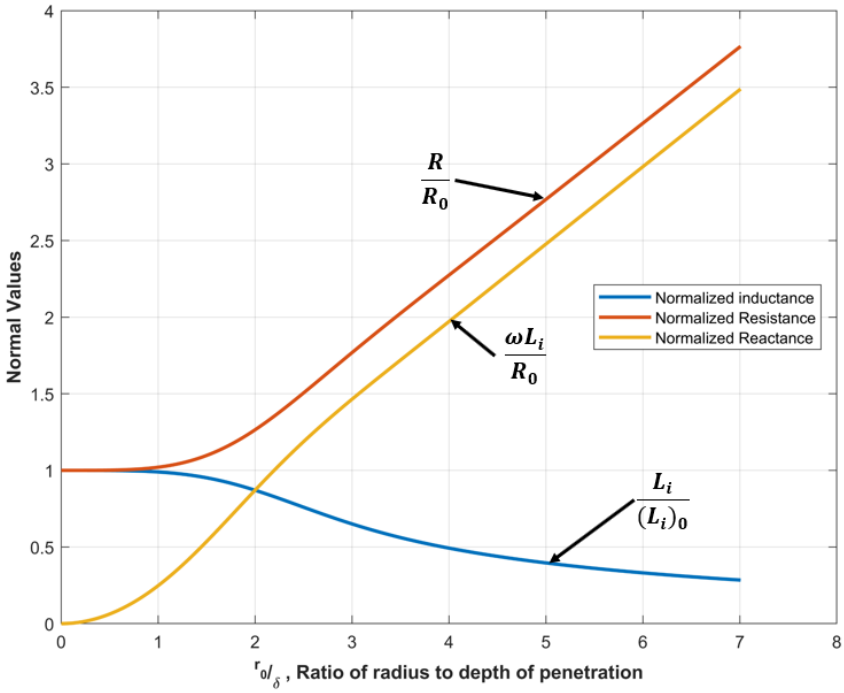

Figure 12: Solid- wire Skin effect quantities compared with dc Values [40]

As shown in Figure 12, at low-frequency, when the conductor radius is less than the skin-depth ($r_0/\delta < 1$), the current is uniformly distributed over the conductor cross-section. Hence, the resistance and internal inductance are constant with frequency, at DC approximate values. However, at high-frequencies, when the conductor radius is greater than the skin-depth ($r_0/\delta > 1$), the current is concentrated at the surface of the conductor because the skin-depth decreases with the square-root of frequency ($\delta \propto 1/\sqrt{f}$). The resistance and inductance are not equal in this case. Due to skin effect, the high-frequency resistance increases with the square-root of frequency ($R \propto \sqrt{f}$), while the high-frequency internal inductance decreases with the square-root of frequency ($L_i \propto 1/\sqrt{f}$) [66].

Similarly, the range of validity for the high-frequency approximations of conductor resistance and internal reactance given in Equation (33) can be assessed by normalizing the

generalized expressions of Equation (40) and Equation (41) by the corresponding high-frequency resistance of Equation (33) [40]. These normalized representations are given as:

$$R_{hf-norm} = R/R_{hf} \tag{45}$$

$$\omega L_{hf-norm} = \omega L_i/R_{hf} \tag{46}$$

where $R_{hf-norm}$ represents the high-frequency normalized AC resistance of Equation (40), R represents the AC resistance of Equation (40), R_{hf} represents the high-frequency approximation of Equation (33), $\omega L_{hf-norm}$ represents the high-frequency normalized internal reactance of Equation (41), and ωL_i represents the internal reactance of Equation (41). Figure 13 provides a plot of the high-frequency normalized quantities defined in Equation (45) and Equation (46) as a function of frequency. In this plot, the frequency axis is again represented as the ratio of conductor radius to skin depth (r_0/δ).

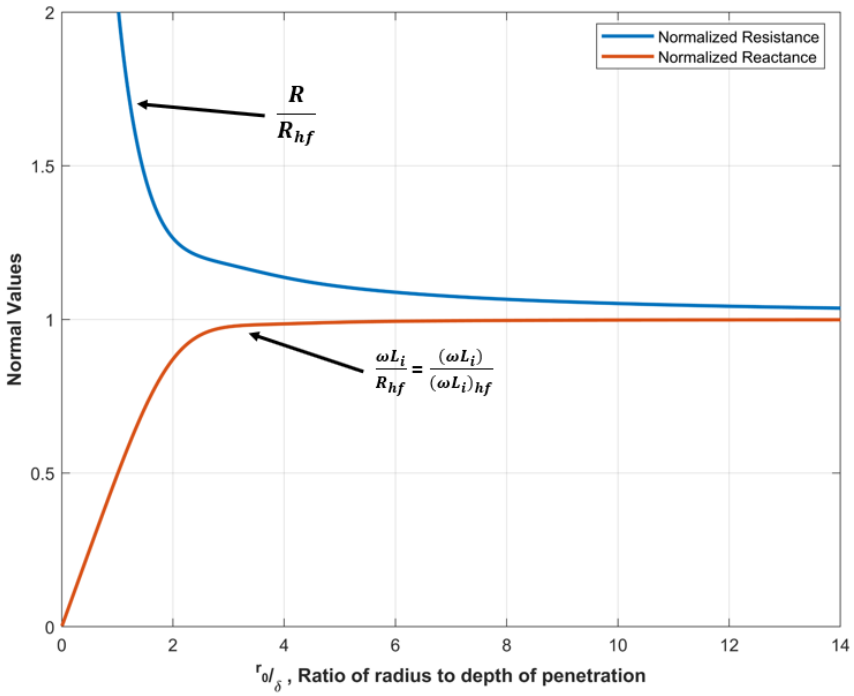

Figure 13: Solid-wire skin effect quantities compared with values from high frequency formula [40]

Figure 13 can be used to determine the frequency range over which it is permissible to apply the high-frequency approximations for resistance and internal inductance given by Equation (33). For a well-developed skin effect model, the real and imaginary components of conductor impedance are expected to be approximately equal at high frequency [41], [66], [116]. Therefore, as shown in Figure 13, the high-frequency approximation of Equation (33) can be used with reasonable accuracy for frequencies at which the wire radius is at least five times larger than the skin-depth ($r_0/\delta > 5$). The high-frequency approximations of Equation (33) become gradually more accurate at higher frequencies, as the skin depth is further reduced. The accurate frequency range over which it is permissible to apply both the low and high-frequency approximations for resistance and internal reactance is provided in Chapter 4 of this thesis.

3.3.4. External Self-Inductance of a Circular Loop.

As discussed previously, total loop inductance or self-inductance includes a contribution of the internal and the external inductance. Treatment of internal inductance of round wires has been provided in the preceding section. Therefore, this section presents a treatment of the external inductance a circular loop formed by round wire.

The external contribution to self-inductance can be obtained by calculating the induced fields at the surface of the conductor. For this analysis to apply, the radius of the loop r must be large as compared to the radius of the conductor cross-section a, as shown in Figure 14(a). Under this constraint, the fields around the conductor are nearly the same as though the current is concentrated along the central axis of the wire [40]. In this case, the external inductance is well approximated by the mutual inductance of the filamentary loop as shown in Figure 14(b).

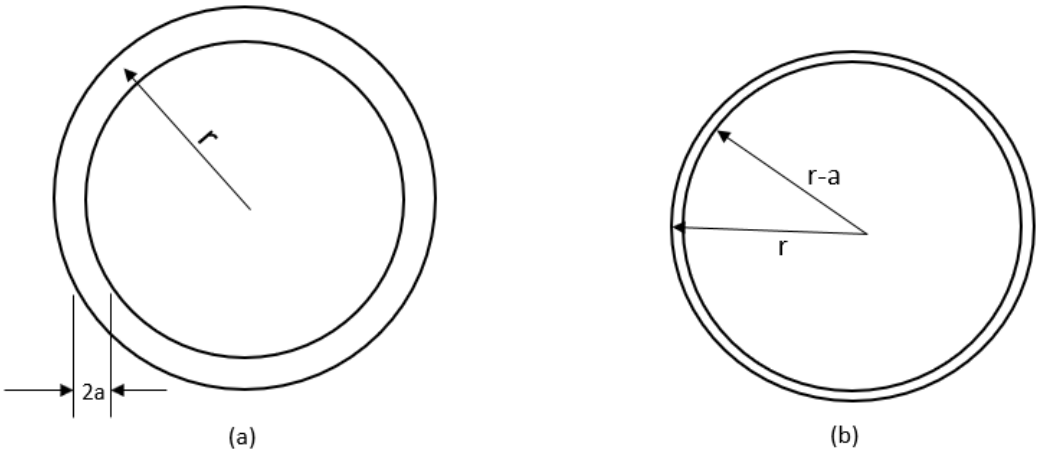

Figure 14: (a) Conducting loop of wire used for calculating external inductance; (b) Filamentary loops, through the center and the other along inside edge, for which mutual inductance is calculated [40]

The external inductance of the wire loop is approximated by utilizing the mutual inductance between the two concentric circles of Figure 14(b), which is given by Equation (47) [40][47].

$$L_{external} \cong r\mu\left[ln\left(\frac{8r}{a}\right) - 2\right] \qquad r \gg a \tag{47}$$

Equation (11) defined total self-inductance as the sum of the internal and external self-inductance components. Thus, the value obtained from Equation (47) must be summed with the internal inductance obtained from Equation (41) to give the total inductance of the loop. Grover also provides a circular loop inductance approximation, which includes the contribution of both the internal and external fields for the circular loop [112]:

$$L_{loop} = 4\pi n^2 a\left\{\left(1 + \frac{r^2}{8a^2}\right)\cdot \ln\frac{8a}{r} + \frac{r^2}{24a^2} - 1.75\right\} \tag{48}$$

where a is the radius of radius of the coil in (*cm*); r is the radius of the conductor cross-section in (*cm*); n is the number of turns in the coil; and L_{loop} is expressed in (*nH*). The accuracy of this expression depends on the ratio of the conductor radius to the coil radius (r/a) [112]. Highest accuracy is obtained for large coils constructed with thin wire: $(r/a) \rightarrow 0$. It is also noted that Equation (48) does not include frequency dependence. Accordingly, this expression is only valid as a low-frequency approximation of the inductance of a circular loop.

3.3.5. Self-Inductance of a Rectangular loop.

The second important test case considered in this thesis is a rectangular loop structure with a closely spaced return conductor. To provide a starting reference for evaluating the impedance of this test case, this section presents a treatment of the external inductance for a rectangular loop of length l and width w, as shown in Figure 15. The conductors of the loop are wires with cross-sectional radius r_w. The magnetic flux density B shown in Figure 15 is contained in the open surface surrounded by the rectangular loop. At low frequency, the current is expected to be uniformly distributed across the cross-section of the circular conductor, which has a diameter of $2r_w$ [47].

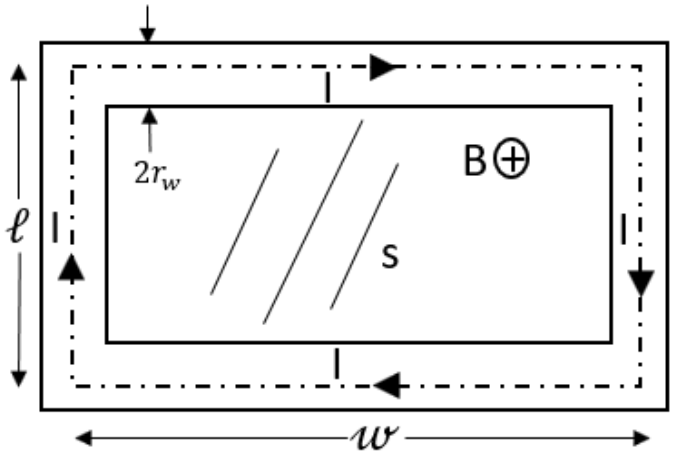

Figure 15: Rectangular loop case for computing external inductance [47]

For the case in which the loop dimensions l and w are much larger than the wire radius r_w, the external inductance of the rectangular loop can be computed as [47]:

$$L_{loop} \cong \frac{\mu_o}{\pi}\left[-l\ \ln\left(1+\sqrt{1+\left(\frac{w}{l}\right)^2}\right)-w\ ln\left(\left(1+\sqrt{1+\left(\frac{l}{w}\right)^2}\right)\right)+l\ ln\frac{2w}{r_w}\right. \tag{49}$$

$$\left.+w\ ln\frac{2l}{r_w}+2\sqrt{l^2+w^2}-2w-2l\right] \qquad l,w \gg r_w$$

where dimensions l and w are the width and length of the rectangular loop in (*mm*), r_w represents the radius of the conductor cross-section in (*mm*), and μ_o represents the permeability of free space in (*H/m*). It is also noted that Equation (49) does not include frequency dependence. Accordingly, this expression is only valid as a low-frequency approximation of the inductance of a rectangular loop.

In the geometry shown in Figure 15, when the return circuit is separated by a large distance from the forward path, the current distribution in the conductor will not be affected by proximity effect. However, for the case in which the forward and return path of the rectangular conductor are in close proximity, the uniform distribution of current in the loop will be distorted at high frequency. For this thesis, rectangular conductors with closely spaced return paths will be used to show the impact of proximity effect. Proximity effect is very difficult to model and quantify using analytical expressions. However, FEA analysis tools can be employed to gain significant insight into the impact of proximity effect. Accordingly, an in-depth study of both the skin effect and the proximity effect using FEA analysis software is presented in Chapter 4 of this thesis.

CHAPTER 4:

FEA ANALYSIS USING COMSOL MULTI-PHYSICS

Finite element analysis (FEA) makes the modeling of devices and systems possible in a virtual environment, for the purpose of solving and analyzing problems in many different fields of study. For the purpose of this thesis, COMSOL Multiphysics [117] will be used to analyze and study different conductors and to extract their associated impedances. This software allows users to build models, define material properties, specify constraints, define. With COMSOL Multiphysics, a variety of different studies may be performed, such as frequency analysis studies, stationary and time-dependent studies, coil analysis studies, fatigue analysis studies, and eigenfrequency analysis studies.

One advantage of using COMSOL Multiphysics is that it allows problems to be solved in either a two-dimensional or three-dimensional workspace. In addition, it is possible to directly import geometry data from various CAD software packages into COMSOL. Another advantage of COMSOL is that the user does not need an in-depth knowledge of the physics formulations used by the simulation study in question. For example, in-depth knowledge of Maxwell's equations and their interpretations is not required to solve electromagnetics problems in COMSOL Multiphysics. A screenshot of the COMSOL simulation environment is shown in Figure 16.

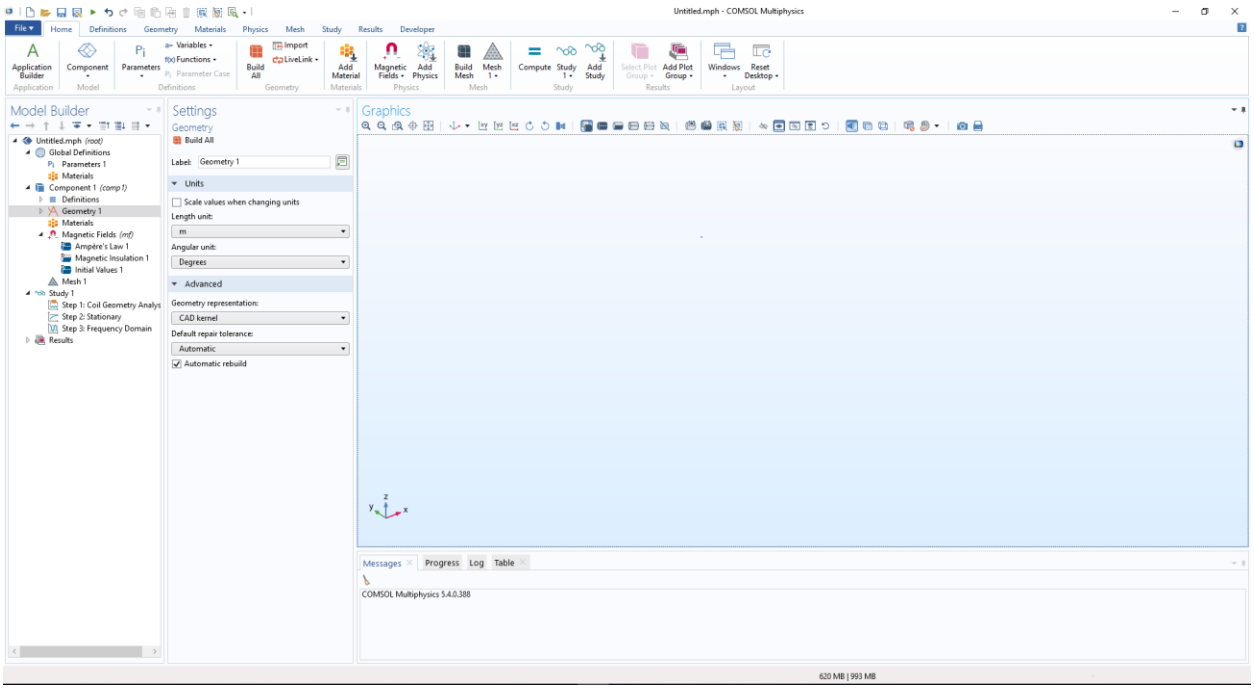

Figure 16: Screenshot of COMSOL Multiphysics environment

Most of the calculations and theoretical formulations presented in Chapter 3 will be demonstrated in this chapter. The model geometry for all test cases will be built in the COMSOL Multiphysics environment using the AC/DC physics application module. In this application module, several sets of equations are available to solve alternating current and direct current problems. For studies involving electromagnetic field analysis around conductor coils, either the Magnetic and Electric Fields (mef) physics configuration, or the Magnetic fields (mf) physics configuration can be used [117]. Study goals relating to electromagnetic waves can be realized by using either option. The mf physics configuration employs the A formulation for solving the magnetic vector potential, while the mef physics configuration employs the A-V formulation for solving the magnetic vector potential and electrical scalar potential. The electric scalar potential is not required for this study. Also, compared to mef physics, mf physics converges faster, consumes less memory, and adequately describes field effects around conductor coils. For these reasons, the mf physics configuration will be used for this study.

4.1. Simulation Study Test Subject

This section includes a list of the different test cases intended for study throughout this chapter as well as the remainder of this thesis. In general, three categories of geometry are considered in this study: circular loop conductors, straight conductors, and rectangular loop conductors. The circular loop geometries (Geometry 1 to Geometry 5 in Table 4), provide the opportunity to study the influence of skin effect alone, without the contribution of proximity effect. Each individual radius of Geometry 1 to Geometry 5 was chosen to achieve a specific target inductance value or target circumference. The straight conductor geometries (Geometry 6 and Geometry 7A-7C in Table 4) present the opportunity to study the influence of proximity effect within a simplified geometry. The simplicity of this geometry facilitates the study of conductor spacing on inductance as well as the field distribution around the conductors. The rectangular loop geometries (Geometry 8 to Geometry 14 in Table 5), provide the opportunity to study proximity effect in combination with skin effect. With this geometry, a return path is positioned close to the forward current path in order to emphasize the influence of proximity effect. To ensure consistency in the rectangular loop study between the COMSOL models and the analytical definition of Equation (49), the definitions for length (l) and width (w) for the rectangular geometry are defined as shown in Figure 17 (a) and Figure 17(b).

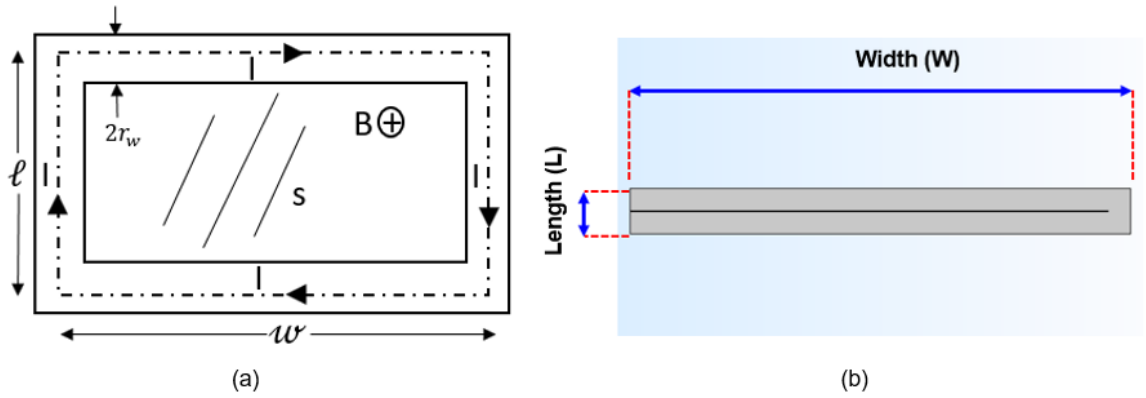

Figure 17: (a) Rectangular loop from Chapter 3:, and (b) Rectangular loop used in COMSOL

TABLE 4
SUMMARY OF CIRCULAR TEST SUBJECTS

Device Under Test	**Loop Radius [cm]**	**Geometry Study Purpose**	**Nomenclature Used**
One-meter Round Loop	15.92	Validate Analytical Models	Geometry 1
Round loop 1	5.65	Skin Effect	Geometry 2
Round loop 2	4.65	Skin Effect	Geometry 3
Round Loop 3	4.19	Skin Effect	Geometry 4
Round Loop 4	3.30	Skin Effect	Geometry 5
Single One-meter Straight Conductor	N/A	Demonstrate Proximity Effect	Geometry 6
Dual One-meter Straight Conductors [5 cm apart]	N/A	Demonstrate Proximity Effect	Geometry 7A
Dual One-meter Straight Conductors [8 cm apart]	N/A	Demonstrate Proximity Effect	Geometry 7B
Dual One-meter Straight Conductors [15 cm apart]	N/A	Demonstrate Proximity Effect	Geometry 7C

A summary of the rectangular loop geometries and dimensions is given in Table 5. A sweep of the geometry length is performed using Geometry 8 to Geometry 11. A sweep of the geometry width is performed using Geometry 10, Geometry 12, Geometry 13, and Geometry 14.

TABLE 5
RECTANGULAR LOOP TEST SUBJECTS

Width (W) [mils]	**Length (L) [mils]**	**Geometry Study Purpose**	**Nomenclature Used**
7500	700	Proximity Effect	Geometry 8
7500	500	Proximity Effect	Geometry 9
7500	300	Proximity Effect	Geometry 10
7500	200	Proximity Effect	Geometry 11
6500	300	Proximity Effect	Geometry 12
5500	300	Proximity Effect	Geometry 13
4500	300	Proximity Effect	Geometry 14

4.2. COMSOL Analysis and Impedance Extraction of Geometry 1

The goal of this chapter is to use COMSOL models to validate the analytical treatment of inductance and resistance presented in Chapter 3. This chapter also serves as a stepping-stone to the final validation of the presented models in Chapter 5. Therefore, the theories proposed by S. Ramo et al. [40] will be validated in this chapter. Skin and proximity effect in conductors and the resulting frequency-dependence of inductance and resistance due to both effects will also be demonstrated.

It is well established in the literature that the low-frequency internal inductance of a round wire is approximately $50\ nH/m$ [40], [47], [114]. Therefore, for a circular loop composed of one meter of round wire, the internal inductance at DC is expected to be 50 nH. Recall that the analytical treatment of internal inductance and resistance presented in Chapter 3 was demonstrated using a one-meter length of round conductor. Therefore, for the first step in this simulation study, a one-meter length of round conductor formed into a circular loop (Geometry 1) was built in COMSOL in order to achieve the target internal inductance of 50 nH. To achieve this goal, a circumference of 1-meter was realized with a loop radius of 0.1592 meters (15.92 cm). Several steps were required to implement this model in COMSOL.

First, a coil sketch of radius $15.92\ cm$ was designed in the COMSOL 2-D workspace as shown in Figure 18.

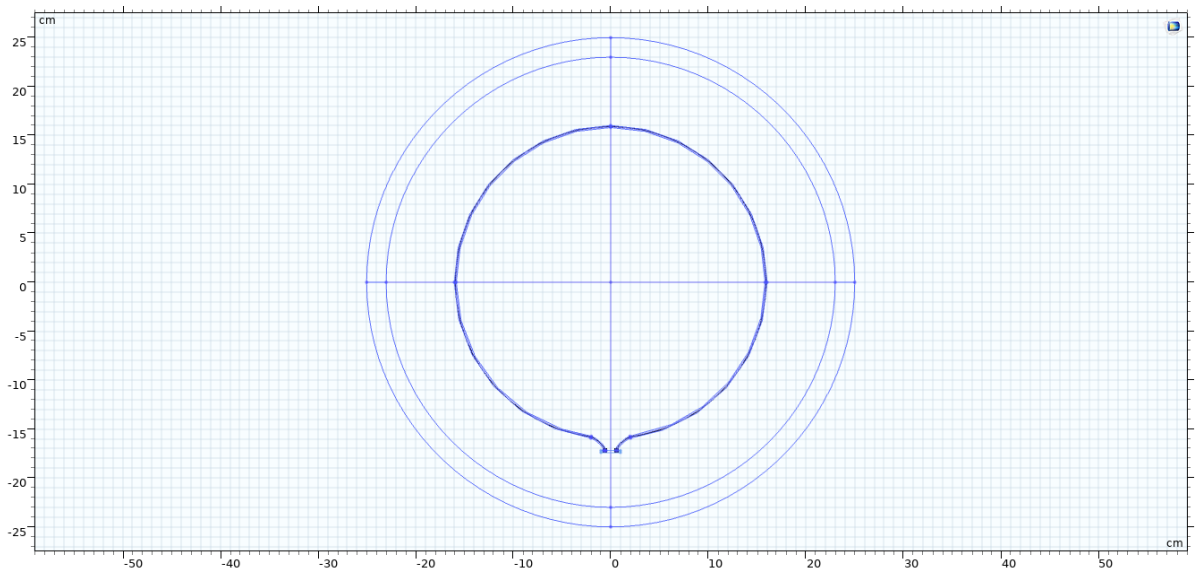

Figure 18: Initial circular coil 2-D sketch

Second, a circular cross-section was sketched perpendicular to one end of the helix shape of one turn as shown in Figure 19. The diameter of this circular cross-section is 2.052 $[mm]$, which represents size 12 in the standard American Wire Gauge (AWG). Standard AWG 12 wires are also used in the experimental section of Chapter 5.

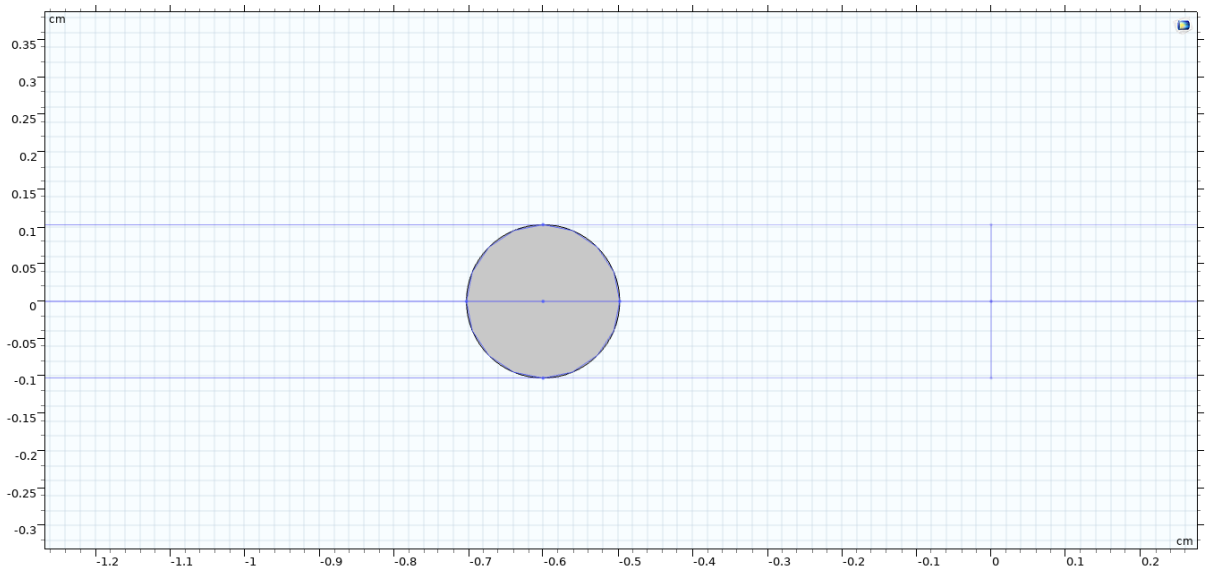

Figure 19: Loop cross-section to be swept through the loop path

Third, using the sweep feature in COMSOL, the circular cross-section shown in Figure 19 was swept through the one-turn coil geometry shown in Figure 18. The final product of these geometry manipulations is shown in Figure 20.

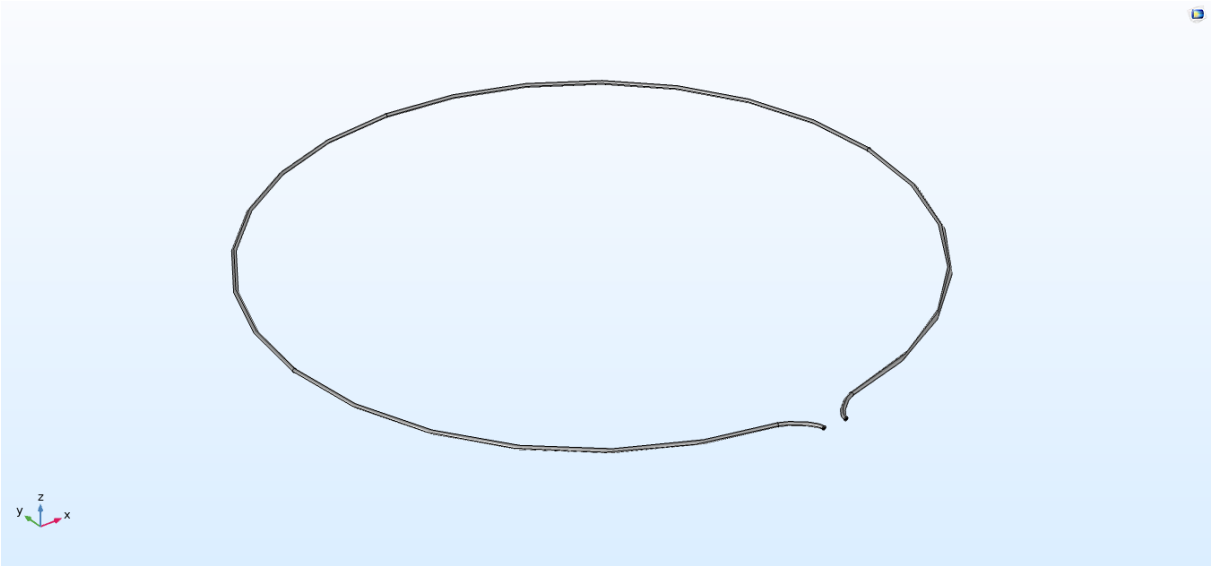

Figure 20: Finalized one-meter conductor loop built in COMSOL

Fourth, because inductance is only defined for a closed loop, a shorting envelope was placed across both terminals of the conductor as shown in Figure 21. This is a necessary step to complete the circuit for current conservation. If this step is omitted, the necessary input and output coil excitation conditions cannot be defined. The input and output conductor boundary conditions for conservation of current are shown in Figure 22.

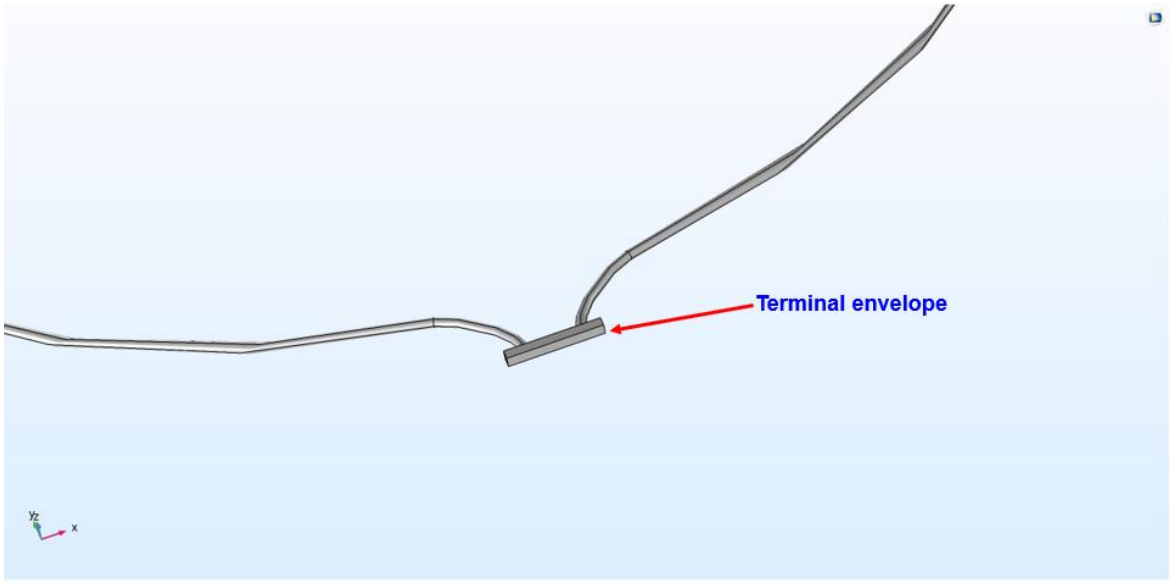

Figure 21: Placing a shorting envelope between terminals for vacuum provision

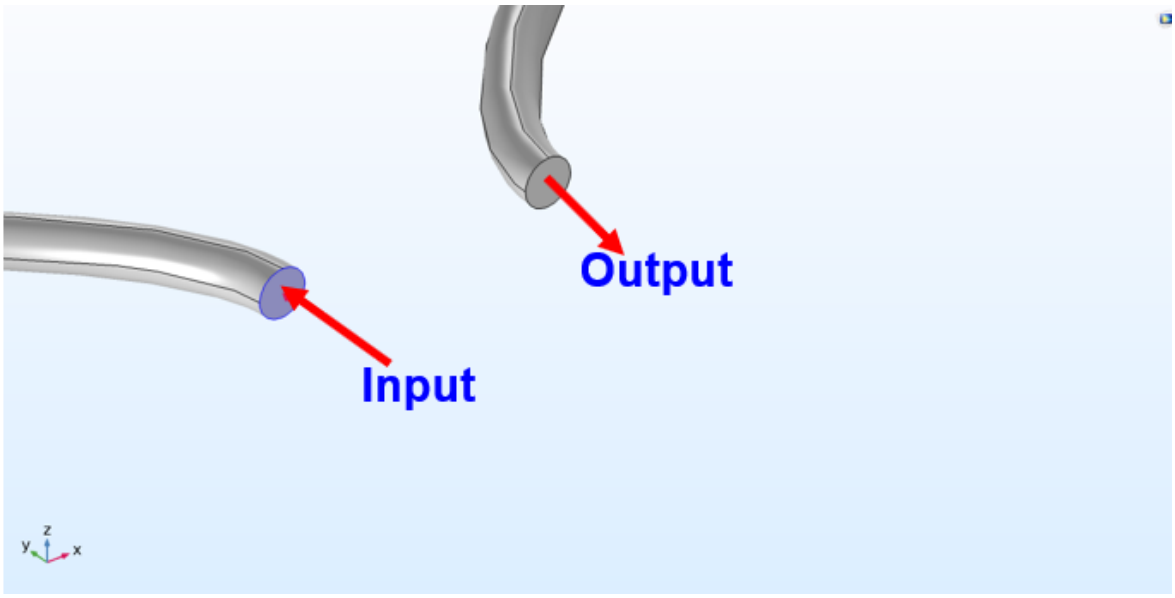

Figure 22: Input and Output specification for current conservation

Fifth, boundary conditions were defined. For this purpose, a magnetic insulation envelope was provisioned around the conductor in the shape of a sphere. This sphere serves as a gaussian surface around the conductor for preservation of Gauss's law for the magnetic and electric fields. An infinite element domain was created at the outer boundary of this sphere. The infinite element domain (IED) is used because it provides better simulation accuracy as compared to an ordinary magnetic insulation (MI) boundary condition [118]. With the MI boundary condition, the size of the air-box is a parameter of sensitivity. The air-box has to be built large enough to capture the total magnetic lines of flux required for better simulation result accuracy. This leads to an increase in memory requirements and meshing problems. With the IED configuration, the conductor is modeled as existing in a space which extends to infinity and contains nothing else. By using the IED, the size of the air-box is not a parameter of sensitivity. All the required magnetic flux lines are captured in the simulation. Figure 23 shows a screen shot of the IED implemented with a radius of 25 cm around Geometry 1. Using an IED ensures that the size of the Gaussian surface is not critical to the accuracy of simulation results.

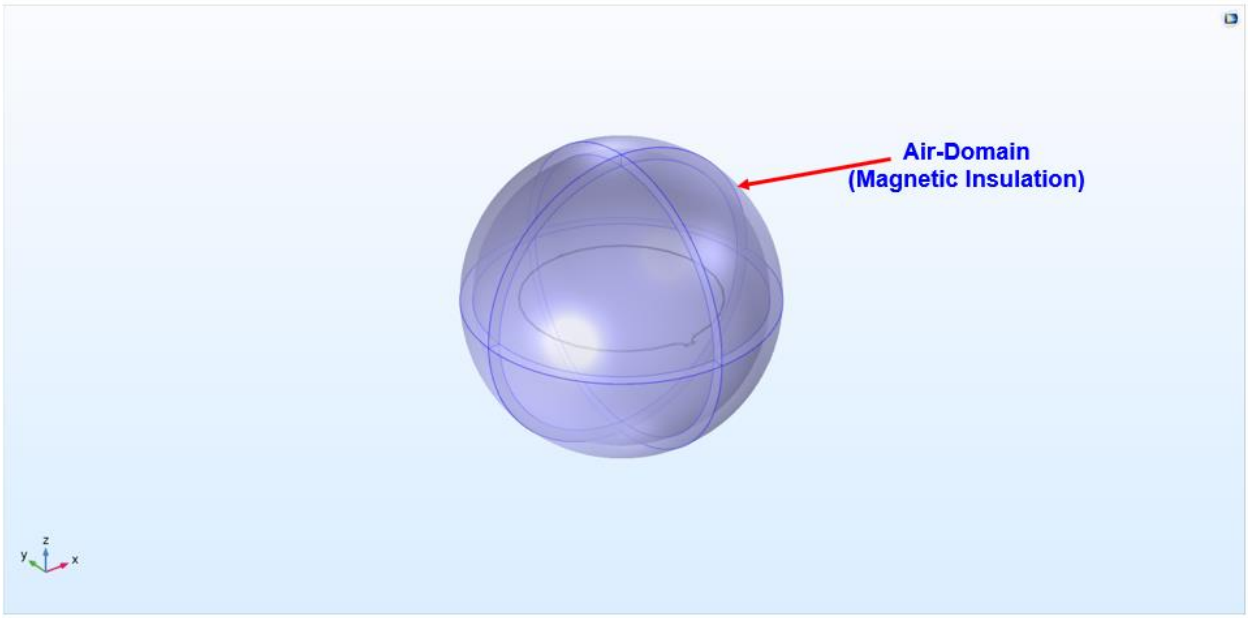

Figure 23: Infinite-element air-domain for Magnetic Insulation provision

Sixth, the material properties for all elements in the simulation environment were specified, and an electrical stimulus was configured. Copper is specified for the conducting material; vacuum is specified for the terminal envelope; and air is specified for the IED around the conductor. For the electrical stimulus, a coil excitation current of 1A was configured for application into one of the terminals, with the other terminal specified as the return.

Seventh, a meshing sequence was applied. Meshing enables the discretization of the geometry into small units of simple shapes, referred to as mesh elements. A free-tetrahedral mesh was applied to all domains to create small discretized polygons. Figure 24 shows a screenshot of the fully meshed geometry.

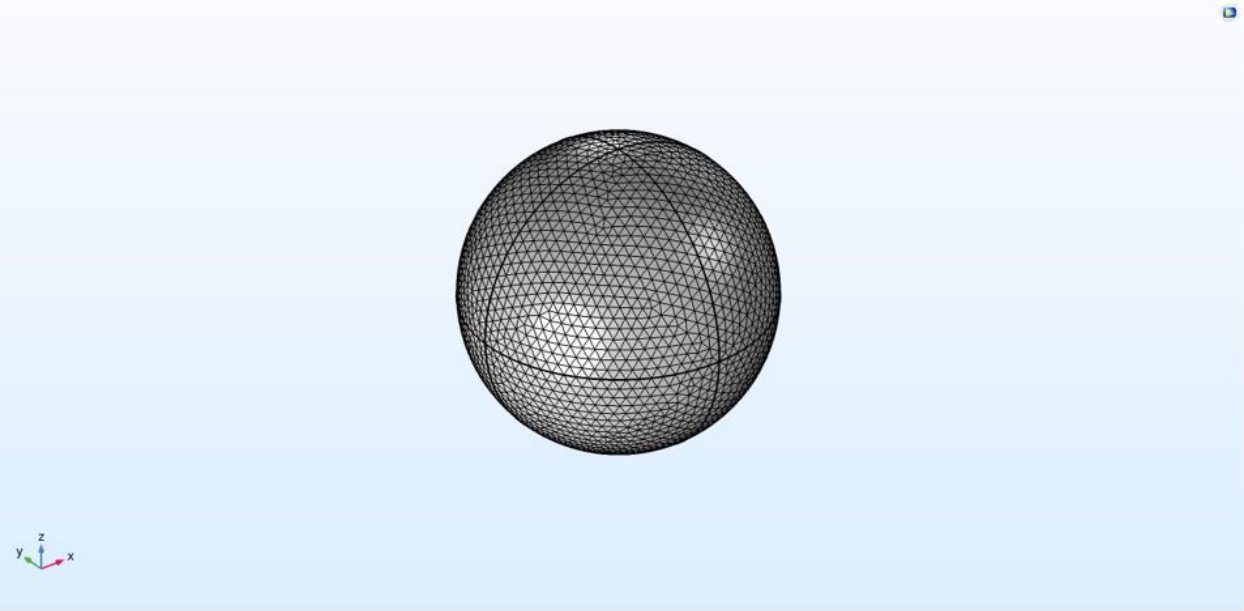

Figure 24: Screenshot of the fully meshed geometry

Eighth, a set of study and solver configuration settings were applied. For this simulation, three individual studies are needed: a coil geometry analysis study, a stationary study, and a frequency-domain study. The coil geometry analysis study specifies the conductor as a coil so that electrical parameters such as inductance, resistance, and voltage can be extracted from the electromagnetic field values computed by COMSOL. The stationary study makes it possible to

determine DC parameter values from the electromagnetic field values computed by COMSOL. Finally, the frequency-domain study makes it possible to evaluate the electrical parameters of the coil across a wide frequency range. A log-spaced frequency sweep from 500 *Hz* to 20 *MHz* with seven steps per decade was applied to the study. This frequency range was selected because the spectral envelope of power electronics applications based on WBG devices is usually dominated by content within this frequency range. After simulation was completed, the resistance and inductance of the coil were extracted from the results node of the COMSOL sequence. The frequency-dependent resistance and inductance values predicted by COMSOL for Geometry 1 are shown in Figure 25 and Figure 26, respectively.

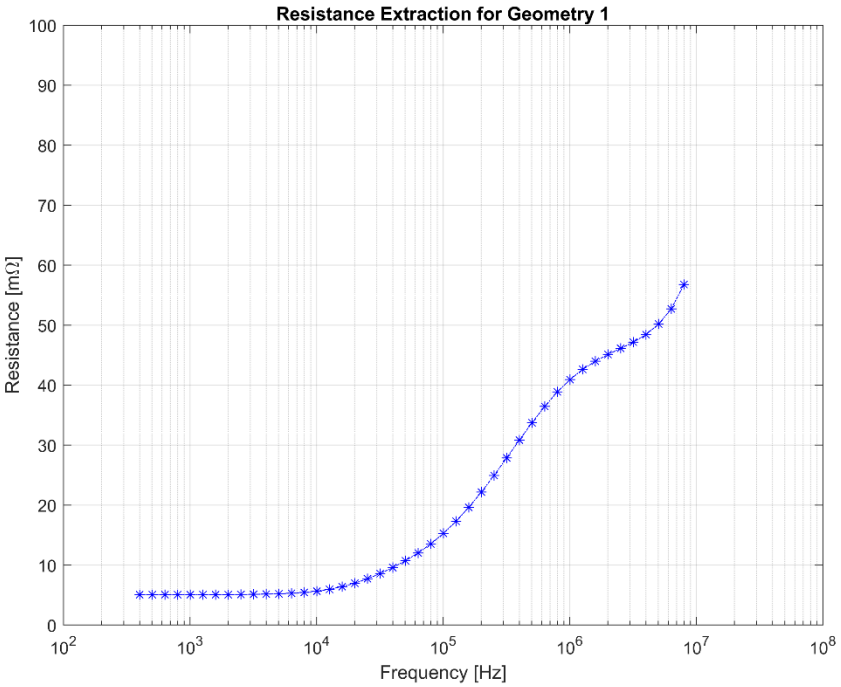

Figure 25: Frequency-dependent Resistance extracted with COMSOL for Geometry 1

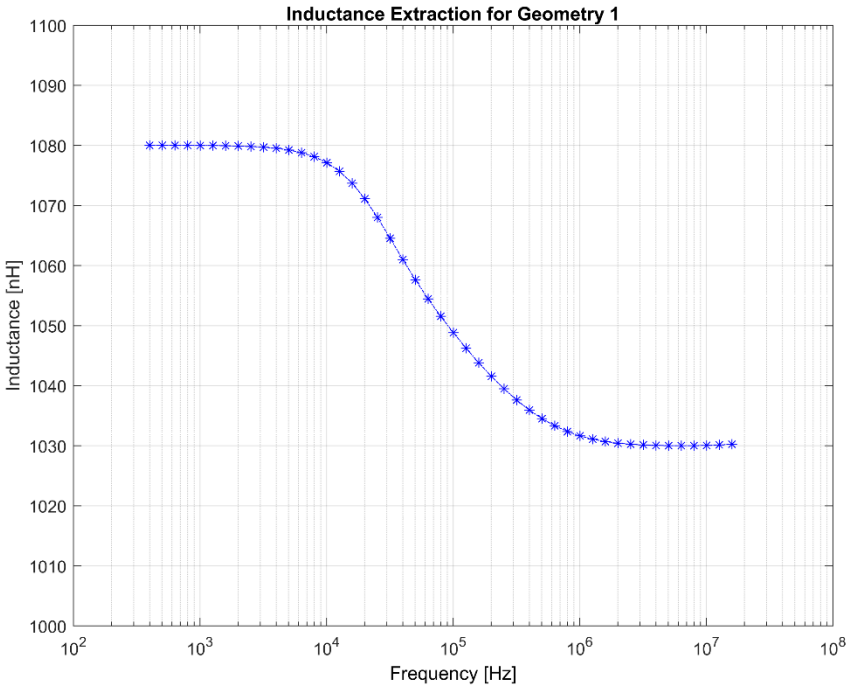

Figure 26: Frequency-dependent Inductance extracted with COMSOL for Geometry 1

The extracted impedance values shown in Figure 25 and Figure 26 are in good agreement with the analytical predictions for the Geometry 1 conductor at low-frequency. At DC, an analytical approximation of the resistance for Geometry 1 is given as:

$$R_i(0) = \rho \cdot {}^{l}/_{A} \tag{50}$$

where $R_i(0)$ represents the DC resistance in (Ω), ρ represents the conductor resistivity of 1.667×10^{-8} in $(\Omega \cdot m)$, l represents the conductor length in (m), and *A* represents the conductor cross-sectional area in (m^2). Also, from Equation (48), the low-frequency approximation of loop inductance provided by Grover [112] is given as:

$$L_{loop}(0) = 4\pi n^2 a \left\{ \left(1 + \frac{r^2}{8a^2}\right) \cdot \ln\frac{8a}{r} + \frac{r^2}{24a^2} - 1.75 \right\} \tag{51}$$

where $L_{loop}(0)$ represents the loop inductance or self-inductance at DC in nH; r represents the radius of the conductor in cm; *a* represents the radius of the coil in cm; and *n* represents the

number of turns in the coil. The accuracy of this low-frequency approximation for self-inductance depends on the ratio of the conductor radius to the coil radius (r/a) [112]. Highest accuracy is obtained for large coils constructed with thin wire (r/a) $\rightarrow 0$. Table 6 compares the low-frequency analytical approximations of Equation (50) and Equation (51) for Geometry 1 with the low-frequency values predicted by COMSOL for the resistance and inductance of this structure, respectively. It is noted that the analytical approximations are in close agreement with the COMSOL predictions at low frequency. Table 6 also includes an inductance estimate for Geometry 1 obtained from an online calculator [119] based on Rosa's approximation for low-frequency inductance [113]. This low-frequency inductance estimate is also in good agreement with the Grover low-frequency approximation from Equation (51).

TABLE 6
ANALYTICAL & COMSOL PREDICTION

	Analytical DC Resistance Prediction [mΩ]	COMSOL DC Resistance Prediction [mΩ]	Analytical DC Inductance Prediction [nH]	COMSOL Inductance Prediction [nH]	Online Inductance Calculator [nH]
Geometry 1	5.20	5.05	1075.00	1080.00	1075.10

4.3. COMSOL Skin and Proximity Effect Analysis

This section analyzes the influence of skin and proximity effects on conductor impedance using COMSOL Multiphysics and also validates the analytical predictions of Equation (40) and

Equation (41). Validation of the analytical predictions of Chapter 3 is necessary to demonstrate accurate implementation of the COMSOL impedance extraction process. This is particularly important in for the extraction of the internal inductance, which is not directly available in the COMSOL results node. The Geometry 1 test case from the previous section will be used as a starting point in the impedance extraction process since analytical analysis has been provided for this geometry.

4.3.1. Skin Effect Demonstration

As mentioned in Chapter 2, due to skin effect, high-frequency current becomes distributed within the conductor such that the current density is highest at the surface of the conductor and decreases progressively toward the center of the conductor. To visualize the impact of skin effect, current density plots were generated in COMSOL for the Geometry 1 test case at different frequencies. These plots are provided in Figure 27 and Figure 28. As shown in Figure 28(a), at $500\ Hz$, the current distribution is uniform across the entire cross-section. As the frequency is increased from $500\ Hz$ to $18\ MHz$, most of the current moves towards the surface of the conductor, with little or no current at the center, as shown in Figure 28(b).

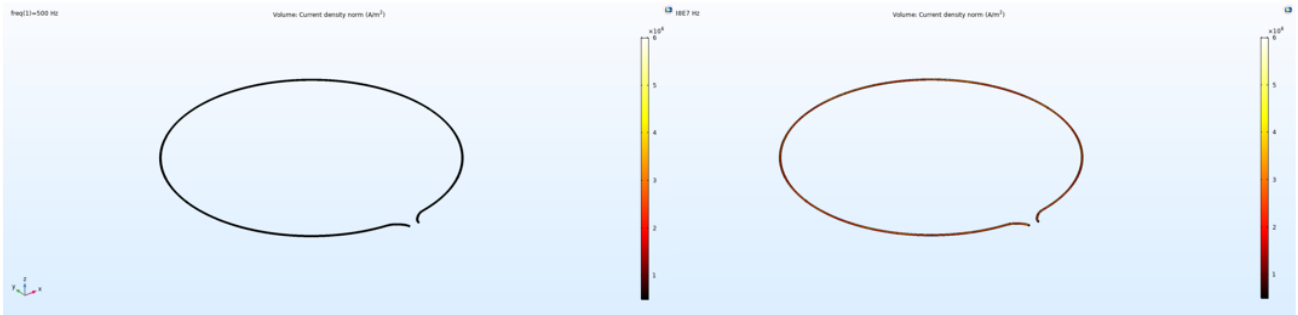

Figure 27: (a) Current density plot @ 500 Hz, (b) Current density plot @ 18 MHz

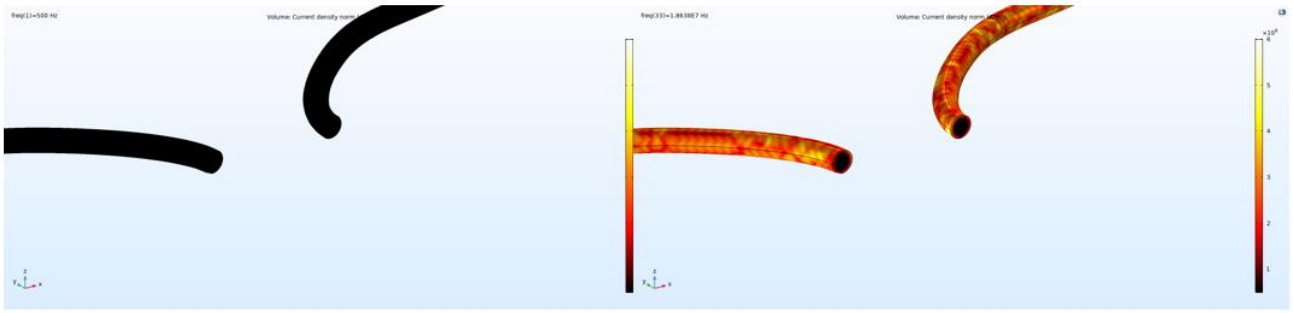

Figure 28: (a) Zoomed-in current density plot @ 500 Hz, (b) Zoomed-in current density plot @ 18 MHz

An analysis of the skin-depth for Geometry 1 was also conducted in COMSOL as part of this study. The extracted values of skin-depth for this geometry are presented in a normalized fashion in Figure 29. Figure 29 demonstrates that the depth of penetration (skin-depth) is reduced as the frequency increases until a point is reached at which there is little or no penetration into the conductor.

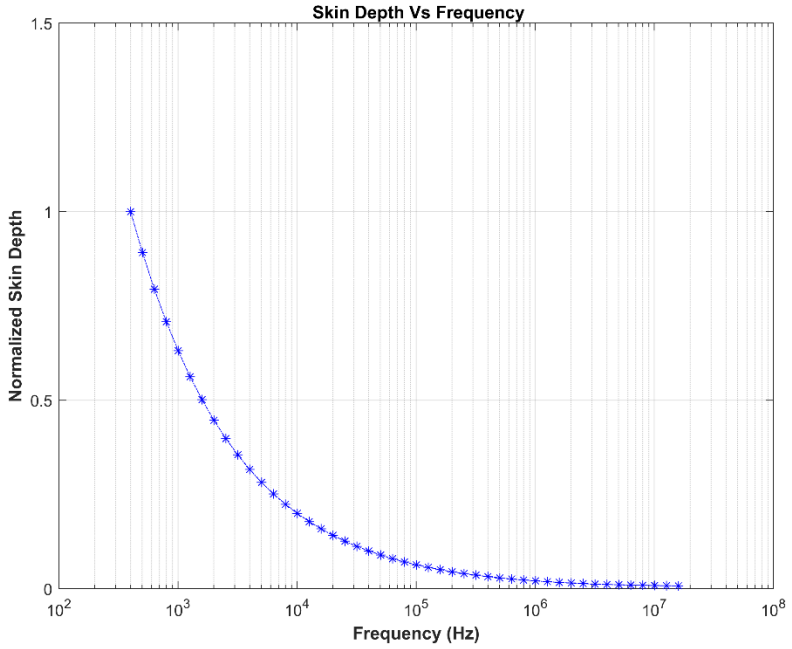

Figure 29: Normalized Skin Depth of Geometry 1

Recall from Chapter 3 that the skin-depth expression of Equation (20) was used to realize the arbitrary frequency approximations for internal impedance, internal resistance and internal reactance provided in Equation (35), Equation (40), and Equation (41), respectively. This implies that skin effect is solely responsible for the frequency-dependence of resistance and internal inductance for the case of a round conductor. As will be shown, this assumption is only valid when the conductor is isolated from other current-carrying conductors. To evaluate the internal impedance of each considered conductor in COMSOL, the following formulas [39] were used:

$$Z_{int} = R_{int} + j\omega L_{int} \tag{52}$$

$$L_{int} = \frac{1}{|I|^2} \int_{cond} \mu \, | \, H \, |^2 \; dS \tag{53}$$

$$R_{int} = \frac{1}{\sigma |I|^2} \int_{cond} | \, J \, |^2 \, dS \tag{54}$$

where Z_{int} represents the internal impedance in ohms (Ω), L_{int} represents the internal inductance in Henries (H), R_{int} represents the internal resistance in ohms (Ω), σ represents the conductivity in siemens per meter (S/m), I represents the total current through the conductor in amperes (A), J represents the current density in amperes per square meter (A/m^2), and H represents the magnetic field intensity in amperes per meter (A/m).

Since resistance is not affected by the fields inside and around the conductor, no separation exists between internal and external resistance. Therefore, internal resistance is the same as total resistance. Resistance is only dependent on the cross-sectional area, the length of the conductor, and the conductor resistivity. On the other hand, inductance is dependent on the fields inside and around the conductor. Therefore, a separation exists between the internal and external inductance. A detailed explanation of this distinction between internal and external inductance is given in Chapter 3.

The internal inductance of the Geometry 1 test case was evaluated in COMSOL by integrating the magnetic field around the conductor as specified by Equation (53). The results from this analysis, which are displayed in Figure 30 below.

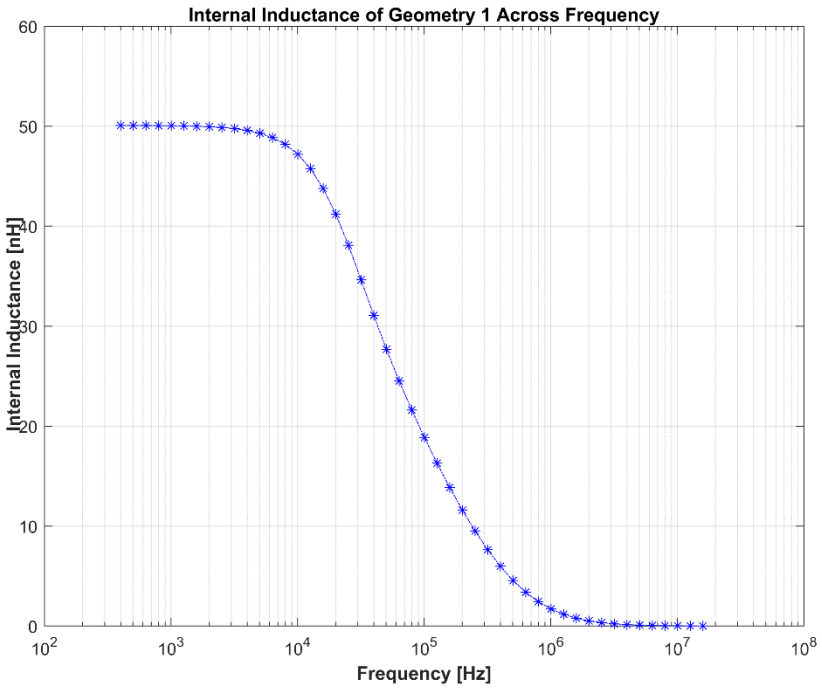

Figure 30: Internal Inductance of conductor loop extracted using COMSOL

The results show that the COMSOL prediction for the internal inductance of Geometry 1 at DC is 50 nH. This value agrees with the analytical approximation of internal inductance provided by Equation (31) at DC for the Geometry 1 conductor length of one meter.

Table 7 provides a summary of the internal inductance and resistance estimates determined for the Geometry 1 test case, both from the analytical approximations of Chapter 3 and from the COMSOL model analysis included in this chapter. It is noted that both methods produce nearly identical estimates for internal inductance and resistance.

TABLE 7
ANALYTICAL & COMSOL PREDICTION

	Analytical DC Resistance Prediction [mΩ]	COMSOL DC Resistance Prediction [mΩ]	Analytical DC Internal Inductance Prediction [nH]	COMSOL DC Internal Inductance Prediction [nH]
Geometry 1	5.20	5.05	50.00	50.07

It is noted that the Ramo [40] analytical approximation for the internal inductance and resistance of round wires given in Equation (40) and Equation (41), respectively, is frequency-dependent. Therefore, a direct comparison of the COMSOL predictions and the analytical approximations for these quantities across frequency can be utilized for cross-validation purposes.

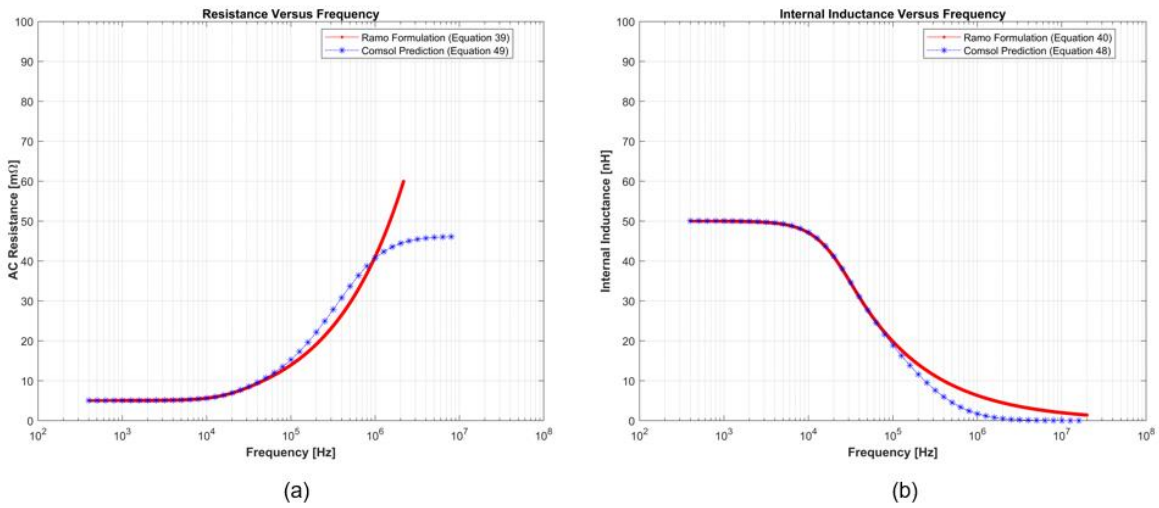

Figure 31: (a) Ramo Formulation and COMSOL prediction for Internal Resistance, (b) Ramo Formulation and COMSOL prediction for Internal Inductance

Figure 31(a) and Figure 31(b) provide a direct comparison between the Ramo analytical approximation and the COMSOL prediction for resistance and internal inductance of Geometry 1, respectively. It is noted that the COMSOL prediction for internal inductance and resistance demonstrates excellent agreement with the associated analytical approximations up to approximately 100 kHz. At higher frequencies, there is an observed difference between the COMSOL prediction and the analytical approximation for resistance. This is likely due to the size of the mesh employed in the COMSOL model. At high frequency, very small mesh size is required to predict the continual increase in resistance that results from the decreasing skin-depth. However, the use of very small mesh elements leads to convergence challenges with FEA solvers. Thus, COMSOL is expected to under-predict the high-frequency AC resistance of conductors when practical mesh sizes are employed. The accuracy of the COMSOL predictions for AC resistance at higher frequency may be improved by employing smaller mesh elements at the expense of computation time.

The frequency range for which it is permissible to use the low-frequency and high-frequency approximations from Chapter 3 can be linked to the ratio r_0/δ, where r_0 represents the cross-section radius of the wire, and δ represents the skin depth. For $r_0/\delta \leq 7.55$, the low-frequency approximation of Equation (30) and Equation (31) can be used depending on the required impedance quantity [40]. Similarly, for $r_0/\delta \geq 7.55$, the high-frequency approximation of Equation (33) can be used [40]. Table 8 provides a mapping of the r_0/δ ratio to frequency and identifies the most suitable impedance approximation equations as a function of frequency for a wire cross-sectional radius of $1.026\ mm$ and copper conductivity of $5.998 \times 10^7 [S/m]$.

TABLE 8
PERMISSIBLE APPROXIMATION METHOD

Frequency [Hz]	**Skin-depth (δ) [m]**	**$\frac{r_0}{\delta}$ Ratio**	**Approximation Method**	**Equation Number**
1e2	0.0065	0.1579	Low-Frequency	(30), (31)
1e3	0.0021	0.4993	Low-Frequency	(30), (31)
1e4	0.00065	1.5788	Low-Frequency	(30), (31)
1e5	0.00021	4.9926	Low-Frequency	(30), (31)
1e6	0.000065	15.7880	High-Frequency	(33)
1e7	0.000021	49.9260	High-Frequency	(33)

Recall that total self-inductance includes the contribution of both the internal and external inductance for a given geometry. It has been shown in the literature that skin effect has no influence on the external inductance, but strongly influences the internal inductance [40]. If the radius of the conductor cross-section is small compared to the wire loop radius, the field around the conductor is nearly the same as though the current were concentrated along the center of the wire [40]. By implication, the magnetic fields around the conductor are not expected to change with frequency in spite of the changing current distribution within the conductor caused by skin effect. This assumes that proximity effect is negligible for the conductor in question, as it is in the case of a round loop with no nearby current-carrying conductors. Figure 32 demonstrates the magnetic flux density around Geometry 1 at two different frequencies. Magnetic flux density is related to the magnetic field intensity by the isotropic permeability of the conductor, which in this case is the permeability of free space. Therefore, the magnetic field intensity around the

conductor will also behave identical to that demonstrated in Figure 32. Therefore, either of these two quantities can be used to show the field distribution around the conductor.

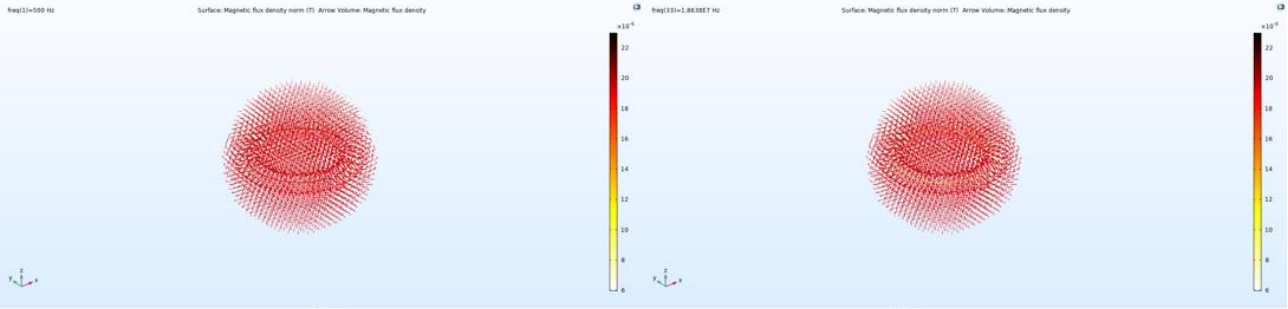

Figure 32: (a) Magnetic Flux Density norm @ 500 Hz, (b) Magnetic Flux Density norm @ 18 MHz

The magnetic flux surrounding the conductor within the Geometry 1 COMSOL model appears to be identical at 500 Hz (Figure 32(a)) and at 18 MHz (Figure 32(b)). However, this visual comparison, while indicative, is not quantitative. Therefore, a volume integration of the B-field inside and outside the conductor at each frequency point was performed in COMSOL. This analysis provides further insight into the difference between internal and external inductance because internal inductance depends only on the fields inside the conductor, while external inductance depends only on the fields outside the conductor. The result of this computation is shown in a normalized fashion in Figure 33.

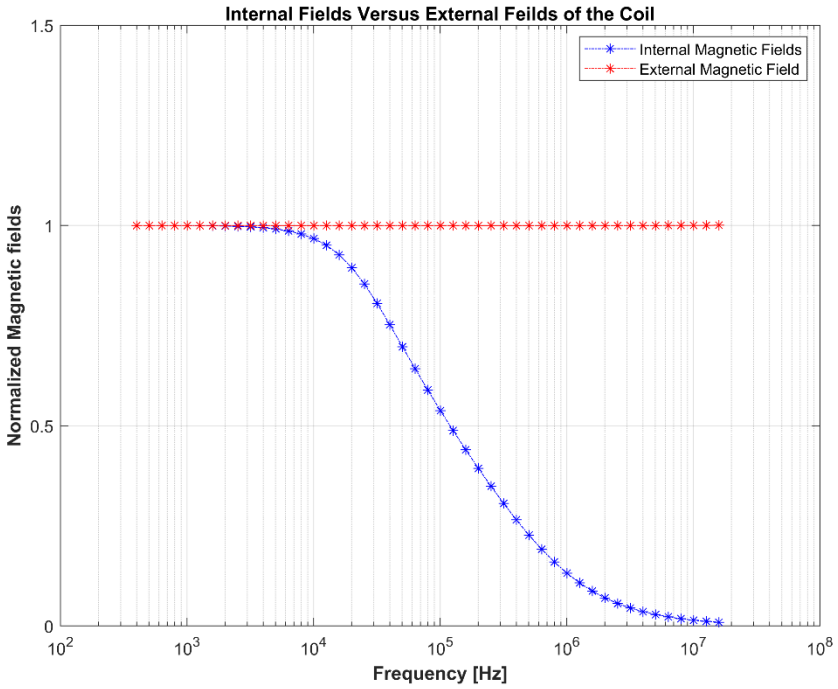

Figure 33: Normalized Internal and External magnetic fields around Geometry 1

Figure 33 demonstrates that the external magnetic fields computed by COMSOL for Geometry 1 do not change across frequency, while the internal fields change drastically across frequency. This implies that the external inductance is frequency independent, while the internal inductance is frequency dependent. Recall that the total self-inductance of a conductive structure is given in Equation (11) as:

$$L_{loop} = L_{internal} + L_{external} \tag{55}$$

Therefore, to calculate the fixed, external inductance of a given conductor, the internal inductance should be subtracted from the total self-inductance. Furthermore, it can be inferred from the analysis of this section that the contribution of the internal inductance is negligible at high frequency. Thus, the total self-inductance at high frequency can be used to estimate the frequency-independent contribution of external inductance. The result of applying this process to the COMSOL-predicted inductance values for Geometry 1 is displayed in Figure 34.

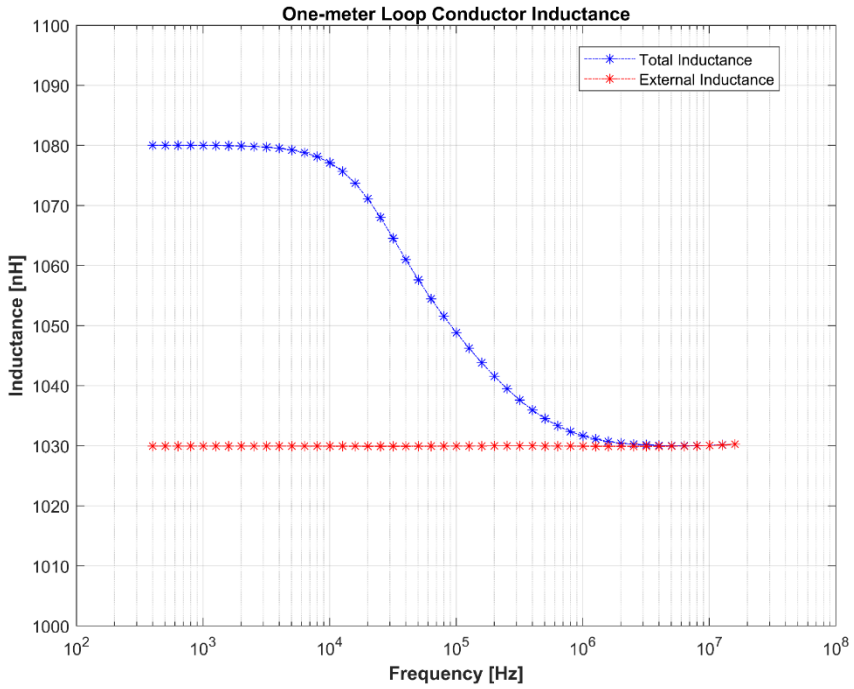

Figure 34: Total and External Inductance of Geometry 1

As shown in Figure 34, the external inductance of Geometry 1 assumes a single value of 1030 nH across frequency. The reduction in total inductance from 1080 nH (low-frequency) to 1030 nH (high-frequency) is completely explained by the drop in internal inductance due to the changed in skin-depth penetration. This analysis confirms that skin effect is solely responsible for the frequency-dependence of an isolated conductor. As will be shown in the following chapter, this finding represents a special case that is only applicable when the influence of proximity effect is negligible. The same analysis were performed on Geometry 2 to Geometry 5, and the results of the process are provided in Chapter 5 of this thesis.

4.3.2. Proximity Effect Demonstration

Proximity effect occurs whenever a conductor carrying current is in the presence of a second nearby conductor, which is also carrying current. The presence of the second nearby conductor can increase or decrease the current in the first conductor, which in turn decreases or increases the inductance, respectively. To illustrate proximity effect in COMSOL, a simplified test case consisting of a one-meter straight conductor was used (Geometry 6). This test case was selected because its simplicity facilitates the studies described in this section, and because it has been previously established that the internal inductance of a one-meter conductor is approximately $50\ nH$.

When performing electromagnetic studies in COMSOL, a good design practice is to ensure that the air-domain around the conductor maintains a similar profile to that of the conductor. This improves simulation accuracy and aids in avoiding convergence issues. Therefore, a cylindrical air domain was employed for the evaluation of Geometry 6. Both the cylindrical air domain and the conductive structure of Geometry 6 were projected in the x-direction as shown in Figure 35.

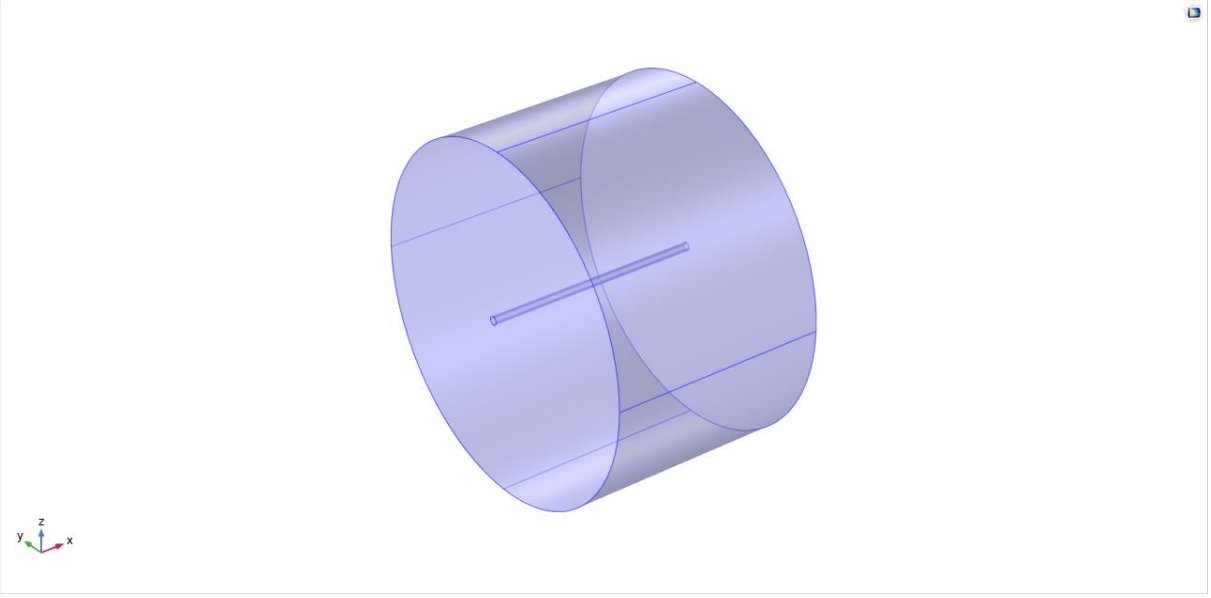

Figure 35: Straight one-meter conductor (Geometry 6)

Because inductance is solely defined for a closed loop, a return circuit must be specified in COMSOL, even when the test case is a straight conductor. The cylindrical air-domain in this simulation serves as the return path. As a consequence, the inductance of a straight conductor is very sensitive to the size of the air domain when evaluated in COMSOL. Adequate care must be taken in choosing an air domain size that accurately predicts the behavior of physical conductors. One approach for ensuring accuracy is to evaluate very long conductor geometries. This approach represents the configuration of a circular loop with an infinitely large radius. Another approach is to calibrate the size of the air domain using an analytical approximation as a reference. An air-domain of radius 80 *cm* projected in the x-axis direction was used for this study. The size of the air-domain was adjusted until a close agreement between COMSOL prediction and an analytical approximation from Grover [112] was achieved at DC for this test case. The particular Grover expression used for this purpose is given as:

$$L = 2l\left(\left(\ln\left(\frac{2l}{d}\right)\left(1+\sqrt{1+\left(\frac{d}{2l}\right)^2}\right)\right)-\sqrt{1+\left(\frac{d}{2l}\right)^2}+\frac{\mu}{4}+\left(\frac{d}{2l}\right)\right) \quad (56)$$

where L represents the inductance in nH, l represents the length of the conductor in *cm*, and d represents the cross-section diameter of the conductor in *cm*.

The same coil study procedure used previously for Geometry 1 was used again for the Geometry 6 test case. The results presented in Table 9 demonstrate that both the internal and total inductance predicted by COMSOL for Geometry 6 match closely the analytical prediction provided by Equation (56).

TABLE 9
ANALYTICAL & COMSOL PREDICTION

	Analytical DC Inductance Prediction [nH]	COMSOL DC Inductance Prediction [nH]	Analytical DC Internal Inductance Prediction [nH]	COMSOL DC Internal Inductance Prediction [nH]
(One-meter straight Conductor)	775	778	50	50

As part of this study, the magnetic field lines around Geometry 6 were studied as a function of frequency. This analysis revealed that the fields around the Geometry 6 conductor do not change with frequency. This is the same trend observed with the Geometry 1 circular loop. The B-field

distribution around Geometry 6 is shown Figure *36*, from low-frequency (500 Hz) to high-frequency (18 MHz).

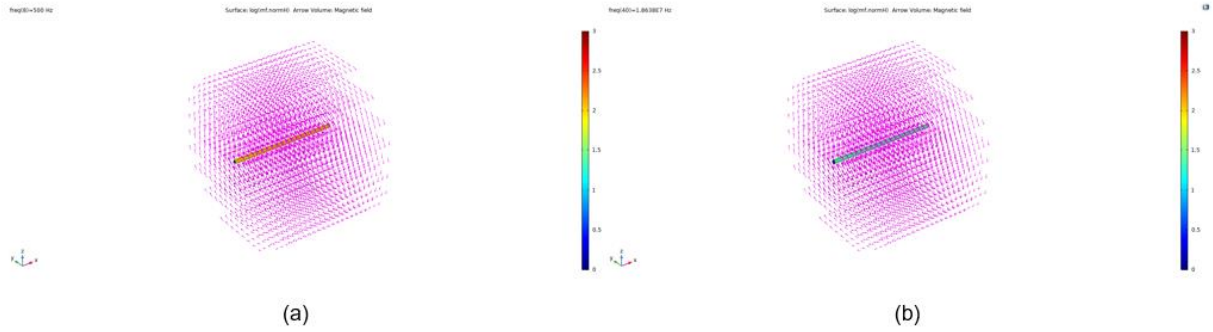

Figure 36*: (a) Magnetic Field Intensity @ 500 Hz, (b) Magnetic Field Intensity @ 18 MHz*

In order to provide a quantitative assessment of the magnetic field for Geometry 6, a volume integration was applied to the B-field both inside and outside the conductor at each frequency point. The results of this evaluation are presented in Figure 77 of Appendix A.5. These results demonstrate that the internal and external field distributions for Geometry 6 exhibit the same trends previously described for Geometry 1. This is because skin effect is the dominant dynamic effect in the single-conductor case represented by Geometry 6.

In order to leverage the results obtained for Geometry 6 to evaluate the influence of proximity effect, a second, identical conductor was added to the model to create Geometry 7. In Geometry 7, the two conductors are positioned $5cm$ apart. The current was specified in such a way that the current direction is opposing in each conductor, as shown in Figure 37.

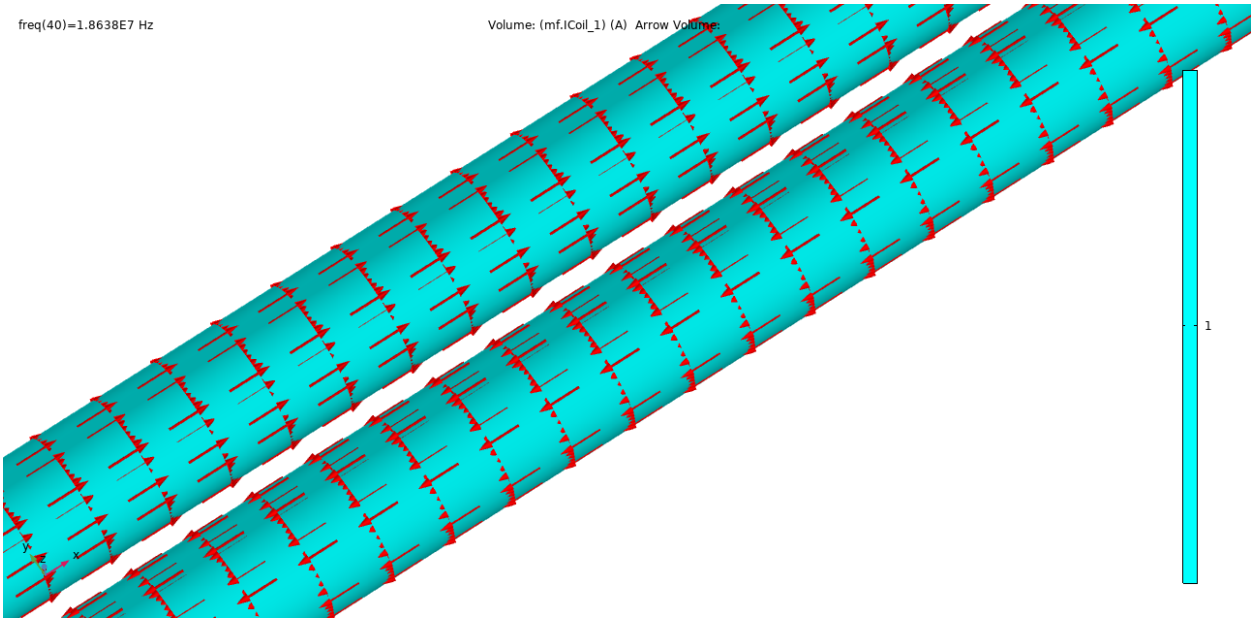

Figure 37: Current Direction in Geometry 7

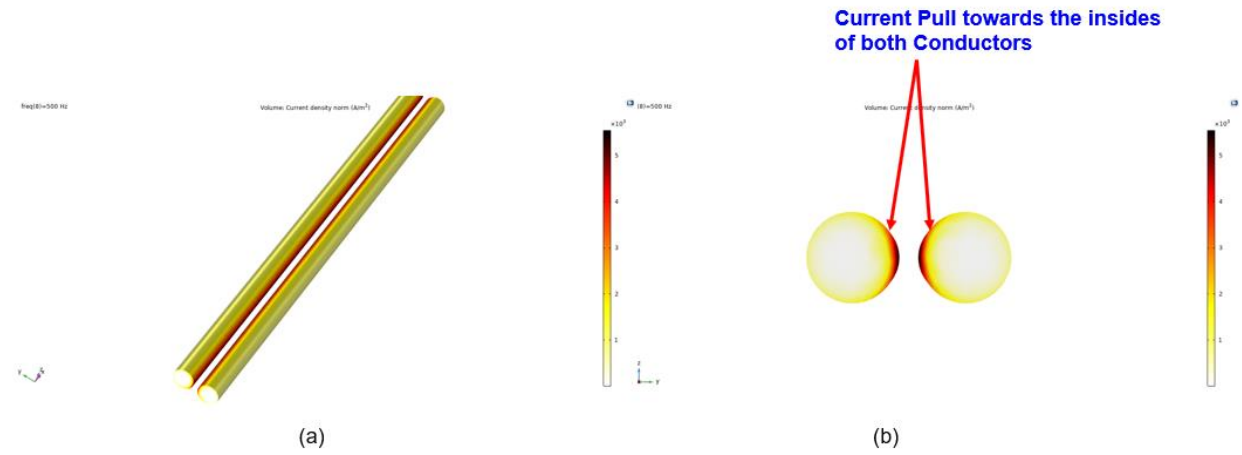

Figure 38: (a) Current Density @ 500 Hz in x-y-z direction, (b) Current Density @ 500 Hz in z-y direction

Figure 38 provides a set of current density plots for Geometry 7 when evaluated in COMSOL at a stimulus frequency of 500 Hz. The influence of both skin and proximity effect are clearly visible in this figure, and especially in Figure 38(b). Skin effect causes the concentration of

current at the outside of each conductor as indicated by yellow, and the absence of current at the center of each conductor as indicated by white. In addition, the red region of Figure 38(b) indicates that most of the current concentrates on the side of each conductor that is closest to the neighboring conductor. Application of the right-hand rule to this geometry reveals that the fields on the outside of the pair of conductors will combine destructively, while the fields between the pair of conductors will combine constructively. The destructive combination of the "outer" flux leads to flux cancellation; while the constructive combination of the "inner" flux leads to high current concentration of current in this region. Due to the influence of proximity effect, the behavior of the B-field is frequency dependent for Geometry 7. The observed change in field distribution around Geometry 7 is shown in Figure 39. This figure demonstrates that the B-field outside the pair of conductors is significantly reduced at high frequency (18 MHz) compared to low frequency (500 Hz).

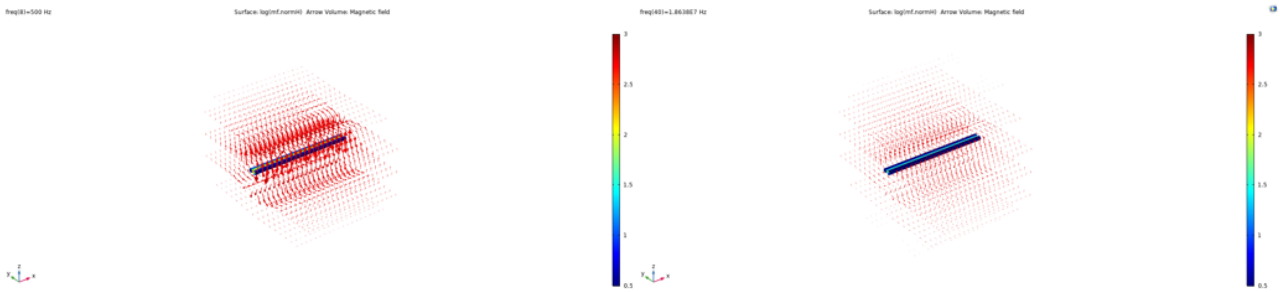

Figure 39: (a) Magnetic Field Intensity for Geometry 7 @ 500 Hz , (b) Magnetic Field Intensity for Geometry 7 @ 18 MHz

To investigate the impact of conductor spacing on proximity effect, two additional test cases were evaluated in COMSOL. The normalized external magnetic field distributions for each of these test cases are plotted as a function of frequency in Figure 40.

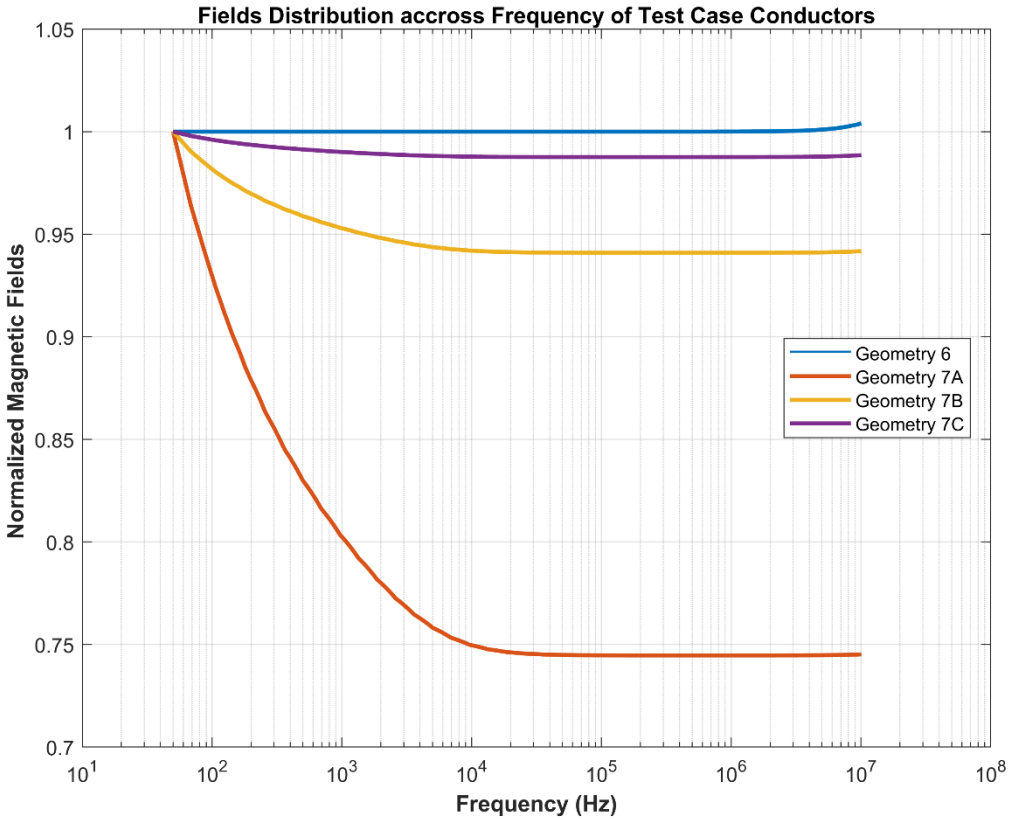

Figure 40: Normalized field distribution demonstrating proximity effect

Figure 40 demonstrates that the separation distance of the conductors plays an important role in determining the frequency dependence of the magnetic field. When this distance is reduced, both the constructive and destructive combination of field lines is intensified, which leads to increased flux cancellation for opposing current carrying conductors. This leads to an even greater drop in inductance at high frequency compared to the inductance reduction resulting from skin effect alone in the single-conductor case. This analysis suggests that inductance is

particularly reduced when conductors carrying current in opposite directions are separated by a very small distance. This is the basis for the inductance reduction technique leveraging flux cancellation that is described in literature [120]–[122]. This inductance reduction technique is also employed in the design of high-performance conductive systems within MCPMs and busbars.

A summary of the estimated inductance values for each of the test cases considered in this section is provided in Table 10. The results shown in Table 10 corroborate the claim that small conductor spacing leads to more significant inductance reduction due to flux cancellation.

TABLE 10
EXTRACTED INDUCTANCE USING COMSOL FOR TEST CASES AT DC

	15cm spacing	**8cm spacing**	**5cm spacing**
Inductance [nH]	219.69	155.71	103.59

4.4. COMSOL Analysis and Impedance Extraction of a Rectangular Loop

This section extends the analysis in the previous section by demonstrating the influence of the skin effect and the proximity effect in rectangular loop conductors. The rectangular loop conductors studied in this section are similar to the conductors found in MCPMs and converter systems. This study presents a clear demonstration of the influence of proximity effect in these types of rectangular conductors. Several simple test cases (Geometry 8 to Geometry 14 in Table 5) are used to illustrate the concepts in this section. These specific geometries were selected to represent the physical samples used in the empirical studies presented in Chapter 5. In each test case, the return circuit was made as close as possible to the forward path to emphasize the influence of the proximity effect. This arrangement also ensures a large drop in inductance at high frequency due to flux cancellation.

For all geometries considered in this section, the thickness of the conductor was specified to be $6.85\ mils$. This value corresponds to the thickness of a $5\ oz$ copper layer on a printed circuit board (PCB). $5\ oz$ copper was used for fabrication of the PCBs employed in the experimental studies of Chapter 5. Figure 41 shows one example rectangular loop geometry designed in COMSOL Multiphysics in support of this study.

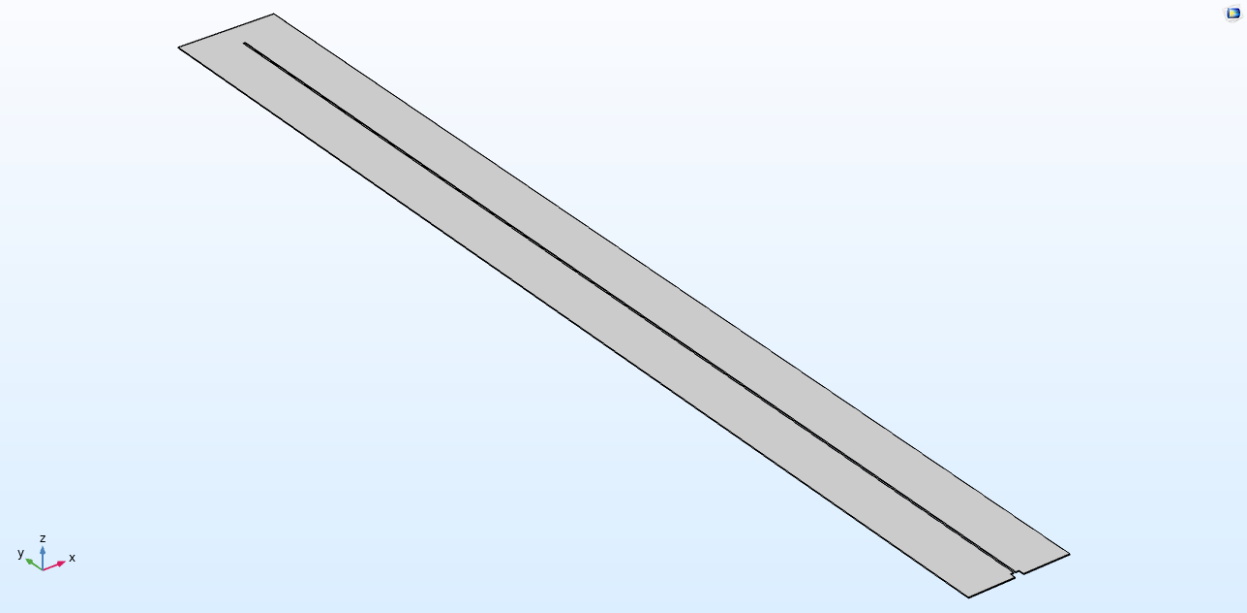

Figure 41: Example Rectangular Test Loop implemented in COMSOL

Recall that to avoid convergence issues and ensure simulation accuracy in COMSOL, it is recommended to use a similar profile between the air-domain and the device under study in COMSOL. Accordingly, the studies in this section employ a rectangular infinite-element domain (IED), which closely resembles the profile of the conductor geometries employed in these studies. This geometry is shown in the mesh rendering of Figure 42.

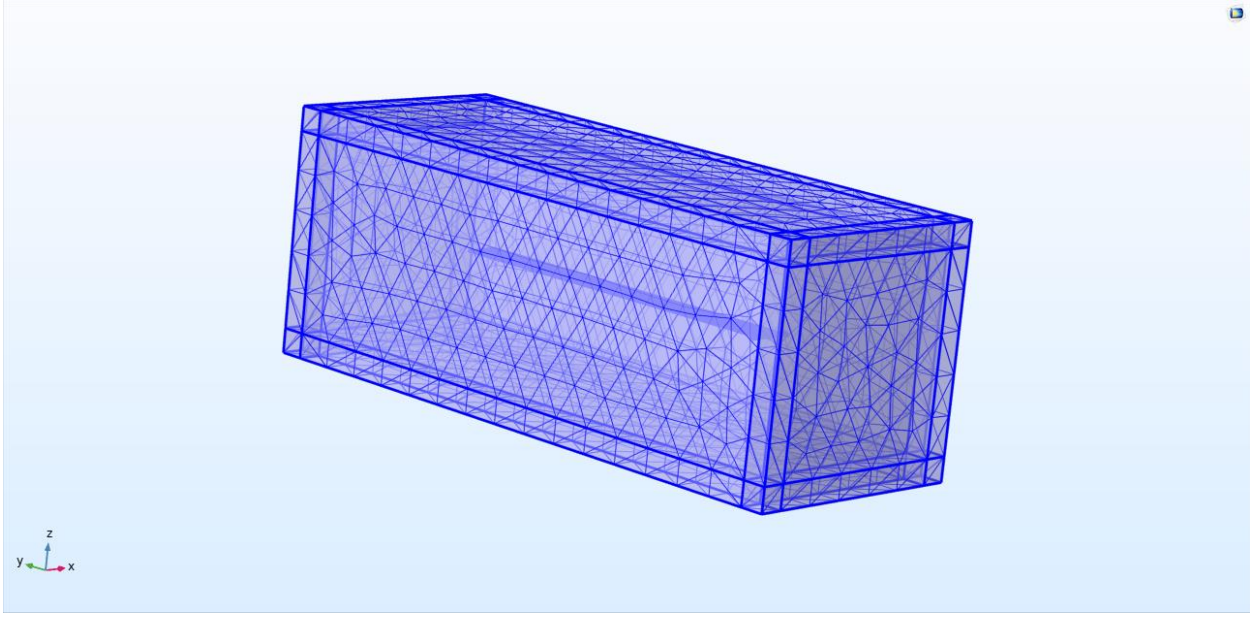

Figure 42: Mesh Rendering of the entire domain

The frequency-domain studies described in this section utilize a log-spaced frequency sweep from 500 Hz to 20 MHz with seven steps per decade. All other study settings are similar to those specified for the Geometry 1 study described previously in this chapter. An example current density plot, which was computed for the Geometry 8 test case, is shown at two different frequencies in Figure 43. The influence of proximity effect is evident in Figure 43(b), which illustrates the current density of Geometry 8 at high frequency (18 MHz).

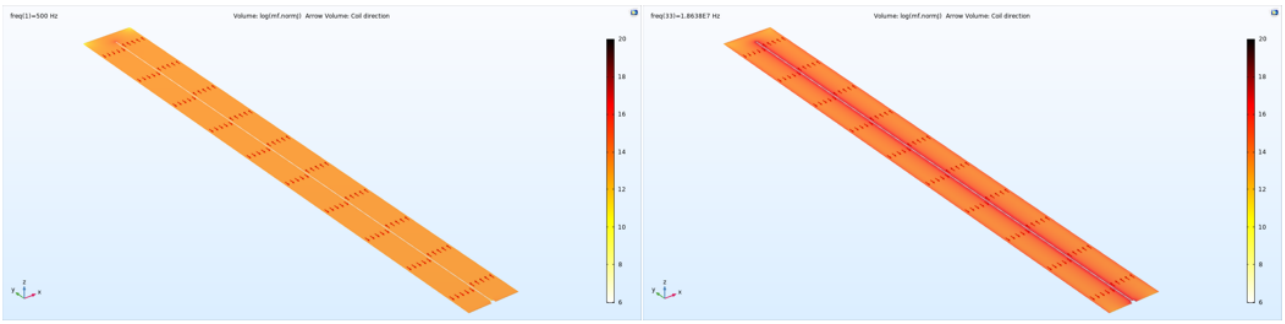

(a) (b)

Figure 43: (a) Current density for Geometry 8 @ 500 Hz, (b) Current density for Geometry 8 @ 18 MHz

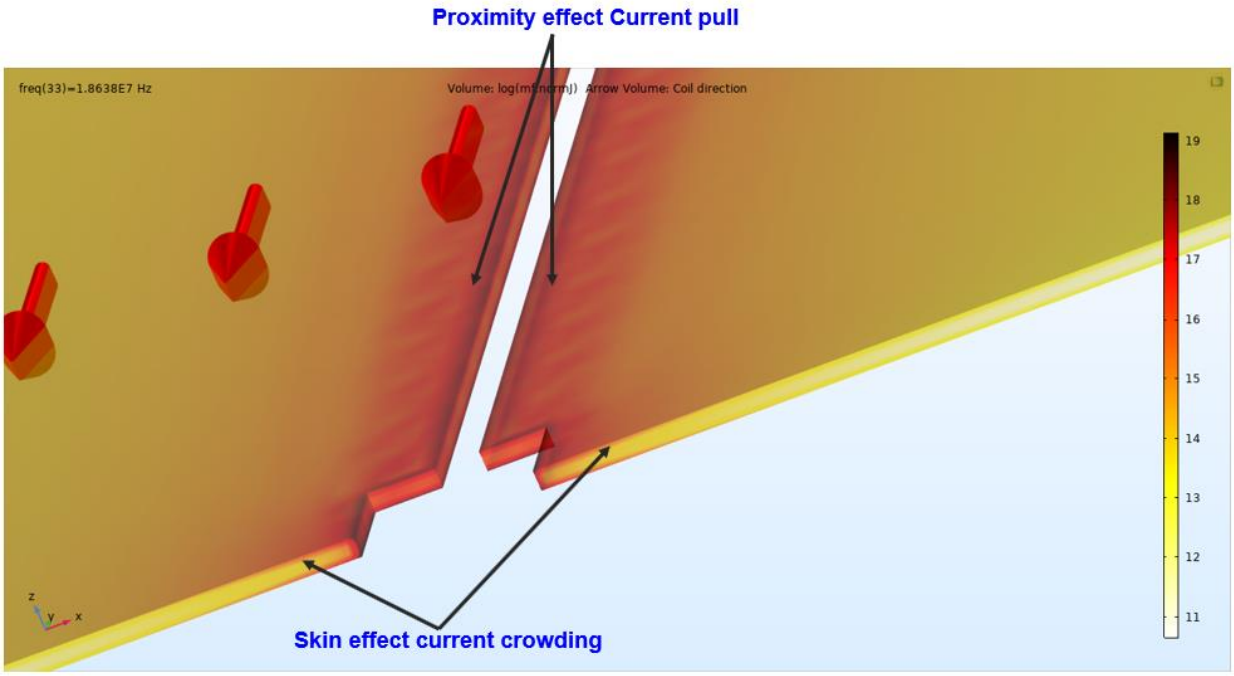

Figure 44: Current density plot for Geometry 8 at high-frequency (18 MHz)

For the circular loop geometries, it was shown that the skin effect is solely responsible for the frequency-dependence of the conductor impedance. However, for the rectangular-loop geometries, both the skin effect and the proximity effect affect the impedance. This is illustrated in the zoomed-in, high-frequency current density plot shown in Figure 44. For this specific case, the influence of proximity effect is much more pronounced than the influence of skin effect. As shown in Figure 44, proximity effect causes the concentration of current at the inner portion of the conductor as indicated by the red region. Most of the current concentrates on the side that is closest to the return path conductor. The skin effect also causes the concentration of current at the surface of the conductor as indicated by the tiny red region, and the absence of current at the center of the conductor is indicated by yellow.

The assumptions for approximating the resistance and internal inductance of conductors under the influence of skin effect do not apply for the case of rectangular-loop geometries [40].

This is due to the influence of proximity effect. For such structures, the current in the return path conductor will produce nearly as much effect upon current distribution as the current in the forward path conductor. In addition, the external inductance also depends on frequency in this case. This is because the external magnetic field is affected when the internal current loses its symmetrical distribution with respect to the wire axis [40]. Presently, there is no known analytical model that separates the self-inductance of a rectangular loop into internal and external components. Therefore, separating inductance into internal and external components might be difficult for this type of coil.

The observed change in magnetic field distribution around Geometry 8 is shown in Figure 45. Figure 45(a) and Figure 45(b) presents the B-field distribution of Geometry 8 at 500 Hz and at 18 MHz, respectively. This figure demonstrates that the magnetic field surrounding the rectangular loop geometry is reduced at high frequency due to proximity effect and the resulting flux cancellation.

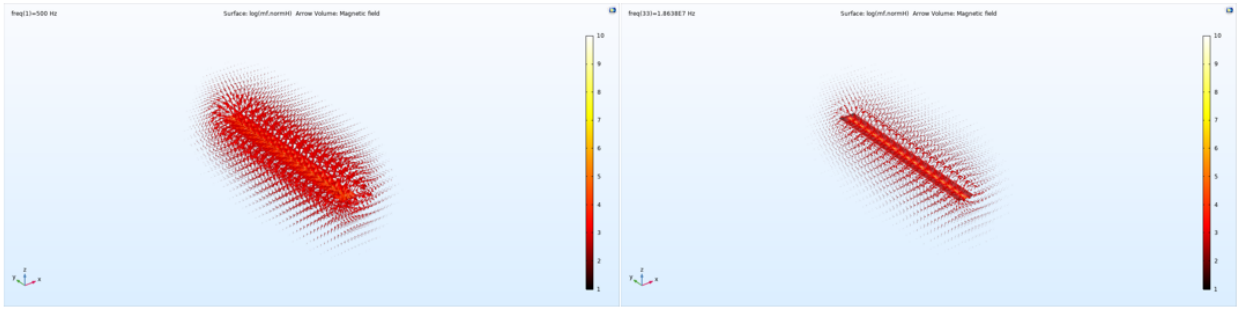

(a) (b)

Figure 45: (a) Rectangular Magnetic Field @ 500 Hz, (b) Rectangular Magnetic Field @ 18 MHz

Figure 46 shows the results of applying a volume integration of the external magnetic fields at each frequency point for the Geometry 1 and the Geometry 8 test cases. As shown in this figure, the field distribution around the Geometry 1 conductor does not change across

frequency due to the absence of proximity effect. In the case of the Geometry 8 conductor, the field distribution around the conductor changes across frequency. At high-frequency, the total integrated field value decreases to about half the value at low-frequency due to proximity effect and the resulting flux cancellation.

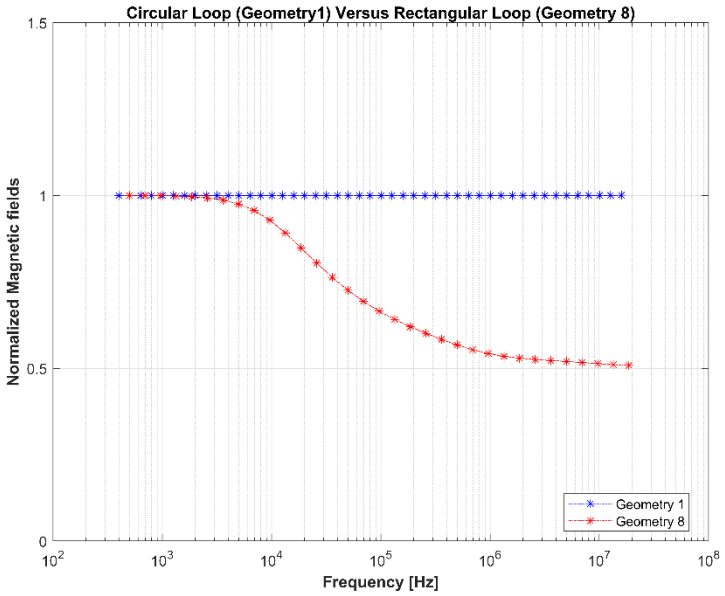

Figure 46: Magnetic Field intensity of Geometry 1 (without proximity effect) versus Magnetic field intensity of Geometry 8 (with proximity effect)

4.4.1. Rectangular Loop Dimension Variation

The goal of this section is to evaluate the impact of varying the dimensional parameters of the rectangular loop geometry studied in this chapter. The parameters to be varied are the loop length (l) and the loop width (w) as defined in Figure 17. It is believed that understanding the influence of these parameters may prove useful in the design of busbars and other similar current carrying conductors in power electronic converters.

The effect of varying the conductor length (l) within the rectangular loop geometry is illustrated in Figure 47. When the length of the conductor is reduced, the low-frequency inductance is nearly unchanged, but the inductance drop moves to higher frequency and becomes less significant. In other words, the greater the length of the rectangular loop, the greater the inductance drop. This result agrees with intuition because the inductance is directly proportional to the effective cross-sectional area. Therefore, as the cross-sectional area is decreased, the inductance drop also reduces.

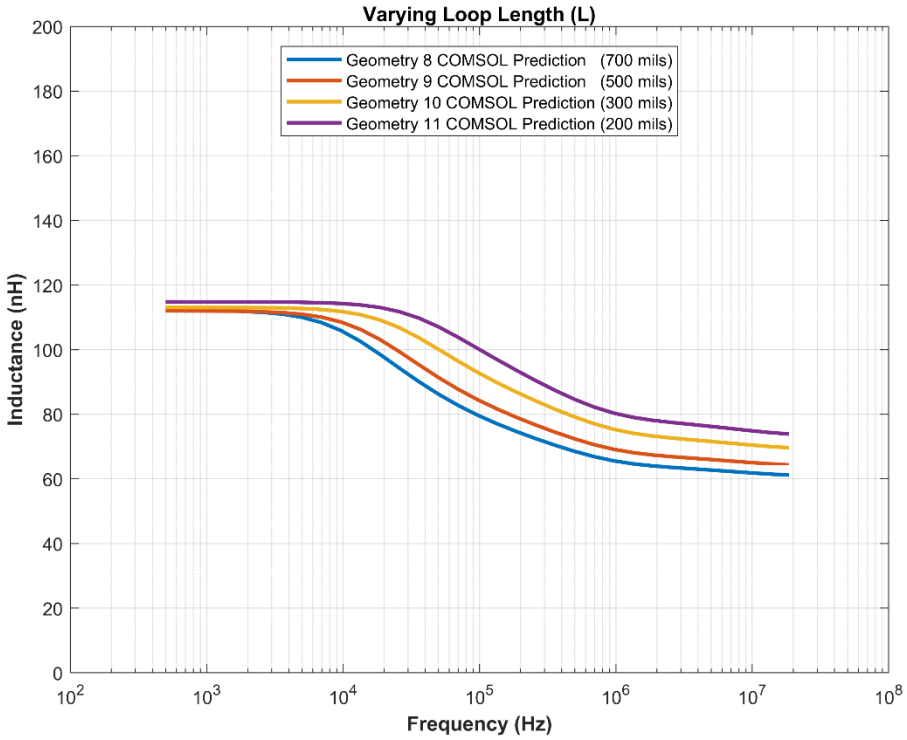

Figure 47: Effect of varying loop length

The effect of varying the conductor width (w) within the rectangular loop geometry is illustrated in Figure 48. As shown in this figure, the total inductance is directly proportional to the rectangular geometry conductor width (w). The reduction in inductance at high frequency appears to be fairly insensitive to the conductor width parameter. This agrees with intuition because the effective cross-sectional area is unchanged, therefore, the inductance drop also remains unchanged. But the as the effective loop area is decreased, the low frequency inductance also decreases as shown in Figure 48.

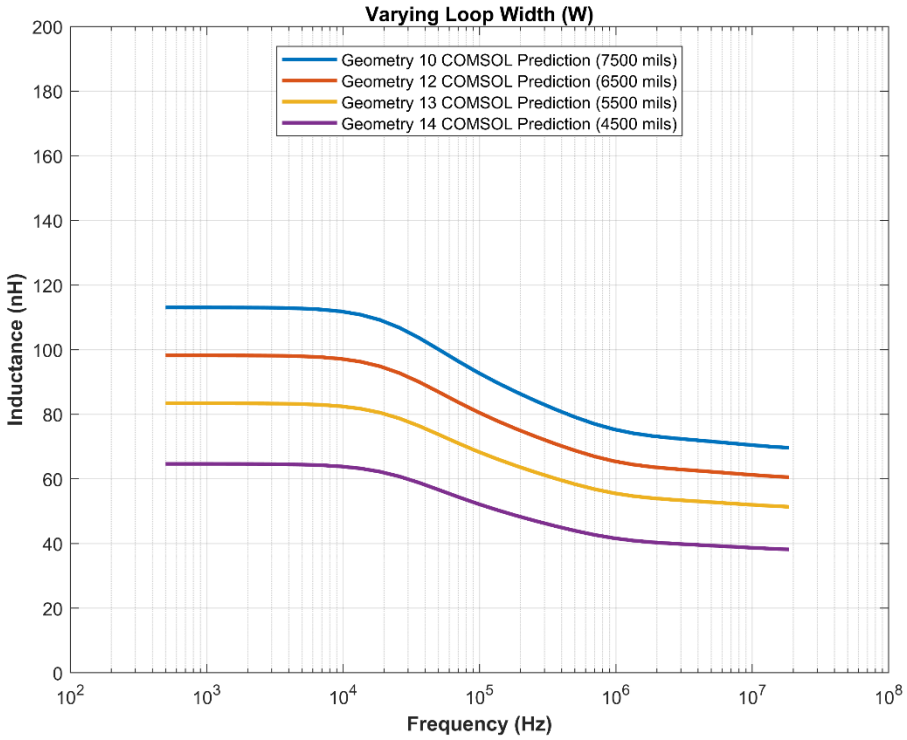

Figure 48: Effect of varying loop width

4.5. Summary of FEA Analysis

This chapter presents a COMSOL-based simulation study of the impedance characteristics of several different conductor geometries. The impedance predictions from these simulation studies are compared against the analytical predictions of Chapter 3. These comparisons reveal good agreement between both impedance estimation methods. A thorough analysis of the skin effect and the proximity effect is also included in this chapter. The skin effect is found to be solely responsible for the frequency-dependence of conductor impedance when the conductor is isolated from other current-carrying conductors. When the conductor is near other current-carrying conductors, the proximity effect also influences the conductor impedance, particularly at high frequency. When conductor geometry is influenced only by skin effect, the total inductance can be cleanly separated into internal and external inductance components. The former is affected by fields inside the conductor, while the latter is affected by fields external to the conductor. When conductor geometry is influenced by proximity effect, a clean separation between internal and external inductance is not possible. It is also shown that proximity effect causes inductance to decrease significantly at high-frequency for closely-spaced conductors carrying current in opposite directions. This is due to a reduction in external fields at high frequency due to flux cancellation. On the other hand, for geometries influenced by skin effect alone, the external magnetic field does not change with frequency. This implies that skin effect can only influence the internal inductance, which helps to explain why modest reductions in inductance are typically observed for geometries that are not influenced by proximity effect.

CHAPTER 5:

EMPIRICAL EVALUATION & VALIDATION OF PARASITICS OF CONDUCTORS

The goal of this chapter is to validate the COMSOL impedance models from Chapter 4 as well as to validate some of the analytical models from Chapter 3 to the extent possible. Empirical validation of the results extracted from FEA analysis using COMSOL is an important step in the conductor impedance estimation process. Due to its simplicity, accuracy, and ease of use, the impedance analyzer (ZA) will be used for this process. One major advantage of the ZA is that impedances can be obtained directly from raw data measurements from this instrument. The ZA also offers the advantage of sweeping across a wide range of frequencies per measurement as compared to the LCR meter, which measures impedances at one frequency per measurement.

Presently, there are very few ZA instruments capable of accurately measuring single-digit nano-Henry-scale inductances between 10 and 100 MHz. For example, Keysight's E4990a, which is one of the most accurate impedance analyzers on the market, can measure inductances as small as 1 nH within a 5% accuracy range [17]. The E4990a impedance analyzer is capable of measuring impedances between 20 Hz and 120 MHz [92]. This instrument, which is used for performing empirical measurements of the test case conductor geometries in this thesis, is shown in Figure 49.

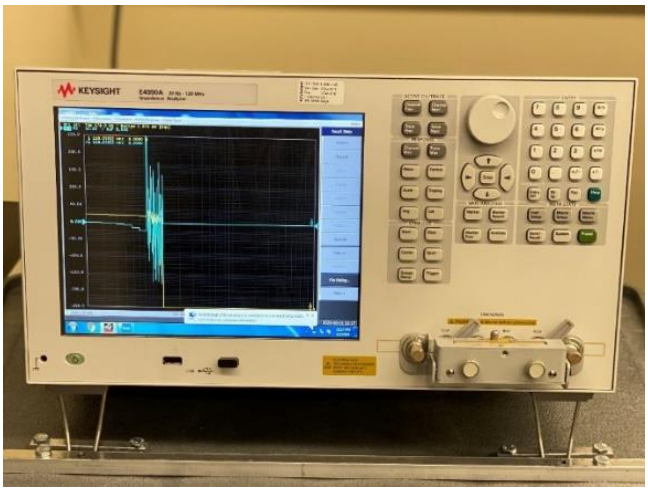

Figure 49: Keysight E4990a impedance analyzer with test fixture attached to RF connectors

A test fixture, which is also manufactured by Keysight technologies (Keysight 16047E), is used in conjunction with the ZA to enable measurement of the DUTs considered in this thesis. The Keysight 16047E commercial fixture is designed to measure impedances of leaded components with high accuracy over the entire frequency range of the impedance analyzer [123]. The DUTs considered in this work are designed in such a way that they fit between the leads of the Keysight 16047E test fixture. A close-up image of the 16047E test fixture is shown in Figure 50.

Figure 50: Keysight 16047E test fixture

5.1. Fixture Compensation

Before measurement of the DUT is performed, it is necessary to compensate the test fixture. Compensation is necessary in order to remove the fixture contribution from the impedance measurement results. The accuracy of the measurement can be substantially improved by the compensation process. The compensation process generally requires the measurement of three reference or “standard” impedances: OPEN, SHORT, and LOAD. However, when manufacturer-provided commercial test fixtures are used for DUT measurement, the LOAD standard can be omitted [123]. Therefore, because the 16047E test fixture is used, there is no need to perform LOAD compensation for the measurements presented herein [123]. Typically, compensation of the test fixture is performed by utilizing the internal capabilities of the ZA. Using this “internal” compensation process, the OPEN, SHORT and LOAD measurements are performed, and the results are recorded inside the ZA. The ZA then uses mathematical compensation equations to remove the impact of the test fixture when the DUT is measured. The required equations used for fixture compensation are given in Table 11, which is adapted from [67].

TABLE 11
FIXTURE COMPENSATION EQUATIONS

Compensation Type	Equation	
Short	$Z_L = (Z_{XM} - Z_{SC})$	(57)
Open	$Z_L = \frac{Z_{OC} Z_{XM}}{(Z_{OC} - Z_{XM})}$	(58)
Load	$Z_L = \frac{Z_{ST} Z_{XM}}{Z_{SM}}$	(59)
Open and Short	$Z_L = \frac{Z_{OC}(Z_{XM} - Z_{SC})}{(Z_{OC} - Z_{XM})}$	(60)
Open and Load	$Z_L = \frac{Z_{ST} Z_{XM}(Z_{OC} - Z_{ST})}{(Z_{OC} - Z_{XM}).* Z_{ST}}$	(61)
Short and Load	$Z_L = \frac{Z_{ST}(Z_{XM} - Z_{SC})}{(Z_{SM} - Z_{SC})}$	(62)
Open, Short and Load	$Z_L = \frac{(Z_{XM} - Z_{SC})(Z_{OC} - Z_{SM})}{(Z_{OC} - Z_{XM})(Z_{SM} - Z_{SC})} Z_{ST}$	(63)

Z_{XM} Measured DUT Impedance

Z_{OC} Measured Open calibration standard Impedance

Z_{SC} Measured Short calibration standard Impedance

Z_{SM} Measured Load calibration standard Impedance

Z_{ST} True Impedance of Load calibration standard

5.2. External Fixture Compensation

External fixture compensation is an alternative to the ZA's internal compensation process. By external compensation, the standard compensation measurements are performed by

the user and recorded in an external file. Subsequently, DUT measurements are performed without utilizing the internal instrument compensation process, and these uncompensated DUT measurements are stored separately. Finally, the mathematical compensation equations of Table 11 are applied in a post-processing step via MATLAB to remove the fixture influence. It is shown in [67] that using the external compensation technique is superior to the internal compensation method. One advantage of the external compensation process is that repeated measurements for each standard and the DUT can be stored and inspected separately during the post-processing stage. This enables outliers in the measurements to be removed prior to averaging the remaining valid results. For low-impedance conductor measurements, the external compensation technique leads to significant improvements in impedance accuracy, especially at low-frequency. For this thesis, the external compensation process was utilized with a set of 25 measurements per standard and 600 data points per measurement. To perform the OPEN standard measurement, the lead plates of the 16047E are closed with no DUT in place, as shown in Figure 51.

Figure 51: Open compensation measurement

For the SHORT compensation measurement, a manufacturer-supplied copper shorting bar is placed between the lead plates, as shown in Figure 52.

Figure 52: Short compensation measurement

Figure 53 shows the result of applying the internal and external compensation techniques to the same DUT inductance measurement. For this setup, repeated measurements were performed of the SHORT compensation standard, the OPEN compensation standard, and the DUT. Twenty-five individual measurements were made of each type and subsequently post-processed using the procedure outlined in [67]. As the plot of Figure 53 demonstrates, the low-frequency uncertainty in the DUT inductance measurement is significantly reduced as a result of applying the external compensation process as compared to the internal compensation technique.

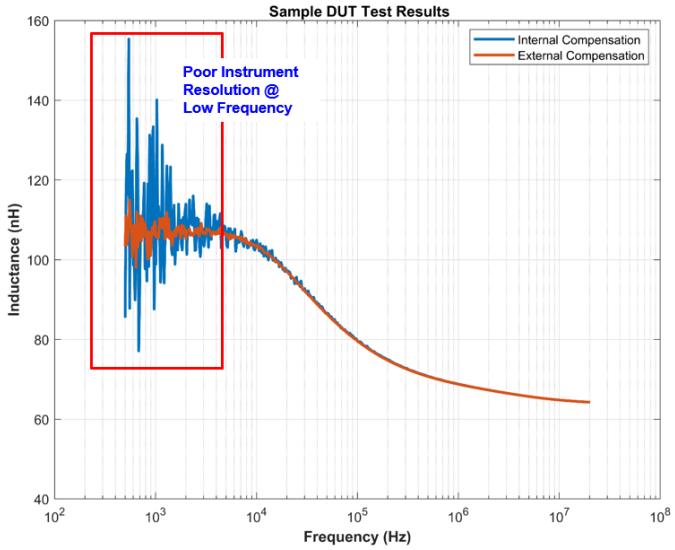

Figure 53: Comparing Internal and External compensation techniques

5.3. Empirical Measurement of Devices Under Test

This section presents the empirical measurements of the test conductor geometries considered by this thesis. Specifically, the different geometries treated in the simulation study of Chapter 4 were measured to validate the FEA predictions presented previously. Since this thesis focuses on circular and rectangular test conductor geometries particularly, four circular loops and seven rectangular loops were fabricated and measured. The diameter of each circular loop was selected using the analytical approximation of Equation (48) to achieve specific target inductance values. The target inductance values selected are: 300 nH (Geometry 2), 250 nH (Geometry 3), 200 nH (Geometry 4), and 150 nH (Geometry 5). Figure 54 shows the measurement setup utilized for evaluation of the Geometry 3 test case. For additional test setup details, refer to Appendix A.6.

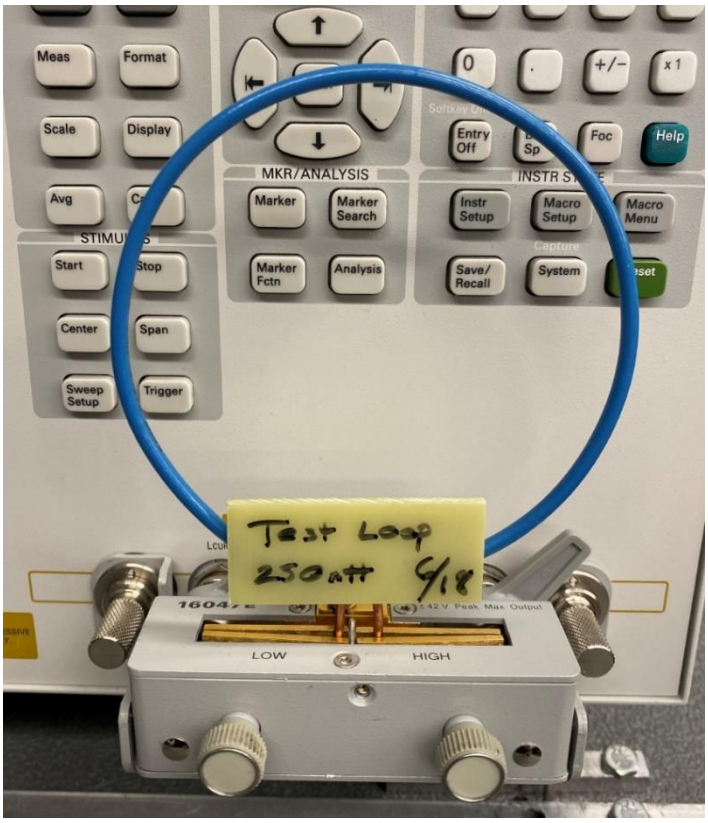

Figure 54: Empirical setup of Geometry 3 conductor

The rectangular test loop geometries were implemented via custom PCBs. Each geometry was designed using PCB design software and the generated Gerber files were sent to a PCB company for manufacturing. In the case of the rectangular loop geometries, two parameters were varied both in the simulation environment and in the PCB design process as detailed in Chapter 4. These parameters are the loop length (l) and the loop width (w), as defined previously in Figure 17. This variation is intended to demonstrate the influence of each parameter on the resulting inductance profile, which can subsequently inform the design of busbars and other current carrying conductors. Figure 55(a) shows the seven individual PCBs used to implement the different rectangular loop geometries considered in this thesis. See Table 4 and Table 5 for the detailed specifications of each test conductor geometry. Figure 55(b) shows the measurement

setup utilized for evaluation of the Geometry 8 test case. A complete empirical validation of the FEA predictions presented in Chapter 4 is provided in the next section.

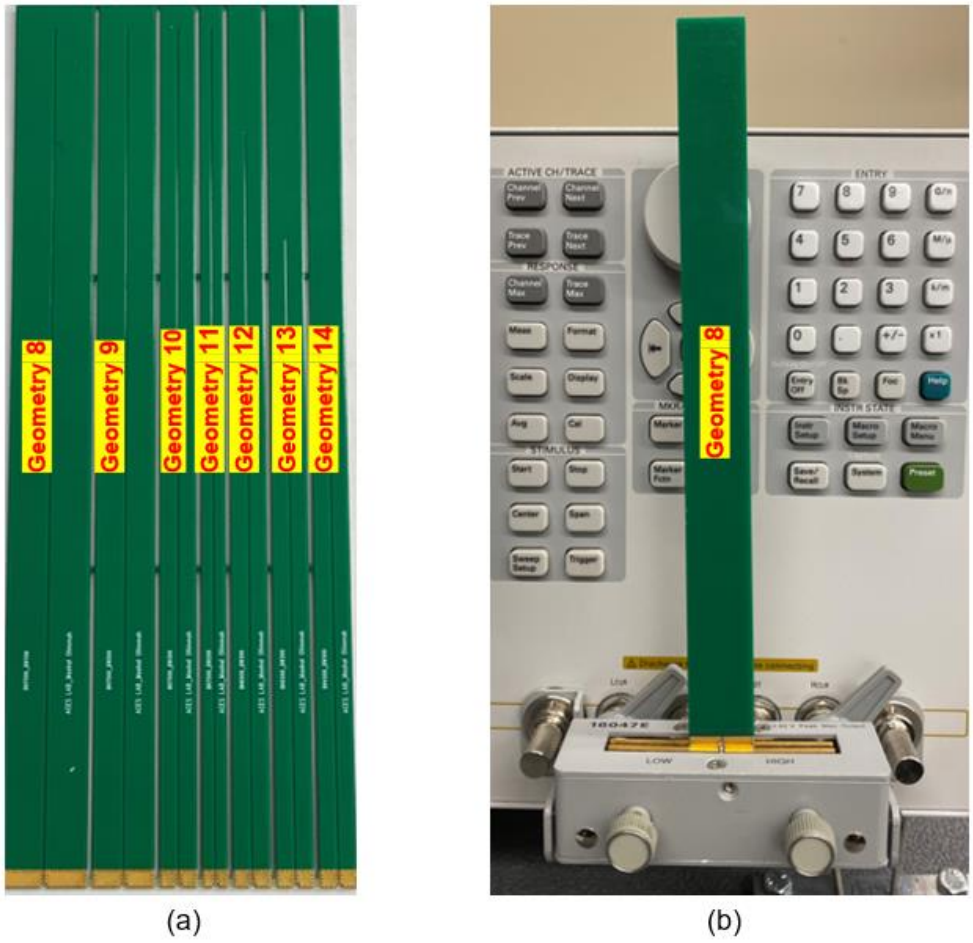

Figure 55: (a) Seven rectangular test loop side-by-side (Geometry 8 to Geometry 14), (b) Empirical setup of Geometry 8 rectangular loop conductor

5.4. Empirical Validation of FEA Predictions

This section compares the empirical impedance measurements for each test conductor geometry against the impedance profile predicted by COMSOL and presented in Chapter 4. In addition, where applicable, the theoretical predictions from Chapter 3 are included as well. For example, Figure 56 presents a comparison of the analytical approximations, the COMSOL predictions, and the empirical measurements of inductance for the round loop test cases of Geometry 2 and Geometry 5. Although only two test cases are shown in Figure 56 for the sake of clarity, all test cases show similar trends and good agreement. From Figure 56, the analytical model of Chapter 3 compares reasonably well with both the COMSOL predictions of Chapter 4 and the empirical measurement of Chapter 5 across frequency. This comparison suggests that the COMSOL models for these geometries can be used to accurately predict the inductance of circular loop conductor geometries for which the dominant frequency dependence results from skin effect.

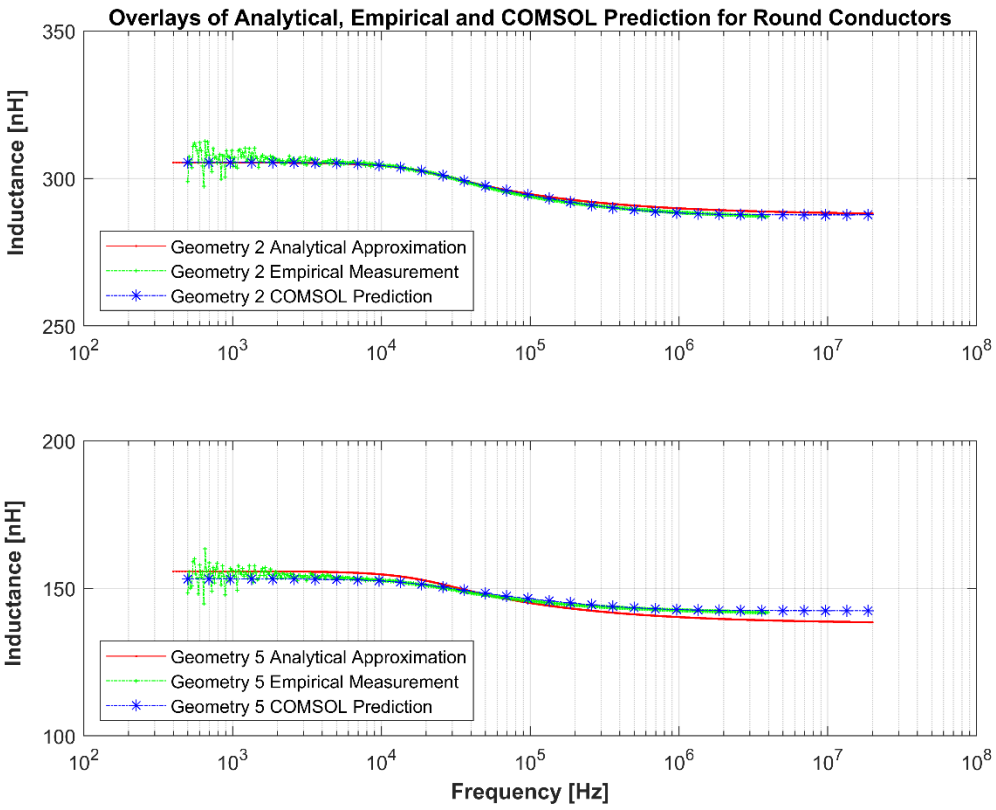

Figure 56: Analytical Approximation (Equation (41)), Empirical Measurement, and COMSOL prediction for select circular geometries

Figure 57 presents a comparison of the analytical approximations and the COMSOL predictions of internal inductance for the circular loop test cases of Geometry 2 and Geometry 5. It is noted that these two predictions for internal inductance are in good agreement across the entire frequency range shown in Figure 57. Because there is no way to isolate the internal inductance of the DUT from the total inductance, which is measured with the impedance analyzer, the empirical measurement comparison is omitted from Figure 57. Table 12 shows a comprehensive

summary of the analytical predictions, the empirical measurements, and the COMSOL predictions of inductance for the four circular loop test cases at DC or low-frequency.

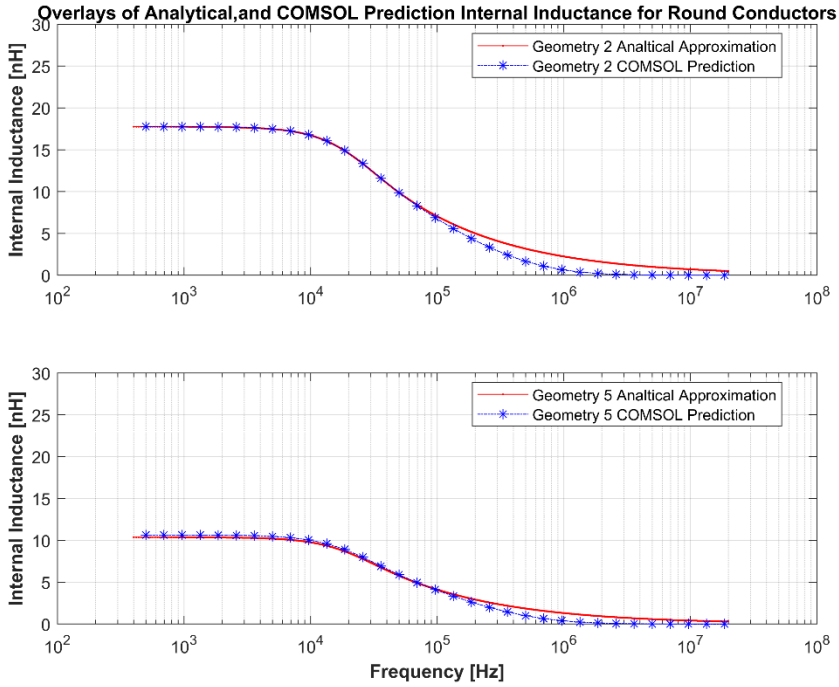

Figure 57: Analytical Approximation (Equation (41)), and COMSOL prediction for Internal inductance of select round loops

TABLE 12
CIRCULAR LOOP INDUCTANCE MEASUREMENTS AND MODEL PREDICTIONS

Geometry Number	DUT Target Inductance [nH]	Analytical Prediction @ DC [nH]	Empirical Measurement @500 Hz [nH]	COMSOL Prediction @500 Hz [nH]	Analytical Internal Inductance @ DC [nH]	COMSOL Internal Inductance @ 500 Hz [nH]
2	300	302.86	307.36	309.44	17.75	17.76
3	250	237.85	241.58	242.92	14.61	14.76
4	200	208.92	209.26	214.92	13.17	13.58
5	150	154.80	153.96	155.16	10.37	10.65

Figure 58 presents a comparison of the analytical approximations, the COMSOL predictions, and the empirical measurements of AC resistance for the round loop test cases of Geometry 2 and Geometry 5. The results of Figure 58 demonstrate good agreement between both prediction methods and the empirical measurements from low-frequency to about 1 MHz. Above this frequency, there is an observed divergence of both the COMSOL prediction and the empirical measurement from the ideal case predicted by the analytical approximation. The high-frequency discrepancy demonstrated by the COMSOL model is likely the result of the mesh configuration employed, as accurately predicting high-frequency AC resistance requires extremely small mesh elements or a boundary layer mesh [124] . Such a configuration is difficult to simulate due to the computational complexity and the associated risk of convergence failure. The reason for the divergence of the theoretical model from the empirical measurement is less clear. This may

indicate a metrology issue, but this has not been analyzed further. Table 13 shows a comprehensive summary of the analytical predictions, the empirical measurements, and the COMSOL predictions of AC resistance for the four circular loop test cases.

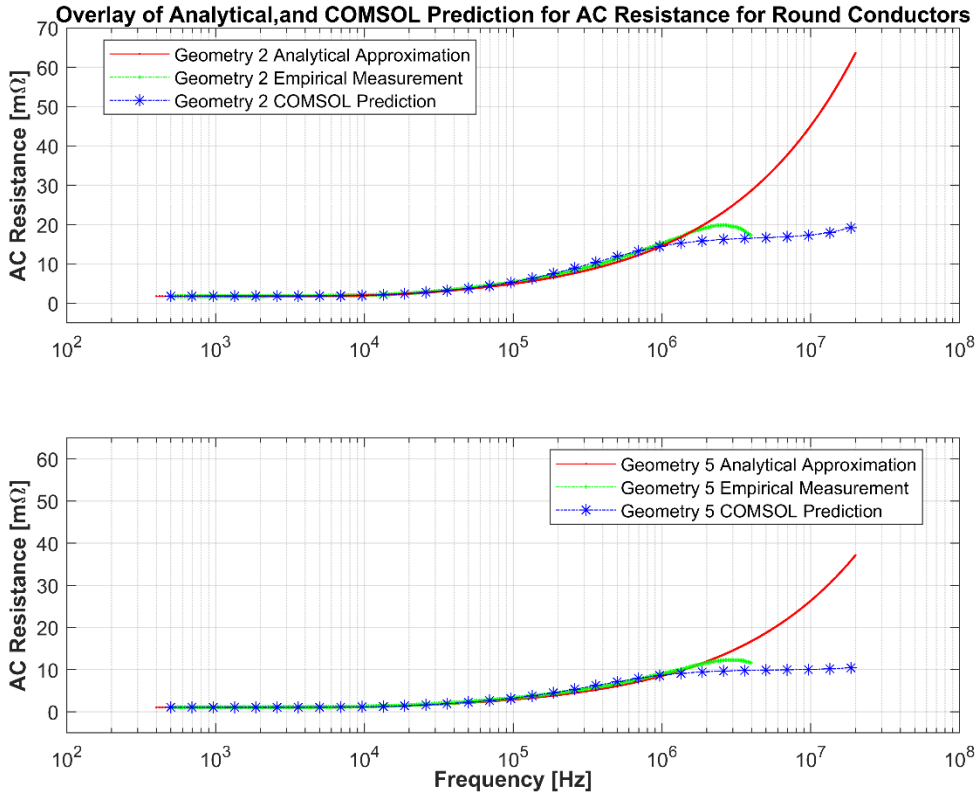

Figure 58: Analytical Approximation (Equation (41)), Empirical Measurement, and COMSOL prediction of AC Resistance for select Circular loops

TABLE 13
CIRCULAR LOOP RESISTANCE MEASUREMENTS AND MODEL PREDICTIONS

Geometry Number	Circumference [m]	Analytical Prediction @ DC [mΩ]	Empirical Measurement @500 Hz [mΩ]	COMSOL Prediction @500 Hz [mΩ]
2	0.355	1.79	1.79	1.80
3	0.292	1.47	1.47	1.48
4	0.263	1.33	1.35	1.36
5	0.207	1.05	1.06	1.06

Figure 59 presents a comparison of the analytical approximations, the COMSOL predictions, and the empirical measurements of inductance for the rectangular loop test cases of Geometry 8 and Geometry 14. Although only two test cases are shown in Figure 59 for the sake of clarity, all test cases show similar trends and good agreement. The results of Figure 59 show good agreement between the empirical measurement and COMSOL prediction across frequency. Presently, there is no analytical model that can predict the frequency-dependence of inductance for arbitrarily sized rectangular loops that are subject to proximity effect. Consequently, a fixed value obtained through low-frequency approximation is used to represent the analytical prediction shown in Figure 59. Table 14 shows a comprehensive summary of the analytical predictions, the empirical measurements, and the COMSOL predictions of inductance for the seven rectangular loop test cases. This comparison suggests that the COMSOL models for these geometries can be used to accurately predict the inductance of rectangular loop conductor geometries for which the frequency dependence results from both the skin effect and the proximity effect.

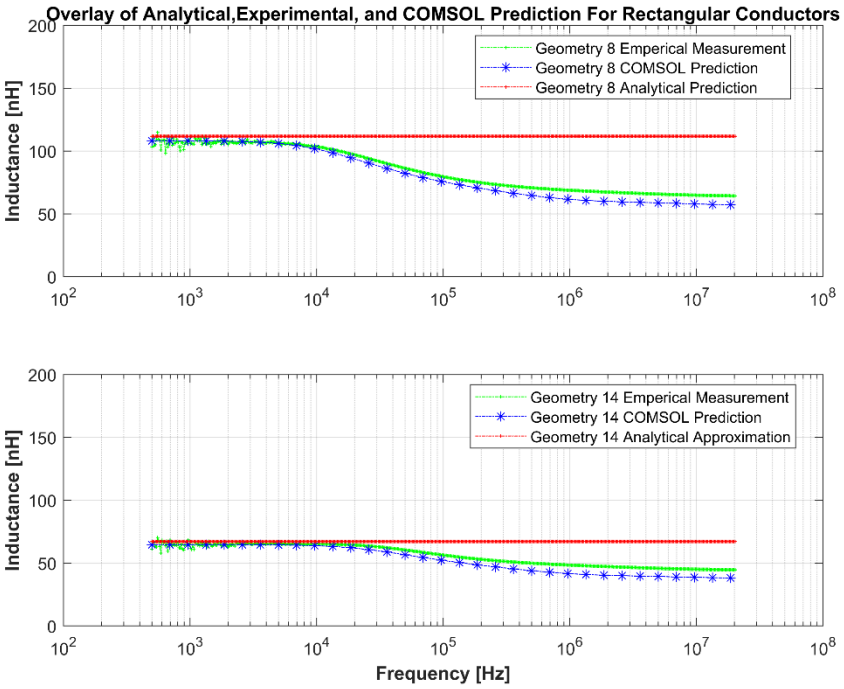

Figure 59: Analytical Approximation (Equation (49)), COMSOL prediction, and Impedance Analyzer Measurement of Total Inductance of Rectangular Loop across frequency.

TABLE 14
RECTANGLE LOOP MEASUREMENT RESULTS

Geometry Number	Analytical Prediction @ DC [nH]	Empirical Measurement @500 Hz [nH]	COMSOL Prediction @500 Hz [nH]	COMSOL Internal Inductance @ 500 Hz [nH]
8	111.6	110.02	112.13	2.41
9	112.5	110.21	112.00	3.14
10	114.6	110.57	113.07	4.65
11	117.4	117.32	117.78	6.20
12	96.70	97.70	98.24	4.04
13	81.95	81.23	83.41	3.43
14	67.12	67.47	68.63	2.93

Figure 60 presents a comparison of the analytical approximations, the COMSOL predictions, and the empirical measurements of AC resistance for the rectangular loop test cases of Geometry 8 and Geometry 14. The results of Figure 60 demonstrate good agreement between the COMSOL prediction and the empirical measurement for the entire frequency range considered. On the other hand, the analytical approximation for AC resistance is only accurate up to about 10 kHz. Above this frequency, the conductor resistance increases exponentially as expected due to skin and proximity effect. However, at present, there is no analytical model that can accurately

predict the frequency-dependence of AC resistance for arbitrarily sized rectangular loops that are subject to proximity effect. Therefore, a fixed value obtained through low-frequency approximation is used to represent the theoretical prediction shown in Figure 60. Table 15 shows a comprehensive summary of the analytical predictions, the empirical measurements, and the COMSOL predictions of AC resistance for the seven rectangular loop test cases. Overall, these results indicate good agreement between the empirical measurements and the COMSOL predictions across the considered variations in conductor geometry.

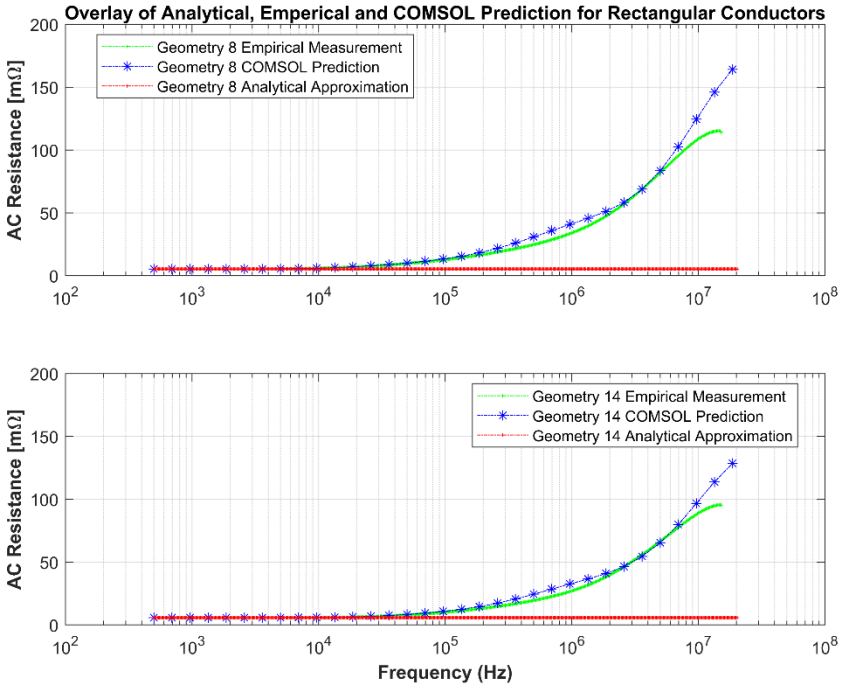

Figure 60: Analytical Approximation (Equation (50)), COMSOL prediction, and Impedance Analyzer Measurement of Total Inductance of Rectangular Loop across frequency

TABLE 15

AC RESISTANCE MEASUREMENTS OF RECTANGULAR LOOP

Geometry Number	Empirical Measurement @500 Hz [mΩ]	COMSOL Prediction @500 Hz [mΩ]
8	5.25	4.20
9	8.38	5.80
10	12.48	9.53
11	18.28	14.14
12	9.50	8.27
13	9.50	7.02
14	7.61	5.77

5.5. Summary of Empirical Evaluation

This chapter presents the empirical validation of the analytical approximations of Chapter 3 and the FEA predictions of Chapter 4. The experimental results presented in this chapter were obtained using a properly calibrated impedance analyzer. Overall, the results from the empirical measurements are found to be in good agreement with both the analytical approximations from Chapter 3 and the COMSOL predictions from Chapter 4. However, there are two limitations of the analysis and validation presented in this chapter. First, there is no way to isolate the internal impedance of conductors using empirical methods such as impedance analyzer measurements. Thus, the separation of internal and external impedance quantities that was presented in Chapter 3 and Chapter 4 could not be validated experimentally. Second, there is no analytical model that can accurately predict the frequency-dependence of AC resistance for arbitrarily sized rectangular loops that are subject to proximity effect. Thus, the comparisons presented in this chapter for the rectangular test case geometries are limited to the empirical validation of the COMSOL impedance predictions over frequency. Nevertheless, these constraints do not limit the utility of the presented COMSOL models; nor do they detract from the empirical validation of these models. Thus, the COMSOL models presented in Chapter 4 and empirically validated in this chapter can be used without restriction to predict the frequency-dependent impedance of the types of conductor geometries considered in this thesis.

CHAPTER 6:

MATHEMATICAL MODELING OF INDUCTANCE

The preceding chapters of this thesis have presented the analytical prediction, the FEA simulation, and the empirical validation of conductor impedance across frequency. As a concluding part of this thesis, a simple mathematical model, which can predict the frequency-dependence of conductor inductance, is formulated. This simple model can be easily integrated into SPICE simulations of complex circuits to more accurately represent the influence of conductor impedance, especially at high frequency. This model also accurately predicts the influence of skin effect and proximity effect for conductors of arbitrary shape and cross-section. It is noted that Chapter 2 of this thesis references several models that have been used previously to represent the frequency-dependence of conductor impedance for many geometries. However, many of the models presented in Chapter 2 are difficult to implement in SPICE simulations; others are not very accurate; and others are limited to certain conductor geometries. Therefore, an alternative model is proposed in this chapter. This model is simple to implement, inexpensive in terms of computation time, and can be easily implemented in SPICE simulations. This model is a significant improvement over the conventional approach, which ignores the frequency dependence of conductors and employs fixed-value lumped parameters to represent the inductance and resistance of these structures. As demonstrated previously in this thesis, the skin and proximity effects introduce significant frequency dependence into these quantities that are not represented by the conventional approach. This chapter therefore presents a simple formulation which captures the frequency-dependent resistance and inductance of conductors in

a SPICE circuit using only a few parameters from the mathematical model. The resulting SPICE model prediction is compared to the FEA prediction for each test geometry considered in this thesis to evaluate its accuracy and predictive capability.

6.1. Conventional Model of Conductor Impedance in LTspice

This section presents a baseline model of conductor impedance using the conventional approach, using the parameters obtained for Geometry 2. As described previously, the conventional model is based on estimating the DC values of conductor impedance and implanting the estimated parasitic parameters as fixed, frequency-independent values in simulation. An example of a conventional impedance model for the Geometry 2 test case is presented in Figure 61.

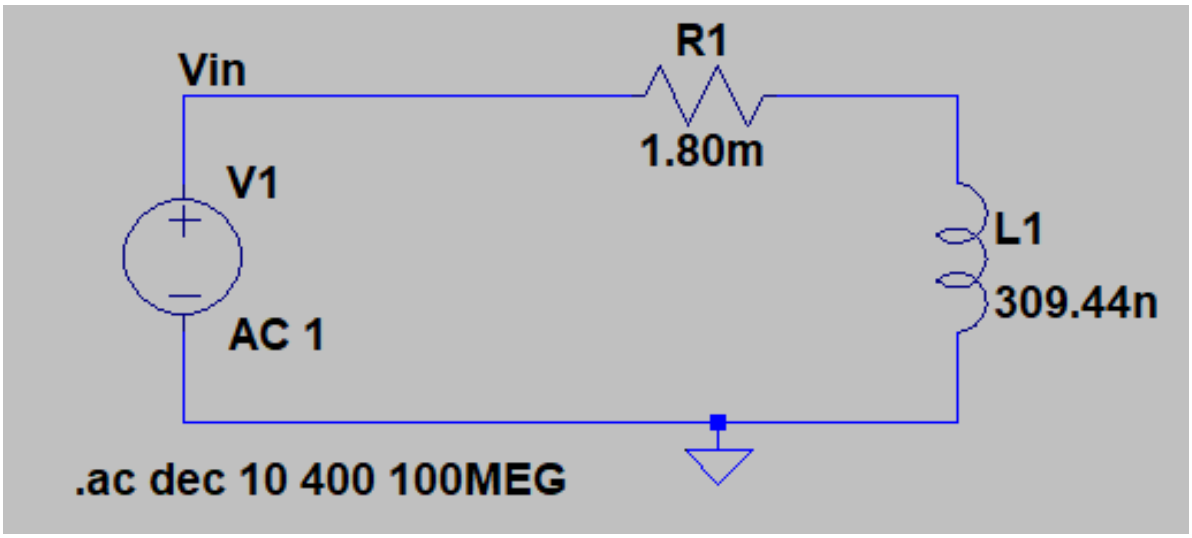

Figure 61: LTSpice Lumped-Circuit Representation of Geometry 2

The parameters for the resistance and inductance used in Figure 61 are the Geometry 2 low-frequency COMSOL predictions for both quantities. A small signal AC stimulus was applied to the equivalent circuit of Figure 61 to evaluate the impedance of this model across frequency.

This stimulus was swept with a log-spaced frequency from 500 Hz to 100 MHz with 10 steps per decade. The equivalent impedance, resistance and inductance were extracted from the SPICE simulation across frequency. The results of this analysis are compared with the COMSOL prediction for this geometry in Figure 62.

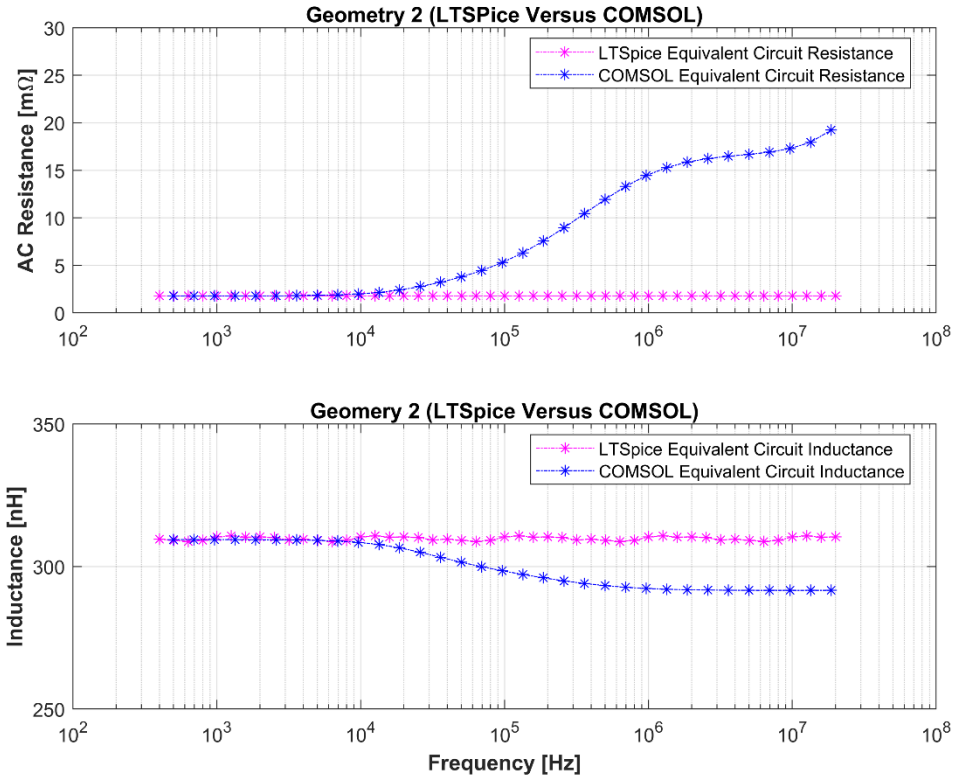

Figure 62: LTSpice Simulation vs. COMSOL Prediction

Figure 62 shows that the conventional conductor impedance model is only valid up to about 10 kHz. Above this frequency, the conventional model prediction is invalid, because the skin and proximity effects cause the conductor impedance to vary significantly from the low-frequency behavior. To capture this behavior, a frequency-dependent equivalent circuit model is required. In order to provide this circuit, a mathematical model which predicts inductance behavior across frequency must first be formulated. The parameters from this mathematical model can then be

mapped to relevant circuit elements in SPICE. The development of such a mathematical model is provided in the next section.

6.2. Mathematical Model Background

To support the formulation of a mathematical model for inductance over frequency, it is necessary to identify a suitable fitting function. This fitting function should correspond to the characteristic shape of inductance over frequency, which has been demonstrated throughout this thesis. This characteristic shape corresponds roughly to the family of sigmoid functions, reflected over the x-axis. One suitable member of this family of functions is the arctangent function. The arctangent function can be reflected over the x-axis by the following expression:

$$y = tan^{-1}x = \arctan(-x) \tag{64}$$

The x-axis reflected arctangent function is plotted in Figure 63 over the range $(-1 \leq x \leq 1)$. Figure 63 demonstrates a similar trend to the frequency-dependent inductance plots shown in previous chapters. However, it is noted that both a horizontal translation and a vertical translation is necessary for this function to be used to represent inductance. This is because frequency and inductance are only defined for positive values, and the relationship of Equation (64) is centered at the origin. In addition, it is also necessary to apply both horizontal and vertical scaling parameters to the relationship of Equation (64) in order to capture variations in inductance and frequency that are associated with different geometries. Nevertheless, Figure 63 suggests that frequency-dependent inductance can be modeled by the relationship of Equation (64), once suitable scaling and translation values are identified.

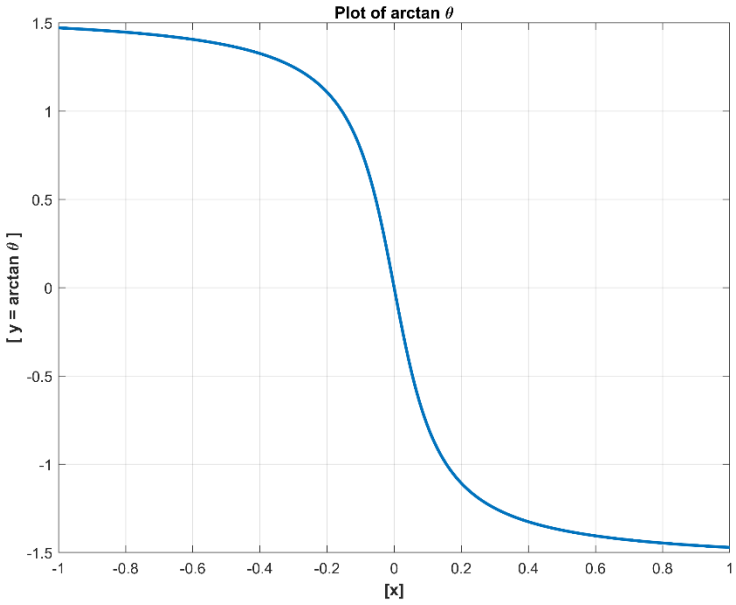

Figure 63: Plot of Equation (64)

6.3. Mathematical Model of Frequency dependent Inductance

A modified version of the relationship of Equation (64), which includes both scaling and translation values, is provided in Equation (65):

$$L(f) = tan^{-1}(f) = \frac{2}{\pi} * \mathrm{A} * arctan\,(-(f - f_c) \times C) + B \tag{65}$$

where $L(f)$ represents the total inductance in Henries (*H*), f represents the frequency in Hertz (*Hz*), A represents the vertical dimensionless scaling parameter; f_c represents the horizontal translation parameter which also corresponds to the cross-over frequency in Hertz (*Hz*), C represents the horizontal dimensionless scaling parameter, and B represents the vertical translation parameter in Henries (*H)*. Each of these parameters can be linked directly to the characteristics of the inductance profile. For example, parameters A and B can be easily estimated from the low-frequency and high-frequency inductance approximations of Equation (31) and Equation (34), respectively.

$$A \cong \frac{\left((L_i)_{lf} - (L_i)_{hf}\right)}{2} \tag{66}$$

$$B \cong \frac{\left((L_i)_{lf} + (L_i)_{hf}\right)}{2} \tag{67}$$

On the other hand, the values for C and f_c are geometry dependent. The values of these parameters must be obtained through curve fitting to the inductance profile for a particular geometry. However, once this is done, the values of C and f_c can be re-used for permutations of a given geometric structure. As shown in this chapter, these values do not change significantly for scaled versions of the same geometry type. Fitting the model of Equation (65) and then scaling to different sizes of geometry enables the prediction of inductance for structures that are yet to be built or that are impractical to measure directly. As a practical matter, it is noted that the frequency translation parameter f_c corresponds to the so called "cross-over" frequency (in Hz), which occurs at the median inductance value.

6.3.1. Curve-Fitting of Mathematical Model to Circular Loop Geometry

As a starting point, the mathematical model of Equation (65) was applied to the inductance profile for the Geometry 1 test case. Parameter A was determined from Equation (66), and parameter B was determined from Equation (67). Values for parameters C and f_c were obtained through curve-fitting the COMSOL inductance data using the MATLAB curve-fitting toolbox. A comparison of the resulting mathematical model prediction of inductance and the COMSOL prediction of inductance for Geometry 1 is shown in Figure 64. As shown in Figure 64, the mathematical model of Equation (65) provides good agreement with the COMSOL prediction for inductance for Geometry 1 across the entire frequency range considered. The

model parameter values that achieved the agreement shown in Figure 64 for Geometry 1 are as follows: $A = 30.47$, $B = 1055.0$, $C = 2.00$, and $f_c = 4.80$.

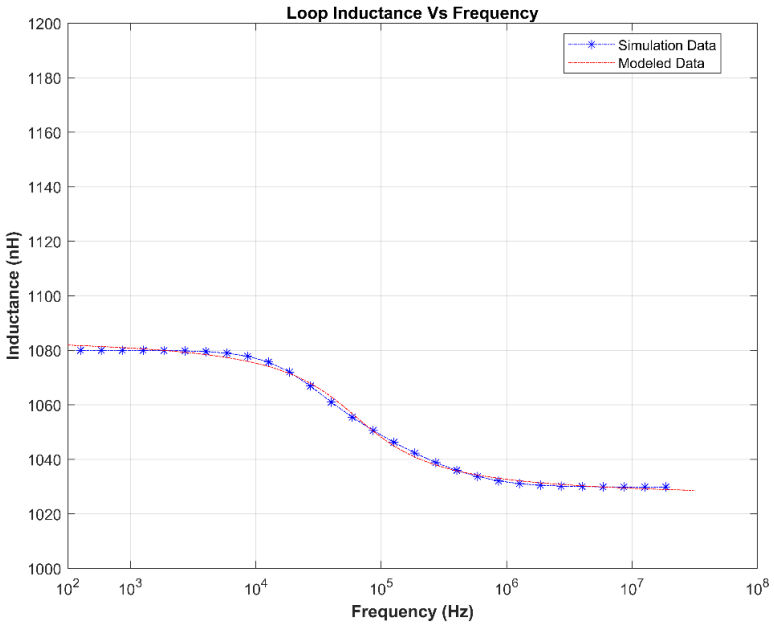

Figure 64: Comparison of Mathematical Model Prediction and COMSOL Prediction for Geometry1

6.3.2. Predictive Capabilities of Mathematical Model for Round Loop Geometry

This section evaluates the predictive capability of the mathematical model presented in Equation (65) by leveraging this model to predict the frequency-dependent inductance for the remaining round loop geometries (Geometry 2 to Geometry 5) without curve fitting the measured data for these structures. This process was realized by directly computing model parameters A and B from Equation (66) and Equation (67), respectively. The C and f_c parameter values that were estimated from curve-fitting Geometry 1 are re-used for predicting the frequency-dependent inductance of Geometry 2 to Geometry 5. The accuracy of the resulting inductance predictions are shown in Figure 65 by comparison to the COMSOL model predictions for these geometries. As shown in Figure 65, the resulting mathematical model predictions demonstrate good agreement with the COMSOL predictions for all four geometries

across the full frequency range considered. This confirms that the mathematical model presented in Equation (65) can be readily re-used once the values for the geometry-specific parameters C and f_c are known. As a result, the mathematical model presented in Equation (65) is shown to be a powerful and useful tool for predicting the frequency-dependent inductance of conductor geometries for which the dominant frequency dependence results from skin effect.

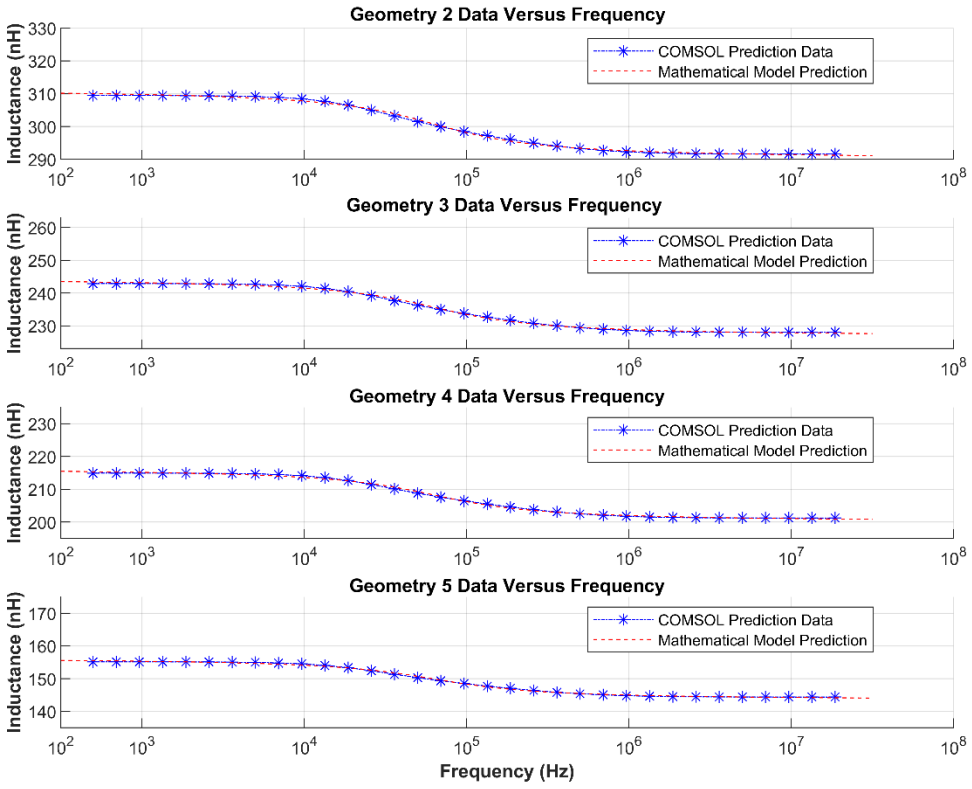

Figure 65: Circular loop Geometries (COMSOL Prediction Versus Mathematical Model Prediction (Equation (65)))

6.3.3. Curve-Fitting of Mathematical Model to Rectangular Loop Geometry

The mathematical model presented in Equation (65) was also applied to the rectangular loop test cases presented in the previous chapter (Geometry 8 to Geometry 14). For these geometries, the modeling process relies more heavily on measured inductance data, because theoretical

approximations for the low-frequency and high-frequency inductance of arbitrarily sized rectangular loops are not available. However, measured values of inductance at low-frequency and high-frequency can still be utilized to determine parameter values of model parameters A and B using Equation (66) and Equation (67), respectively. However, the values of the geometry-specific parameters C and f_c must be obtained by curve-fitting measured inductance data or COMSOL model predictions. To evaluate the influence of conductor geometry on the values of these parameters, the mathematical model presented in Equation (65) was curve-fit to the measured inductance data for each of the seven rectangular geometries. Figure 66 shows the effect of varying the loop width (w) for the rectangular geometries. In general, the loop width (w) is shown to be directly proportional to the inductance magnitude, but the inductance reduction at high frequency is also dependent on this parameter. Figure 67 shows the effect of varying the loop length (l) for the rectangular geometries. In general, the loop length (l) is shown to primarily affect the inductance magnitude drop at high frequency. Figure 66 and Figure 67 demonstrate good agreement between the mathematical model presented in Equation (65) and the COMSOL inductance predictions across frequency for these test geometries. This demonstrates that the mathematical model presented in Equation (65) is able to represent the influence of both the skin and proximity effects.

A summary of the model parameters that were used to provide model agreement shown in Figure 65, Figure 66 and Figure 67 for the circular and rectangular geometries are presented in Table 16, Table 17, and Table 18. The relationships between the model parameter values and the characteristics of the rectangular geometry profile are more complex than the relationships observed for the circular loop geometries. For example, while variation in the width (w) geometry parameter is linked primarily to mathematical model parameters A and B, variation in

the length (l) geometry parameter is linked to all four parameters of the mathematical model. Thus, it may be possible to predict the frequency-dependent inductance profile for rectangular geometry profiles with permutations in width, using a similar procedure to that leveraged for the round conductor geometries. However, predicting the frequency-dependent inductance profile for rectangular geometry profiles with permutations in length is significantly more challenging. This is because the length parameter also affects the geometry-specific parameters C and f_c. Thus, it is not practical to find suitable parameter values for a 'baseline' rectangular case and re-use these values for permutations of this geometry that vary in length. As a result, curve-fitting of all four mathematical model parameters is likely the most practical method for adapting the mathematical model presented in Equation (65) to this type of geometry.

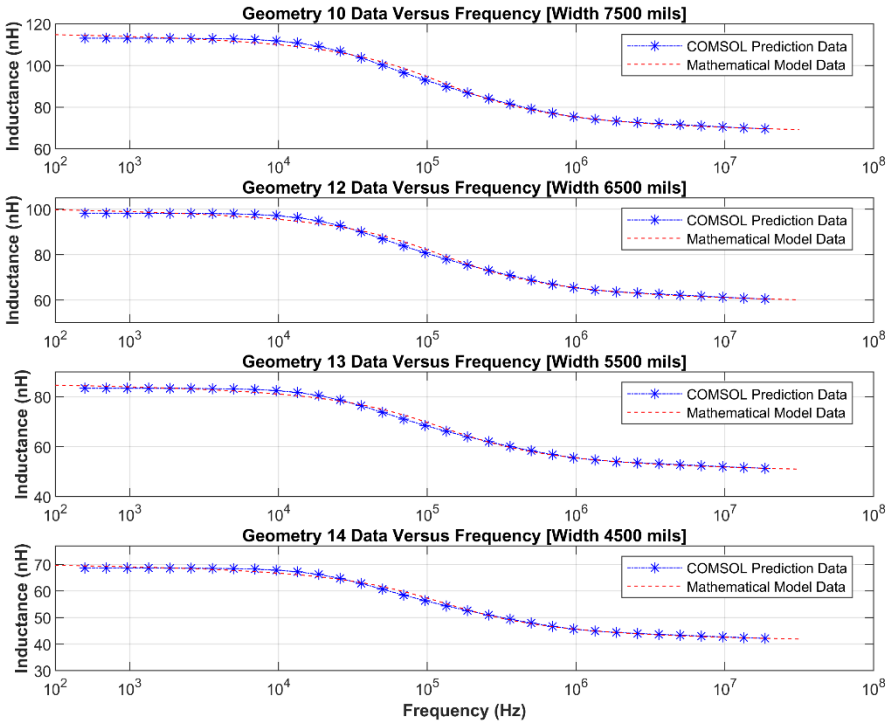

Figure 66: Rectangular loop Geometries (COMSOL Prediction vs. Mathematical Model (Equation (65))) (Width Variation)

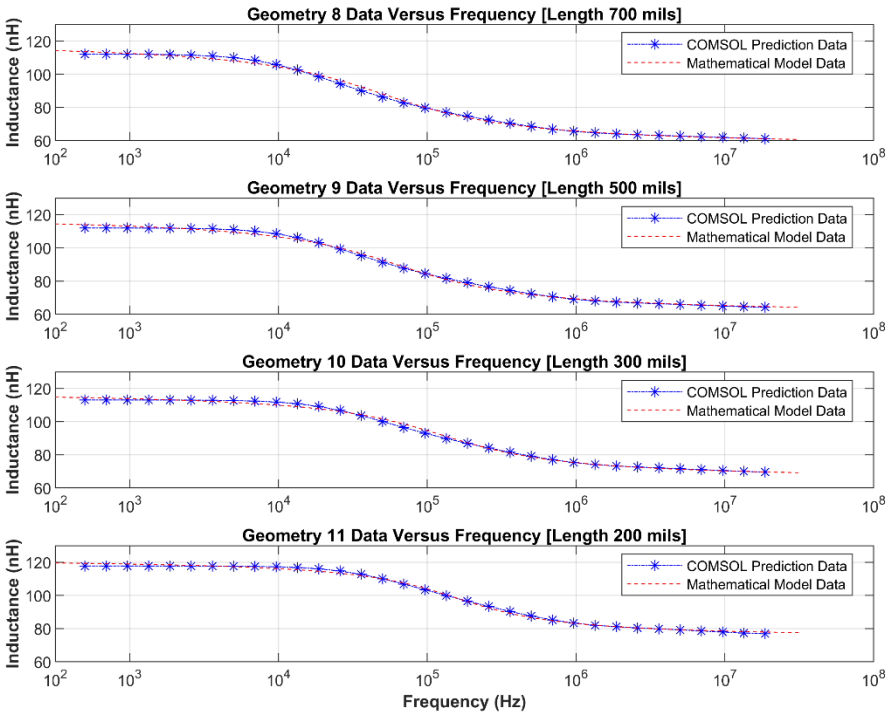

Figure 67: Rectangular loop Geometries (COMSOL Prediction vs. Mathematical Model (Equation (65))) (Length Variation)

TABLE 16

CIRCULAR LOOP MODEL PREDICTION RESULTS

Geometry Number	Model Parameter A	Model Parameter B [nH]	Model Parameter C	Model Parameter Log f_c Log [Hz]	Coil Radius [cm]
1	30.47	1055.00	2.00	4.80	15.92
2	10.91	300.70	2.00	4.80	5.65
3	9.09	235.70	2.00	4.80	4.65
4	8.38	208.20	2.00	4.80	4.19
5	6.59	149.90	2.00	4.80	3.30

TABLE 17

RECTANGULAR LOOP MODEL PREDICTION RESULTS (VARYING LENGTH)

Geometry Number	Model Parameter A	Model Parameter B [nH]	Model Parameter C	Model Parameter Log f_c Log [Hz]	Coil Width [mils]	Coil Length [mils]
8	32.39	88.10	1.45	4.70	7500	700
9	30.03	89.78	1.52	4.80	7500	500
10	26.98	91.83	1.60	5.10	7500	300
11	24.26	98.32	1.88	5.20	7500	200

TABLE 18

RECTANGULAR LOOP MODEL PREDICTION RESULTS (VARYING WIDTH)

Geometry Number	Model Parameter A	Model Parameter B [nH]	Model Parameter C	Model Parameter Log f_c Log [Hz]	Coil Width [mils]	Coil Length [mils]
10	26.98	91.83	1.60	5.10	7500	300
12	23.45	79.79	1.60	5.10	6500	300
13	19.94	67.72	1.60	5.10	5500	300
14	16.46	55.68	1.60	5.10	4500	300

6.4. LTSPICE Simulation of Frequency-Dependent Impedance

In the literature, complex ladder models [36], [37], [42] have been proposed to represent the frequency-dependent impedance of conductors and transmission lines. These models can be used directly in modeling tools such as LTspice. However, these models generally contain many elements and are therefore expensive in terms of computation time. As an alternative to this approach, a simple equivalent circuit model which leverages the mathematical model presented in Equation (65) is proposed. A similar model has been presented previously in [125]. However, this prior model does not account for variation in resistance at high frequency. For the cases considered by this thesis, utilizing the circuit model of [125] predicts a value for cross-over frequency that is an order of magnitude lower than the actual value. This makes the model of [125] inadequate for predicting the frequency-dependence of conductor impedance for WBG applications. The model presented herein addresses both of these challenges. The proposed equivalent circuit model, which is based on the mathematical model presented in Equation (65), is shown Figure 68.

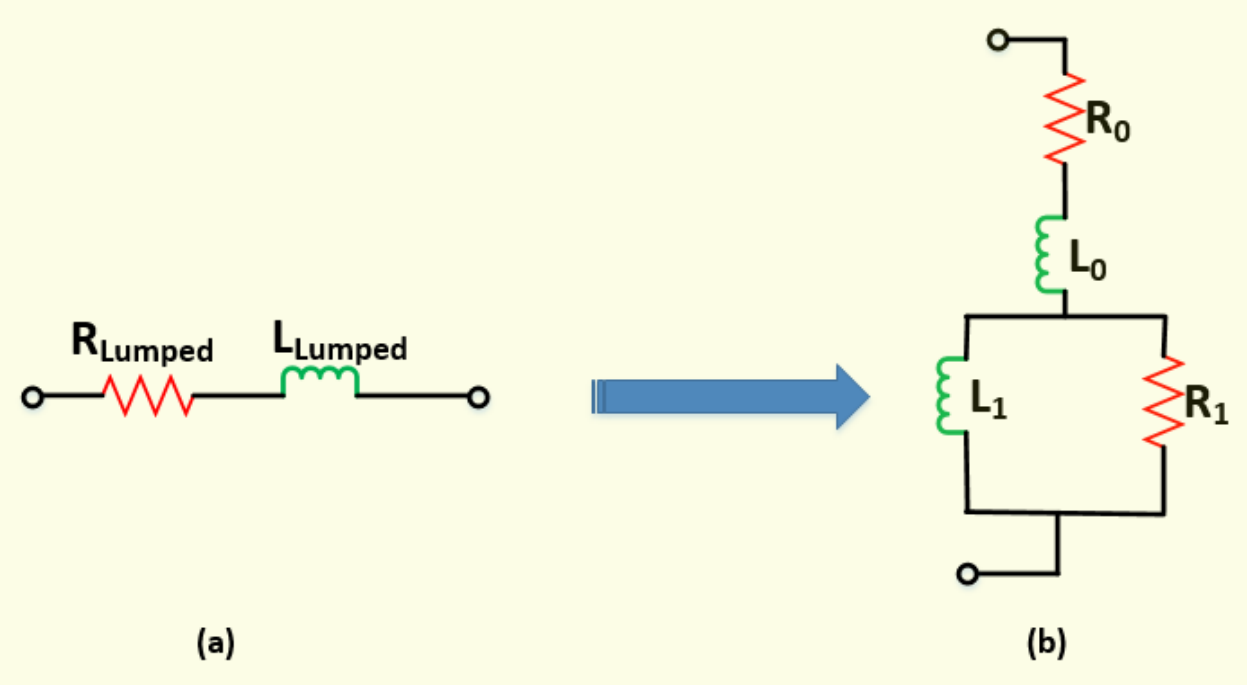

Figure 68: (a) Conventional Conductor Equivalent circuit, and (b) Proposed Frequency-Dependent Conductor Equivalent Circuit

In the equivalent circuit model of Figure 68, R_0 represents the low-frequency resistance prediction in (Ω); R_1 represents the incremental resistance prediction at high frequency in (Ω); L_0 represents the high-frequency inductance prediction in (H), and L_1 represents the total inductance drop prediction from low-frequency to high-frequency in (H).

The circuit of Figure 68(b) can be readily analyzed in terms of a low-frequency equivalent and a high-frequency equivalent. At low frequency, the impedance of L_1 is lower than R_1. Thus, the current favors L_1 and the equivalent circuit at low frequency is approximately the series combination of R_0, L_0 , and L_1. At high frequency, R_1 is lower than the impedance of L_1. Thus, the current favors R_1, and the equivalent circuit at high frequency is approximately the series combination of R_0, L_0 , and R_1.

The equivalent circuit parameters of Figure 68 (b) can be mapped to the relevant mathematical model parameters of Equation (65) as follows:

$$L_0 = B - A \tag{68}$$

$$L_1(f) = 2 \times A \tag{69}$$

$$R_1(f_c) = 2 \times pi \times (f_c) \times L_1 \tag{70}$$

For the purpose of fitting the parameters of the mathematical model to these equivalent circuit values, several useful approximations can be identified. For example, A corresponds to the positive or negative offset inductance from the median value in Henries (H); B corresponds to the median inductance values in Henries (H); and f_c corresponds to the cross-over frequency value in hertz (Hz).

By applying Equations (68)-(70), the equivalent circuit parameter values for each test geometry can be readily calculated. It is noted that the DC resistance parameter (R_0) is not included in the previous estimation process. This parameter can be obtained from the COMSOL predictions of Chapter 4 or the empirical measurements of Chapter 5. However, it is generally necessary to further adjust this parameter to provide good agreement between the prediction of the equivalent circuit model and the empirical measurements for each test geometry. This adjustment is necessary due to the simple nature of the SPICE equivalent circuit proposed here. It may be possible to address this challenge by using a more complex equivalent circuit. However, this would come at the cost of additional computational overhead during transient simulation. A summary of the equivalent circuit parameters obtained by applying this procedure to each of the test case geometries is provided in Table 19.

TABLE 19
EQUIVALENT FREQUENCY-DEPENDENT CIRCUIT PARAMETERS

Geometry Number	**Cross-Over Frequency Log [Hz]**	**A**	**B [nH]**	**L_0 [nH]**	**L_1 [nH]**	**$R_1(f_c)$ [mΩ]**	**R_0 (DC) [mΩ]**	**R_0 (DC) $Modified$ [mΩ]**
1	4.80	30.47	1055.0	1.025e3	60.94	24.16	5.05	3.35
2	4.80	10.91	300.70	289.10	21.82	8.65	1.80	0.1
3	4.80	9.09	235.70	226.61	18.18	7.21	1.48	0.05
4	4.80	8.38	208.20	199.82	16.76	6.64	1.36	0.02
5	4.80	6.59	149.90	143.31	13.18	5.23	1.06	0.01
8	4.70	32.39	88.10	55.71	64.78	20.40	4.20	2.25
9	4.80	30.03	89.78	59.75	60.06	23.81	5.80	3.85
10	5.10	26.98	91.83	64.85	53.96	42.68	9.53	7.58
11	5.20	24.26	98.32	74.06	48.52	48.32	14.14	12.19
12	5.10	23.45	79.79	56.34	46.90	37.10	8.27	6.32
13	5.10	19.94	67.72	47.78	39.88	31.55	7.02	5.07
14	5.10	16.64	55.68	39.04	33.28	26.33	5.77	3.82

Figure 69 presents an LTspice implementation of the equivalent circuit model for Geometry 2 using the parameters of Table 19. A small signal AC stimulus was applied to the equivalent circuit of Figure 69 evaluate the impedance of this model across frequency. This stimulus was swept with a log-spaced frequency from 400 Hz to 30 MHz with 10 steps per decade. The results of this simulation study are compared to the associated COMSOL model prediction in Figure 70.

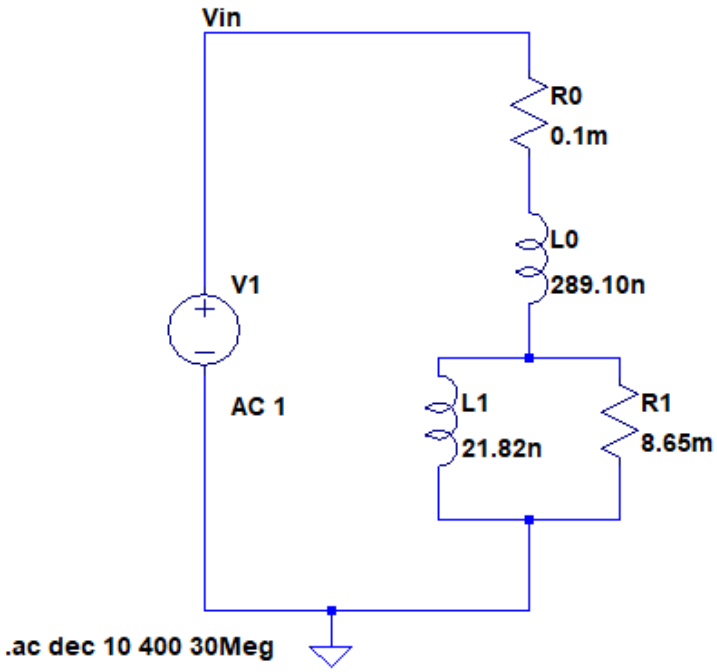

Figure 69: Geometry 2 Equivalent Frequency-Dependent LTspice Simulation

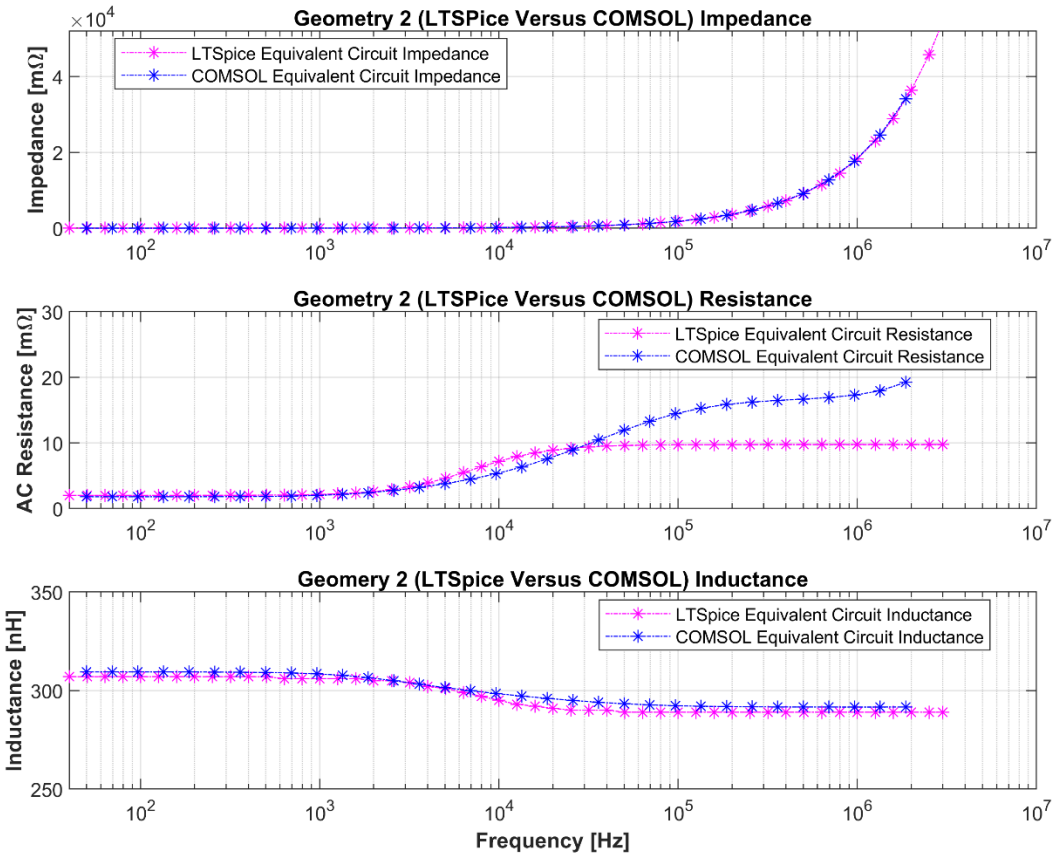

Figure 70: Comparison between LTSpice Simulation and COMSOL prediction

As shown in Figure 70, the impedance prediction of the proposed equivalent circuit model for Geometry 2 demonstrates good agreement with the COMSOL prediction across the entire frequency range considered. The impedance magnitude prediction and the inductance prediction of this equivalent circuit model demonstrate particularly good agreement with the COMSOL model. However, there is some modest discrepancy in the resistance prediction of the equivalent circuit model at high frequency. The high-frequency resistance is expected to increase with frequency in proportion to $f^{1/2}$ due to skin effect [125]. However, the simple equivalent circuit model presented here does not have sufficient degrees of freedom to represent this behavior.

Nevertheless, the difference in the prediction of the equivalent circuit model and the behavior of real conductors at high frequency is expected to be small. The most important frequency-dependent characteristics of realistic conductor behavior are accurately captured by the equivalent circuit presented here. Although only a single geometry is shown in Figure 70 for the sake of clarity, all test cases show similar trends and good agreement. An assessment of the equivalent circuit model impedance prediction for an example rectangular loop geometry (Geometry 8) is included in Appendix A.7 of this thesis.

6.5. Summary of Mathematical Modeling

This chapter presents a simple mathematical model that accurately predicts the influence of the skin and proximity effects in the context of conductor impedance. This model is applied to several test case conductor geometries in this chapter. The predictions of this mathematical model demonstrate good agreement with the COMSOL predictions for each considered geometry. This mathematical model is further utilized to develop a simple equivalent circuit model that can be directly implemented in circuit simulators such as LTspice. This equivalent circuit model is simple to calibrate and inexpensive in terms of computation time. It is shown herein that this equivalent circuit model can be easily calibrated to represent the frequency-dependent inductance of practical conductors.

CHAPTER 7:

CONCLUSION AND FUTURE WORK

7.1. Conclusion

The goal of this thesis is to investigate, understand, and model the frequency-dependent impedance of conductors. This goal is motivated by the need to accurately model conductors in multi-chip power modules and converters employing WBG semiconductor technology in the field of power electronics. WBG semiconductors offer numerous advantages over traditional Silicon semiconductors due to their improved material properties. As a result of these improved material properties, switching frequencies greater than 100 kHz are attainable in conjunction with significant loss reduction compared to traditional Silicon semiconductors. However, due to the switching speeds achievable with WBG semiconductors, high-frequency dynamic effects are introduced, which cannot be ignored by application designers. In this context, the frequency-dependent impedance of the conductors found in MCPMs and converters becomes important. Fixed-value, lumped-parameter models, which are commonly used for representing the impedance of these elements, are inadequate for accurately modeling such systems. This is especially true for time-domain simulations implemented in circuit modeling tools such as SPICE.

The frequency-dependence of conductor impedance is linked to two well-known physical phenomena: the skin effect and the proximity effect. Fortunately, significant work has been done toward quantifying the influence of skin effect using analytical models. On the other hand, the proximity effect is very difficult to model analytically, for several reasons. First, the proximity

effect is strongly dependent on geometry characteristics, such as the distance of separation between neighboring conductors. Second, the symmetric distribution of current in conductors subject to proximity effect is disrupted in ways that are difficult to predict. This leads to a corresponding distortion in the magnetic and electric fields. Overall, the influence of proximity effect is much more difficult to predict than the influence of skin effect for arbitrary conductor geometries.

Despite these challenges, this thesis introduces an effective mathematical model for representing the frequency dependence of conductor impedance. This model is behavioral in nature and can be easily tuned to represent the variation in conductor impedance over frequency that results from both the skin effect and the proximity effect. This model is shown to accurately represent the impedance of conductors of arbitrary shape and cross-section. In addition, this mathematical model is used to develop an equivalent circuit model suitable for implementation in SPICE. This equivalent circuit model can replace the fixed-value, lumped-parameter models that are commonly used in SPICE, and which ignore the frequency dependence of conductor impedance. The equivalent circuit model presented in this thesis provides a more accurate assessment of conductor impedance across frequency than can be obtained using conventional models. In addition, the proposed equivalent circuit can be easily tuned to empirical impedance measurements and is computationally efficient. Overall, the models presented in this thesis are expected to improve the fidelity of power electronic application simulations as the adoption of WBG semiconductors accelerates across the industry.

REFERENCES

[1] T. G. Wilson, “The evolution of power electronics,” *IEEE Trans. Power Electron.*, vol. 15, no. 3, pp. 439–446, 2000.

[2] H. Okumura, “Power electronics innovation by Silicon Carbide power semiconductor devices,” in *2014 IEEE International Meeting for Future of Electron Devices, Kansai (IMFEDK)*, 2014, pp. 1–2.

[3] W. Yu, H. Qian, and J. Lai, “Design of High-Efficiency Bidirectional DC–DC Converter and High-Precision Efficiency Measurement,” *IEEE Trans. Power Electron.*, vol. 25, no. 3, pp. 650–658, 2010.

[4] S. N. Soheli, G. Sarowar, M. A. Hoque, and M. S. Hasan, “A DC-DC Step Down Converter for Unprecedented Higher Efficiency,” in *2018 International Conference on Advancement in Electrical and Electronic Engineering (ICAEEE)*, 2018, pp. 1–4.

[5] J. S. Glaser *et al.*, “Direct comparison of silicon and silicon carbide power transistors in high-frequency hard-switched applications,” in *2011 Twenty-Sixth Annual IEEE Applied Power Electronics Conference and Exposition (APEC)*, 2011, pp. 1049–1056.

[6] J. C. Zolper, “Emerging silicon carbide power electronics components,” in *Twentieth Annual IEEE Applied Power Electronics Conference and Exposition, 2005. APEC 2005.*, 2005, vol. 1, pp. 11-17 Vol. 1.

[7] Z. Chen, “Characterization and Modeling of High-Switching-Speed Behavior of SiC Active Devices.” p. 188, 2009.

[8] J. Qian, A. Khan, and I. Batarseh, “Turn-off switching loss model and analysis of IGBT under different switching operation modes,” in *Proceedings of IECON ’95 - 21st Annual Conference on IEEE Industrial Electronics*, 1995, vol. 1, pp. 240–245 vol.1.

[9] S. C. Das, G. Narayanan, and A. Tiwari, “Variation of IGBT switching energy loss with device current: An experimental investigation,” in *2014 IEEE 6th India International Conference on Power Electronics (IICPE)*, 2014, pp. 1–5.

[10] A. Elasser and T. P. Chow, “Silicon carbide benefits and advantages for power electronics circuits and systems,” *Proc. IEEE*, vol. 90, no. 6, pp. 969–986, 2002.

[11] T. P. Chow, “Wide bandgap semiconductor power devices for energy efficient systems,” in *2015 IEEE 3rd Workshop on Wide Bandgap Power Devices and Applications (WiPDA)*, 2015, pp. 402–405.

[12] A. N. Lemmon, R. Cuzner, J. Gafford, R. Hosseini, A. D. Brovont, and M. S. Mazzola, “Methodology for Characterization of Common-Mode Conducted Electromagnetic Emissions in Wide-Bandgap Converters for Ungrounded Shipboard Applications,” *IEEE J. Emerg. Sel. Top. Power Electron.*, vol. 6, no. 1, pp. 300–314, 2018.

[13] N. Kaminski and O. Hilt, “SiC and GaN Devices - Competition or Coexistence?,” in *2012 7th International Conference on Integrated Power Electronics Systems (CIPS)*, 2012, pp. 1–11.

[14] Cree, “CREE CMF20120D-Silicon Carbide Power MOSFET.” .

[15] T. Nakamura, M. Sasagawa, Y. Nakano, T. Otsuka, and M. Miura, “Large current SiC power devices for automobile applications,” *2010 International Power Electronics Conference - ECCE Asia -, IPEC 2010*. pp. 1023–1026, 2010.

[16] J. He, T. Zhao, X. Jing, and N. A. O. Demerdash, “Application of wide bandgap devices in renewable energy systems - Benefits and challenges,” in *2014 International Conference on Renewable Energy Research and Application (ICRERA)*, 2014, pp. 749–754.

[17] B. W. Nelson, “Spice Modeling and Simulation of Silicon-Carbide Spice Modeling and Simulation of Silicon-Carbide Power,” University of Alabama, 2017.

[18] A. Lostetter *et al.*, “High-temperature silicon carbide and silicon on insulator based integrated power modules,” in *2009 IEEE Vehicle Power and Propulsion Conference*, 2009, pp. 1032–1035.

[19] J. Shovlin, R. Woodin, and T. Witt, “Silicon carbide in a silicon world: introducing wide band gap semiconductor production into a silicon fab,” in *2004 IEEE/SEMI Advanced Semiconductor Manufacturing Conference and Workshop (IEEE Cat. No.04CH37530)*, 2004, pp. 420–424.

[20] J. Shovlin, R. Woodin, and T. Witt, “Silicon carbide in a silicon world: introducing wide

band gap semiconductor production into a silicon fab," in *2004 IEEE/SEMI Advanced Semiconductor Manufacturing Conference and Workshop (IEEE Cat. No.04CH37530)*, 2004, pp. 420–424.

[21] D. Heer, R. Bayerer, and D. Domes, "SiC-JFET in half-bridge configuration - parasitic turn-on at current commutation," in *PCIM Europe 2014; International Exhibition and Conference for Power Electronics, Intelligent Motion, Renewable Energy and Energy Management*, 2014, pp. 1–8.

[22] J. Schuderer, U. Vemulapati, and F. Traub, "Packaging SiC power semiconductors — Challenges, technologies and strategies," in *2014 IEEE Workshop on Wide Bandgap Power Devices and Applications*, 2014, pp. 18–23.

[23] A. Lemmon and R. Graves, "Parasitic extraction procedure for silicon carbide power modules," in *2015 IEEE International Workshop on Integrated Power Packaging (IWIPP)*, 2015, pp. 91–94.

[24] C. Bailey, P. Rajaguru, and H. Lu, "Impact of wide band gap devices on power electronics packaging designs," in *2017 Pan Pacific Microelectronics Symposium (Pan Pacific)*, 2017, pp. 1–6.

[25] Cree, "CAS120M12BM2 Datasheet." 2014.

[26] Cree, "CAS325M12HM2 Datasheet." 2016.

[27] Z. Zhang, B. Guo, and F. Wang, "Evaluation of Switching Loss Contributed by Parasitic Ringing for Fast Switching Wide Band-Gap Devices," *IEEE Trans. Power Electron.*, vol. 34, no. 9, pp. 9082–9094, 2019.

[28] A. Dutta and S. S. Ang, "Effects of parasitic parameters on electromagnetic interference of power electronic modules," in *2017 IEEE Applied Power Electronics Conference and Exposition (APEC)*, 2017, pp. 2706–2710.

[29] D. Reusch and J. Strydom, "Understanding the Effect of PCB Layout on Circuit Performance in a High-Frequency Gallium-Nitride-Based Point of Load Converter," *IEEE Trans. Power Electron.*, vol. 29, no. 4, pp. 2008–2015, 2014.

[30] M. C. Caponet, F. Profumo, R. W. De Doncker, and A. Tenconi, "Low stray inductance bus bar design and construction for good EMC performance in power electronic circuits,"

IEEE Trans. Power Electron., vol. 17, no. 2, pp. 225–231, 2002.

[31] T. Hashimoto, T. Kawashima, T. Uno, N. Akiyama, N. Matsuura, and H. Akagi, "A System-in-Package (SiP) With Mounted Input Capacitors for Reduced Parasitic Inductances in a Voltage Regulator," *IEEE Trans. Power Electron.*, vol. 25, no. 3, pp. 731–740, 2010.

[32] S. Yang, J. Soh, and R. Kim, "Parasitic Inductance Reduction Design Method of Vertical Lattice Loop Structure for Stable Driving of GaN HEMT," in *2019 IEEE 4th International Future Energy Electronics Conference (IFEEC)*, 2019, pp. 1–8.

[33] E. E. Kriezis, T. D. Tsiboukis, S. M. Panas, and J. A. Tegopoulos, "Eddy Current Theory and Applications." 1992.

[34] S. Mei and Y. I. Ismail, "Modeling skin and proximity effects with reduced realizable RL circuits," *IEEE Trans. Very Large Scale Integr. Syst.*, vol. 12, no. 4, pp. 437–447, 2004.

[35] G. Gaba and M. Abou-Dakka, "A simplified and accurate calculation of frequency dependence conductor impedance," in *8th International Conference on Harmonics and Quality of Power. Proceedings (Cat. No.98EX227)*, 1998, vol. 2, pp. 939–945 vol.2.

[36] E. S. Mawuli, Y. Wu, K. Kang, and F. Sekyere, "A New GSG Pad Compact Model for Skin and Proximity Effect," in *2019 IEEE Asia-Pacific Microwave Conference (APMC)*, 2019, pp. 593–595.

[37] N. Idir, Y. Weens, and J. Franchaud, "Skin effect and dielectric loss models of power cables," *IEEE Trans. Dielectr. Electr. Insul.*, vol. 16, no. 1, pp. 147–154, 2009.

[38] A. Colavitto, A. Vicenzutti, D. Bosich, and G. Sulligoi, "Modeling of Power Cables in Shipboard IPES for assessing High Frequency Disturbances Propagation," in *2019 IEEE Electric Ship Technologies Symposium (ESTS)*, 2019, pp. 337–344.

[39] A. Pagnetti, A. Xemard, F. Paladian, and C. A. Nucci, "Evaluation of the impact of proximity effect in the calculation of the internal impedance of cylindrical conductors," *2011 30th URSI Gen. Assem. Sci. Symp. URSIGASS 2011*, pp. 1–4, 2011.

[40] S. Ramo, J. R. Whinnery, and T. Van Duzer, *Fields and waves in communication electronics*. John Wiley & Sons, 1994.

[41] A. Rong and A. C. Cangellaris, “Note on the Definition and Calculation of the Per-Unit-Length Internal Impedance of a Uniform Conducting Wire,” *IEEE Trans. Electromagn. Compat.*, vol. 49, no. 3, pp. 677–681, 2007.

[42] B. K. Sen and R. L. Wheeler, “Skin effects models for transmission line structures using generic SPICE circuit simulators,” in *IEEE 7th Topical Meeting on Electrical Performance of Electronic Packaging (Cat. No.98TH8370)*, 1998, pp. 128–131.

[43] C. Bednarz and M. Leone, “Volume-Filament-PEEC-Based Modal Network Representation for Skin and Proximity Effect in Conductors with Variable Geometry,” in *2018 International Symposium on Electromagnetic Compatibility (EMC EUROPE)*, 2018, pp. 533–538.

[44] M. Enohnyaket and J. Ekman, “PEEC Models for Air-core Reactors Modeling Skin and Proximity Effects,” in *2007 IEEE Power Electronics Specialists Conference*, 2007, pp. 3034–3038.

[45] E. Liu, E. Li, W. Ewe, H. M. Lee, T. G. Lim, and S. Gao, “Compact Wideband Equivalent-Circuit Model for Electrical Modeling of Through-Silicon Via,” *IEEE Trans. Microw. Theory Tech.*, vol. 59, no. 6, pp. 1454–1460, 2011.

[46] H. Zheng, D. Zeng, D. Yang, L. Zhang, and Z. Yu, “An accurate compact model with skin and proximity effects for high coupling-coefficient transformers,” in *2010 10th IEEE International Conference on Solid-State and Integrated Circuit Technology*, 2010, pp. 1886–1888.

[47] C. R. Paul, *Inductance: loop and partial*. John Wiley & Sons, 2011.

[48] J. S. Kim, S. H. Im, and G. S. Park, “A study on the skin effect and eddy current distributions in conductive media,” *2017 20th International Conference on Electrical Machines and Systems, ICEMS 2017*. 2017.

[49] D. Chen, Q. Ji, H. Zhang, and L. Zhao, “Application of pulsed eddy current in plate thickness evaluation,” in *2009 4th IEEE Conference on Industrial Electronics and Applications*, 2009, pp. 3286–3288.

[50] A. K. Singh, Ibraheem, and A. K. Sharma, “Parameter identification of eddy current braking sytem for various applications,” in *2014 Innovative Applications of Computational Intelligence on Power, Energy and Controls with their impact on Humanity (CIPECH)*, 2014, pp. 191–195.

[51] H.-J. Ryoo, J.-S. Kim, D.-H. Kang, G.-H. Rim, Y.-J. Kim, and C.-Y. Won, “Design and analysis of an eddy current brake for a high-speed railway train with constant torque control,” in *Conference Record of the 2000 IEEE Industry Applications Conference. Thirty-Fifth IAS Annual Meeting and World Conference on Industrial Applications of Electrical Energy (Cat. No.00CH37129)*, 2000, vol. 1, pp. 277–281 vol.1.

[52] J. Cao, Z. Yihuang, R. Li, Y. Pan, and Y. Wang, “Analysis of Eddy Current Braking Characteristics of High Speed Maglev Train Based on Dynamic Change of Skin Effect and Operating Speed,” in *2019 22nd International Conference on Electrical Machines and Systems (ICEMS)*, 2019, pp. 1–5.

[53] S. E. Gay and M. Ehsani, “Optimized design of an integrated eddy-current and friction brake for automotive applications,” in *2005 IEEE Vehicle Power and Propulsion Conference*, 2005, pp. 290–294.

[54] S. Anwar and B. Zheng, “An Antilock-Braking Algorithm for an Eddy-Current-Based Brake-By-Wire System,” *IEEE Trans. Veh. Technol.*, vol. 56, no. 3, pp. 1100–1107, 2007.

[55] K. Nagaya and Y. Karube, “A rotary eddy-current brake or damper consisting of several sector magnets and a plate conductor of arbitrary shape,” *IEEE Trans. Magn.*, vol. 23, no. 2, pp. 1819–1826, 1987.

[56] F. Chen, H. Zhao, and H. Ding, “Eddy Current Damper Design for Vibration Suppression in Robotic Milling Process,” in *2018 IEEE International Conference on Robotics and Automation (ICRA)*, 2018, pp. 799–804.

[57] A. K. Singh and Ibraheem, “Model development of eddy current brakes for Energy Absorbing System,” in *2015 International Conference on Recent Developments in Control, Automation and Power Engineering (RDCAPE)*, 2015, pp. 382–384.

[58] T. K. Kiong, H. Sunan, L. Wenyu, and Y. Shuang, “Development for precise positioning of air bearing stages,” in *2012 IEEE International Conference on Mechatronics and Automation*, 2012, pp. 1943–1948.

[59] M. Motalleb, M. Vakilian, and A. Abbaspour, “Calculation of eddy current losses caused by leads and other current sources in high current power transformers,” in *2008 Australasian Universities Power Engineering Conference*, 2008, pp. 1–6.

[60] E. Falck, M. Stoisiek, and G. Wachutka, “Modeling of parasitic inductive effects in power modules,” in *Proceedings of 9th International Symposium on Power Semiconductor*

Devices and IC's, 1997, pp. 129–132.

[61] E. A. Brink and I. W. Hofsajer, "Analytical Approach for Determining the Frequency-Dependent Characteristics of Multipath Conductive Structures," *IEEE Trans. Power Electron.*, vol. 29, no. 11, pp. 5835–5845, 2014.

[62] O. Bir, P. Bohm, K. Preis, and G. Wachutka, "Edge finite element analysis of transient skin effect problems," *IEEE Trans. Magn.*, vol. 36, no. 4, pp. 835–839, 2000.

[63] T. Asada, Y. Baba, N. Nagaoka, A. Ametani, J. Mahseredjian, and K. Yamamoto, "A Study on Basic Characteristics of the Proximity Effect on Conductors," *IEEE Trans. Power Deliv.*, vol. 32, no. 4, pp. 1790–1799, 2017.

[64] Y. Alkraimeen and P. Gomez, "On the Computation of Frequency-Dependent Core and Proximity Effects for Transient Analysis of Transformer Windings," *IEEE Trans. Power Deliv.*, vol. 34, no. 3, pp. 891–898, 2019.

[65] W. B. Kuhn and N. M. Ibrahim, "Analysis of current crowding effects in multiturn spiral inductors," *IEEE Trans. Microw. Theory Tech.*, vol. 49, no. 1, pp. 31–38, 2001.

[66] G. Antonini, A. Orlandi, and C. R. Paul, "Internal impedance of conductors of rectangular cross section," *IEEE Trans. Microw. Theory Tech.*, vol. 47, no. 7, pp. 979–985, 1999.

[67] B. T. Deboi, "On the Accuracy of Impedance Measurements and the Influence of Fixturing," University of Alabama, 2019.

[68] A. Ruehli, "Partial element equivalent circuit (PEEC) method and its application in the frequency and time domain," in *Proceedings of Symposium on Electromagnetic Compatibility*, 1996, pp. 128–133.

[69] W. Zhang, M. T. Zhang, F. C. Lee, J. Roudet, and E. Clavel, "Conducted EMI analysis of a boost PFC circuit," in *Proceedings of APEC 97 - Applied Power Electronics Conference*, 1997, vol. 1, pp. 223–229 vol.1.

[70] J. Z. Chen, L. Yang, D. Boroyevich, and W. G. Odendaal, "Modeling and measurements of parasitic parameters for integrated power electronics modules," in *Nineteenth Annual IEEE Applied Power Electronics Conference and Exposition, 2004. APEC '04.*, 2004, vol. 1, pp. 522-525 Vol.1.

[71] A. E. Ruehli, “Equivalent Circuit Models for Three-Dimensional Multiconductor Systems,” *IEEE Trans. Microw. Theory Tech.*, vol. 22, no. 3, pp. 216–221, 1974.

[72] J. L. Schanen, E. Clavel, and J. Roudet, “Modeling of low inductive busbar connections,” *IEEE Ind. Appl. Mag.*, vol. 2, no. 5, pp. 39–43, 1996.

[73] M. Kchikach, Y. S. Yuan, Z. M. Qian, and M. H. Pong, “Modeling and simulation for conducted common-mode current in switching circuits,” in *2001 IEEE EMC International Symposium. Symposium Record. International Symposium on Electromagnetic Compatibility (Cat. No.01CH37161)*, 2001, vol. 1, pp. 681–685 vol.1.

[74] W. Teulings, J. L. Schanen, and J. Roudet, “MOSFET switching behaviour under influence of PCB stray inductance,” in *IAS ’96. Conference Record of the 1996 IEEE Industry Applications Conference Thirty-First IAS Annual Meeting*, 1996, vol. 3, pp. 1449–1453 vol.3.

[75] V. Kindl, B. Skala, R. Pechanek, M. Byrtus, and K. Hruska, “Calculation of induction machine parasitic capacitances using finite element method,” in *2016 ELEKTRO*, 2016, pp. 176–179.

[76] N. Dai and F. C. Lee, “Characterization and analysis of parasitic parameters and their effects in power electronics circuit,” in *PESC Record. 27th Annual IEEE Power Electronics Specialists Conference*, 1996, vol. 2, pp. 1370–1375 vol.2.

[77] I. Kovacevic-Badstuebner, R. Stark, U. Grossner, M. Guacci, and J. W. Kolar, “Parasitic Extraction Procedures for SiC Power Modules,” in *CIPS 2018; 10th International Conference on Integrated Power Electronics Systems*, 2018, pp. 1–6.

[78] Z. Liu, X. Huang, F. C. Lee, and Q. Li, “Package Parasitic Inductance Extraction and Simulation Model Development for the High-Voltage Cascode GaN HEMT,” *IEEE Trans. Power Electron.*, vol. 29, no. 4, pp. 1977–1985, 2014.

[79] A. N. Lemmon, A. Shahabi, and K. Miskell, “Multi-branch inductance extraction procedure for multi-chip power modules,” in *2016 IEEE 4th Workshop on Wide Bandgap Power Devices and Applications (WiPDA)*, 2016, pp. 95–100.

[80] L. Deng *et al.*, “Modeling and Analysis of Parasitic Capacitance of Secondary Winding in High-Frequency High-Voltage Transformer Using Finite-Element Method,” *IEEE Trans. Appl. Supercond.*, vol. 28, no. 3, pp. 1–5, 2018.

[81] M. B. Shadmand and R. S. Balog, “FEA tool approach for determination of parasitic capacitance of the windings in high frequency coupled inductors filters,” in *2012 IEEE Power and Energy Conference at Illinois*, 2012, pp. 1–5.

[82] M. Mermet-Guyennet, A. Castellazzi, J. Fabre, and P. Ladoux, “Electrical Analysis and Packaging Solutions for High-Current Fast-Switching SiC Components,” in *2012 7th International Conference on Integrated Power Electronics Systems (CIPS)*, 2012, pp. 1–6.

[83] B. Mouawad, J. Li, A. Castellazzi, P. Friedrichs, and C. M. Johnson, “Low parasitic inductance multi-chip SiC devices packaging technology,” in *2016 18th European Conference on Power Electronics and Applications (EPE’16 ECCE Europe)*, 2016, pp. 1–7.

[84] K. Bertling, A. D. Rakic, Y. T. Yeow, A. Brawley, H. Domyo, and F. M. Rotella, “Extraction of SOS MOSFET RF equivalent circuit elements by LCR meter measurements,” *Electron. Lett.*, vol. 46, no. 12, pp. 863–864, 2010.

[85] K. Technologies, “Keysight E4980A Precision LCR meter.pdf.” .

[86] Y.-T. Yeow, “Measurement and numerical modeling of short-channel MOSFET gate capacitances,” *IEEE Trans. Electron Devices*, vol. 34, no. 12, pp. 2510–2520, 1987.

[87] H. Ishiuchi, Y. Matsumoto, S. Sawada, and O. Ozawa, “Measurement of intrinsic capacitance of lightly doped drain (LDD) MOSFET’s,” *IEEE Trans. Electron Devices*, vol. 32, no. 11, pp. 2238–2242, 1985.

[88] A. Lemmon, S. Banerjee, K. Matocha, and L. Gant, “Analysis of Packaging Impedance on Performance of SiC MOSFETs,” in *PCIM Europe 2016; International Exhibition and Conference for Power Electronics, Intelligent Motion, Renewable Energy and Energy Management*, 2016, pp. 1–8.

[89] Z. Chen, D. Boroyevich, R. Burgos, and F. Wang, “Characterization and modeling of 1.2 kv, 20 A SiC MOSFETs,” in *2009 IEEE Energy Conversion Congress and Exposition*, 2009, pp. 1480–1487.

[90] S. Sato, Y. Omura, G. Ghibaudo, L. Benea, and S. Cristoloveanu, “Detailed analysis of frequency-dependent impedance in pseudo-MOSFET on thin SOI film,” in *2018 Joint International EUROSOI Workshop and International Conference on Ultimate Integration on Silicon (EUROSOI-ULIS)*, 2018, pp. 1–4.

[91] X. Gong and J. A. Ferreira, “Extracting the parameters of a common mode EMI equivalent circuit model for a drive inverter,” in *The 2010 International Power Electronics Conference - ECCE ASIA -*, 2010, pp. 892–899.

[92] K. Technologies, “E4990A Impedance Analyzer, 20 Hz to 10/20/30/50/120 MHz.” 2018.

[93] Hoiki, “A new Series of LCR meters to meet Your Applications.pdf.” .

[94] Hoiki, “Impedance Analyzer IM7580 Series - High performance Reliability.pdf.” .

[95] T. Keysight, *Impedance Measurement Handbook “ A guide to measurement technology and techniques.”* .

[96] A. B. Menicanin, M. S. Damnjanovic, L. D. Zivanov, and O. S. Aleksic, “Improved Model of T-Type LC EMI Chip Filters Using New Microstrip Test Fixture,” *IEEE Trans. Magn.*, vol. 47, no. 10, pp. 3975–3978, 2011.

[97] M. F. Caggiano, J. Ou, S. Bulumulla, and D. Lischner, “RF electrical measurements of fine pitch BGA packages,” *IEEE Trans. Components Packag. Technol.*, vol. 24, no. 2, pp. 233–240, 2001.

[98] Y. L. Li *et al.*, “A new technique for high frequency characterization of capacitors,” in *1998 Proceedings. 48th Electronic Components and Technology Conference (Cat. No.98CH36206)*, 1998, pp. 1384–1390.

[99] T. Liu, R. Ning, T. T. Y. Wong, and Z. J. Shen, “A new characterization technique for extracting parasitic inductances of fast switching power MOSFETs using two-port vector network analyzer,” in *2017 29th International Symposium on Power Semiconductor Devices and IC’s (ISPSD)*, 2017, pp. 403–406.

[100] M. Mazzola, M. Rahmani, J. Gafford, A. Lemmon, and R. Graves, “Behavioral modeling for stability in multi-chip power modules,” in *2015 IEEE International Workshop on Integrated Power Packaging (IWIPP)*, 2015, pp. 87–90.

[101] T. Fischer, M. Albach, and G. Schubert, “Accurate Impedance Characterization with a Vector Network Analyzer,” in *2007 7th International Symposium on Electromagnetic Compatibility and Electromagnetic Ecology*, 2007, pp. 216–219.

[102] A. N. Lemmon and R. C. Graves, “Comprehensive Characterization of 10-kV Silicon Carbide Half-Bridge Modules,” *IEEE J. Emerg. Sel. Top. Power Electron.*, vol. 4, no. 4, pp. 1462–1473, 2016.

[103] E. McShane and K. Shenai, “RF de-embedding technique for extracting power MOSFET package parasitics,” in *IWIPP 2000. International Workshop on Integrated Power Packaging (Cat. No.00EX426)*, 2000, pp. 55–59.

[104] A. Lemmon and R. Graves, “Parasitic extraction procedure for silicon carbide power modules,” in *2015 IEEE International Workshop on Integrated Power Packaging (IWIPP)*, 2015, pp. 91–94.

[105] K. Technologies, “E5080B Vector Network Analyzer Note.pdf.” .

[106] L. Yang and W. G. H. Odendaal, “Measurement-Based Method to Characterize Parasitic Parameters of the Integrated Power Electronics Modules,” *IEEE Trans. Power Electron.*, vol. 22, no. 1, pp. 54–62, 2007.

[107] Z. Ariga, K. Wada, and T. Shimizu, “TDR Measurement Method for Voltage-Dependent Capacitance of Power Devices and Components,” *IEEE Trans. Power Electron.*, vol. 27, no. 7, pp. 3444–3451, 2012.

[108] H. Zhu, A. R. Hefner, and J.-. Lai, “Characterization of power electronics system interconnect parasitics using time domain reflectometry,” *IEEE Trans. Power Electron.*, vol. 14, no. 4, pp. 622–628, 1999.

[109] Tektronix, “TDR Impedance Measurements : A Foundation for Signal Integrity,” pp. 1–16, 2008.

[110] D. Smolyansky, “TDR and S-parameters performance requirements for fault isolation and serial data applications,” *2007 70th ARFTG Microwave Measurement Conference: High Power RF Measurement Techniques, ARFTG 2007*. pp. 1–4, 2018.

[111] T. Liu, R. Ning, T. T. Y. Wong, and Z. J. Shen, “A new characterization technique for extracting parasitic inductances of fast switching power MOSFETs using two-port vector network analyzer,” in *2017 29th International Symposium on Power Semiconductor Devices and IC’s (ISPSD)*, 2017, pp. 403–406.

[112] F. W. Grover, *Inductance Calculations*. Dover Publications, 2013.

[113] E. B. Rosa and F. W. Grover, “Formulas and tables for the calculation of mutual and self-inductance (Revised),” *Bull. Bur. Stand.*, vol. 8, no. 1, p. 1, 1912.

[114] C. L. Holloway and E. F. Kuester, “DC Internal Inductance for a Conductor of Rectangular Cross Section,” *IEEE Trans. Electromagn. Compat.*, vol. 51, no. 2, pp. 338–344, 2009.

[115] B. Zohuri, “The Fundamental of Electrodynamics,” 2019, pp. 351–412.

[116] W. Heinrich, “Comments on ‘Internal impedance of conductors of rectangular cross section,’” *IEEE Trans. Microw. Theory Tech.*, vol. 49, no. 3, pp. 580–581, 2001.

[117] R. Manual, “COMSOL Multiphysics® v. 5.4. www.comsol.com. COMSOL AB, Stockholm, Sweden,” 2018.

[118] M. COMSOL, “How to Choose Between Boundary Conditions for Coil Modeling,” *How to Choose Between Boundary Conditions for Coil Modeling*, 2016. [Online]. Available: https://www.comsol.com/blogs/how-to-choose-between-boundary-conditions-for-coil-modeling/.

[119] R. Weaver, “Solenoid Inductance Calculator,” *Radio Theory*, 2012. [Online]. Available: http://electronbunker.ca/eb/InductanceCalcRc.html.

[120] S. Yang, J. Soh, and R. Kim, “Parasitic Inductance Reduction Design Method of Vertical Lattice Loop Structure for Stable Driving of GaN HEMT,” in *2019 IEEE 4th International Future Energy Electronics Conference (IFEEC)*, 2019, pp. 1–8.

[121] J. Lu, H. Bai, A. Brown, M. McAmmond, D. Chen, and J. Styles, “Design consideration of gate driver circuits and PCB parasitic parameters of paralleled E-mode GaN HEMTs in zero-voltage-switching applications,” in *2016 IEEE Applied Power Electronics Conference and Exposition (APEC)*, 2016, pp. 529–535.

[122] Q. Chen, Y. Pei, X. Yang, and Z. Wang, “Analysis and Suppression of Inductive Interference in an Active Integrated Power Electronics Module,” *IEEE Trans. Components Packag. Technol.*, vol. 32, no. 4, pp. 724–733, 2009.

[123] K. Technologies, “Keysight 16047E Test Fixture Operation and Service Manual.” .

[124] M. COMSOL, “How to Model Conductors in Time-varying Magnetic Fields,” 2018. [Online]. Available: https://www.comsol.com/blogs/how-to-model-conductors-in-time-varying-magnetic-fields/.

[125] B. Krauter and S. Mehrotra, “Layout based frequency dependent inductance and resistance extraction for on-chip interconnect timing analysis,” *Proceedings - Design Automation Conference*. pp. 303–308, 1998.

APPENDIX

A.1. Some Important Vector Identities

$$A \cdot B \times C = B \cdot C \times A = C \cdot A \times B \tag{71}$$

$$A \times (B \times C) = B(A \cdot C) - C(A \cdot B)$$

$$\nabla \cdot (A \times B) = B \cdot (\nabla \times A) - A \cdot (\nabla \times B)$$

$$\nabla \cdot \nabla V = \nabla^2 V$$

$$\nabla \times \nabla \times \mathrm{A} = \nabla(\nabla \cdot \mathrm{A}) - \nabla^2 A$$

$$\nabla \times \nabla V = 0$$

$$\nabla \cdot (\nabla \times A) = 0$$

$$\int_V \nabla \cdot A dV = \oint_S A \cdot dS \qquad (Divergence\ Theorem)$$

$$\int_S \nabla \times A \cdot \, dS = \oint_c A \cdot dl \qquad (Stokes\ Theorem)$$

A.2. Derivation of Maxwell's Equations

The four basic laws which make up Maxwell's equations are: (1) Gauss's law for Electric field, (2) Gauss's law of Magnetism, (3) Faraday's law of Induction , and (4) Amperes law. A complete derivation of Maxwell's laws is provided in this section.

Gauss's Law for Electric Field

Gauss's law for electric field is used to describe the strength of the electric field around a point charge. It is the first of these sets of law and it is given mathematically as:

$$\oint_s E \cdot dA = \frac{Q_{inside}}{\varepsilon_0} \tag{72}$$

where E is the Electric field intensity in V/m, Q is the charge in Coloumbs, and ε_0 is the permittivity of free space given as $8.854 \times 10^{-12} Farads/meter$.

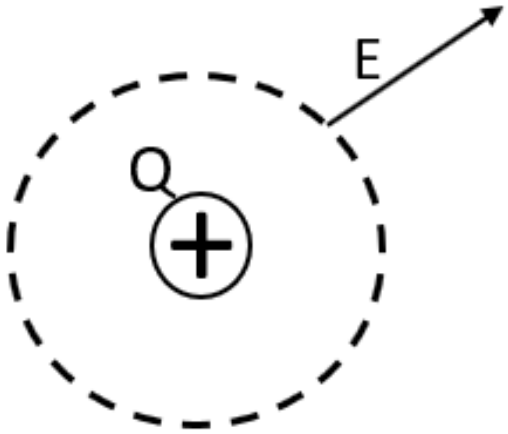

Figure 71: Demonstration of Gauss' law for electric field

Figure 71 is used to explain Gauss's law for electric field. As shown in Figure 71, a Gaussian imaginary surface is drawn around a point charge with electric field E coming out of that surface. The electric field E emanating from the surface which is perpendicular to the imaginary surface in all directions multiplied by the surface area is equal to the total charge inside the surface divided by the permittivity of free space. To convert the integral form of Equation (72) into differential form, recall the divergence theorem which is given as:

$$\oint_s F \cdot dA = \int_V \nabla \cdot F \cdot dV \tag{73}$$

Also, integrating the charge density throughout the gaussian surface yields the total charge inside the surface and given as:

$$\int_V \rho \, dV = Q_{inside} \tag{74}$$

Substituting Equation (73) and Equation (74), into the right and left-hand sides of Equation (72) yields:

$$\int_V \nabla \cdot \, E \, dV = \frac{1}{\varepsilon_0} \int_V \rho \, dV \tag{75}$$

Taking the triple derivatives of both sides of Equation (75) yields the differential form of Gauss' law for an electric field given as:

$$\nabla \cdot E = \frac{\rho}{\varepsilon_0} \tag{76}$$

where E represents the electric field intensity E in (V/m), ρ represents the charge density in coulombs per cubic meter $(C \cdot m^{-3})$, and ε_0 is the permittivity of free space given as $8.854 \times 10^{-12} Farads/meter.$

Gauss's Law of Magnetism

Gauss' law of magnetism is used to describe the strength of the magnetic field around a magnetic material, and it is given mathematically as;

$$\oint_S B \cdot dA = 0 \tag{77}$$

To explain Gaussian law of magnetism, a Gaussian surface can be drawn anywhere around the magnetic material where the magnetic field is present due to the presence of the magnet, as shown in Figure 72.

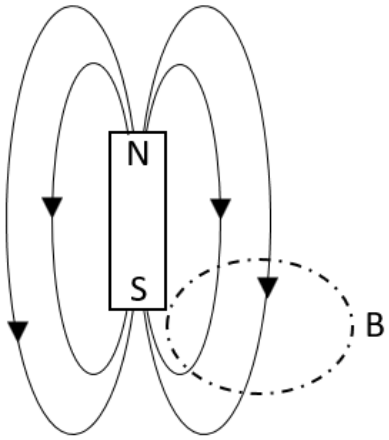

Figure 72: Demonstration of Gauss law for magnetism

The magnetic field lines move in all directions from the north pole to the south pole of the magnetic material. It is shown by this law that all the magnetic flux entering the gaussian surface is equal to the magnetic flux leaving the same surface, which results in a net flux of zero, irrespective of the location of the gaussian surface around the magnetic material.

Applying the divergence theorem of Equation (73) to Equation (77) yields:

$$\int_V \nabla \cdot B \, dV = 0 \tag{78}$$

Taking the triple derivative of both sides of Equation (78) yields:

$$\nabla \cdot B = 0 \tag{79}$$

where B is the magnetic flux density B in (Wb/m^2).

Faraday's Law of Induction

Faradays law is the most profound of the collective group of laws governing all macroscopic EM fields which are known as Maxwell's equations, according to [47]. Faraday's law is the basis for the use of electricity and all its corresponding implications. To state the

Faraday's fundamental law, consider Figure 73 in which an open surface s with a contour path c surrounding it.

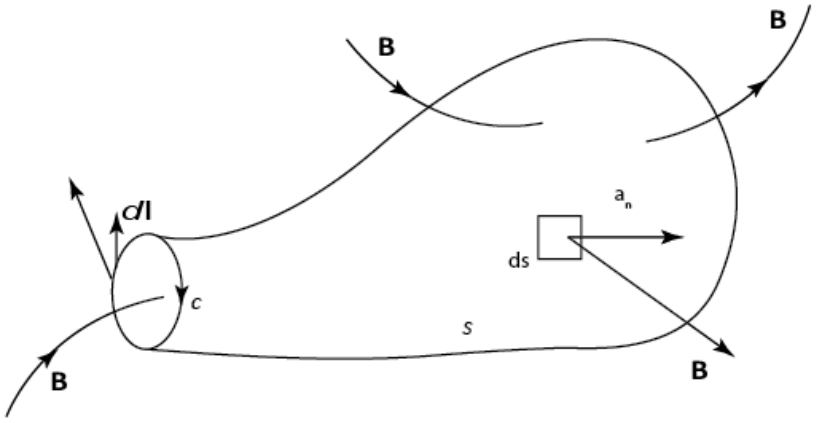

Figure 73: Demonstration of Faraday's law [47]

The voltage between two points along a specified path is the negative line integral of the electric field between the points along the path [40]. The term electromotive force (emf) is used more frequently in place of the voltage about a closed path whenever there is a contribution of changing magnetic flux.

The electromotive force emf is equal to the time rate of change of magnetic flux through the path and is given as:

$$emf \equiv -\frac{d\psi_m}{dt} \tag{80}$$

The electromotive force emf around the closed loop c is obtained as the line integral of the electric field [47] and given as:

$$emf \equiv voltage\ about\ closed\ path \equiv -\oint_c \boldsymbol{E}.d\boldsymbol{I} \tag{81}$$

And the magnetic flux which passes through the open surface s is obtained with a surface integral is given as:

$$\Phi = \int_s \mathbf{B} \cdot \mathbf{ds} \tag{82}$$

Faraday's law is thus given mathematically as:

$$\oint_c \boldsymbol{E} \cdot d\boldsymbol{I} \equiv -\frac{d\Phi}{dt} \equiv -\frac{d}{dt} \int_s \mathbf{B} \cdot \mathbf{ds} \tag{83}$$

Recall Stokes theorem given as:

$$\oint \boldsymbol{F} \cdot \boldsymbol{dI} = \int_s (\boldsymbol{\nabla} \times \boldsymbol{F}) \cdot \boldsymbol{dS} \tag{84}$$

Stokes law given above states that the surface integral of the curl of F over an open surface s is the same as the line integral of F around the contour c which encloses the open surface.

Applying Stokes theorem of Equation (84) to Equation (83), and re-writing the equation gives:

$$\int_s (\boldsymbol{\nabla} \times \boldsymbol{E}) \cdot \boldsymbol{dS} = -\int_s \frac{\boldsymbol{\partial B}}{\boldsymbol{\partial t}} \cdot \boldsymbol{dS} \tag{85}$$

Comparing both sides of Equation (85), the point form of Faradays law becomes:

$$\boldsymbol{\nabla} \times \boldsymbol{E} = -\frac{\boldsymbol{\partial}\, \boldsymbol{B}}{\boldsymbol{\partial}\, \boldsymbol{t}} \tag{86}$$

where $\nabla \times E$ gives the curl of the circulation of E at a point, E represents the electric field intensity E in (V/m), and B represents the magnetic flux density B in (Wb/m^2).

Ampere's Law

Ampere's law is stated mathematically as:

$$\oint B \cdot dl = \mu_0 I_{Enclosed} + \mu_0 \varepsilon_0 \frac{\partial}{\partial t} \oint E \cdot dA \tag{87}$$

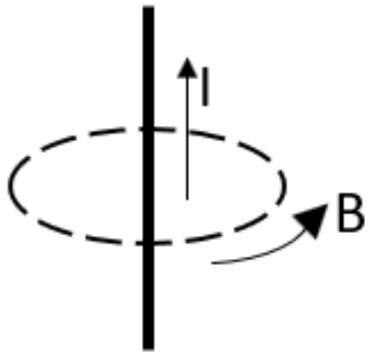

Figure 74: Demonstration of Ampere's law

Whenever there is a conductor loop carrying current, there will always be a magnetic B-field or region surrounding that loop. Equation (87) shows that the strength of the field around a conductor carrying current is proportional to the current in the wire-loop. Considering the second term of the right-hand side of Equation (87), the change of the electric flux around the conductor will also cause a change in the magnetic field.

The current enclosed ($I_{Enclosed}$) term of (87) may be expressed as the integral of the volume current density J in Amperes per meter square (A/m^2). This is expressed mathematically as:

$$I_{Enclosed} = \int_S J \cdot dS \tag{88}$$

Substituting Stokes theorem of Equation (84), and Equation (88) into Equation (87) yields:

$$\int_s (\nabla \times B) \cdot dS = \mu_0 \int_s J \cdot dS + \mu_0 \varepsilon_0 \frac{\partial}{\partial t} \int_s E \cdot dS \tag{89}$$

Taking the double derivatives of Equation (89) yields:

$$\nabla \times B = \mu_0 J + \frac{1}{c^2} \frac{\partial E}{\partial t} \tag{90}$$

where c is the speed of light in m/s and it is given by:

$$c = \frac{1}{\sqrt{(\mu_0 \varepsilon_0)}} \tag{91}$$

where μ_0 represents the permeability of free space in (*H/m*), ε_0 is the permittivity of free space given as $8.854 \times 10^{-12} Farads/meter$, B represents the magnetic flux density in (Wb/m^2), E represents the electric field intensity in (V/m), and J represents the current density in (A/m^2).

A.3. Skin-Depth Derivation

The existence of fields around the conductor carrying current implies that there would also be field penetrations into the said conductor. To determine the extent of field penetration into the conductor, take the curl of the Maxwell's third equation and apply the vector identity given in the Appendix A.1.

Maxwell's third equation is given as:

$$\nabla \times E = -j\omega B \tag{92}$$

Recall that the magnetic flux density B is related to the magnetic field intensity H by the equation:

$$\mathrm{B} = \mu \mathrm{H} \tag{93}$$

Taking the Curl of both sides of Equation (92), and using the B and H relation of Equation (93) yields:

$$\nabla \times \nabla \times E = -j\omega\, \mu \nabla \times H \tag{94}$$

Recall vector identity of Equation (95) given as:

$$\nabla \times \nabla \times \mathrm{A} = \nabla(\nabla \cdot \mathrm{A}) - \nabla^2 A \tag{95}$$

substituting the vector identity of Equation (95) into Equation (94) yields Equation (96) given as:

$$\nabla \times \nabla \times E = \nabla(\nabla \cdot \mathrm{E}) - \nabla^2 E = -j\omega\, \mu \nabla \times H \tag{96}$$

Recall from Maxwell's first law that:

$$\nabla \cdot E = 0 \tag{97}$$

Substituting Equation (97) into Equation (96), and multiplying both sides of Equation (96) by -1, yields:

$$\nabla^2 E = j\omega\mu \nabla \times H \tag{98}$$

From Maxwell's fourth equation which is given as:

$$\nabla \times \mathrm{H} = J + j\omega D \tag{99}$$

Which states that the curl of the magnetic field (H) is given as the sum of the conduction current $J = \sigma E$, and the second term of Equation (99) $j\omega D$ known as the displacement current. For good conductors and metals, the displacement current term $j\omega D$ is usually neglected. This value is small as compared to the conduction current for microwave and millimeter-wave frequencies. The displacement current term $j\omega D$ is not measurable until frequencies are in the infrared region [40].

Therefore, Equation (99) becomes:

$$\nabla \times \mathrm{H} = \sigma E \tag{100}$$

Substituting Equation (100) into the right-hand side of Equation (98) results in the Equation (101) given as:

$$\nabla^2 E = j\omega\mu\sigma E \tag{101}$$

Similarly, the current density and magnetic fields can be derived in the same manner, to yield:

$$\nabla^2 J = j\omega\mu\sigma J \tag{102}$$

$$\nabla^2 H = j\omega\mu\sigma H \tag{103}$$

The differential form of Equation (101) for electric field vector can be written as:

$$\frac{d^2 E_z}{dx^2} = j\omega\mu\sigma E_z = \tau^2 E_z \tag{104}$$

where $\tau^2 \equiv j\omega\mu\sigma$ (105)

Taking the square root of both sides of Equation (105) yields:

$$\tau \equiv \sqrt{j\omega\mu\sigma} \tag{106}$$

But $\sqrt{j} = \pm(1+j)/\sqrt{2}$

Taking the positive root of $\sqrt{j}$, Equation (106) becomes:

$$\tau = \frac{(1+j)}{\sqrt{2}}\sqrt{2\pi f\mu\sigma} \tag{107}$$

which is simplified further and given as:

$$\tau = (1+j)\sqrt{\pi f\mu\sigma} = \frac{(1+j)}{\delta} \tag{108}$$

where

$$\delta = \frac{1}{\sqrt{\pi f\mu\sigma}}\ m \tag{109}$$

The quantity δ represents the skin depth in meters (*m*), f represents the frequency in hertz (*Hz*), μ represents the permeability in (*H/m*), and σ represents the conductivity in (*S/m*).

A.4. Online Analytical Inductance prediction

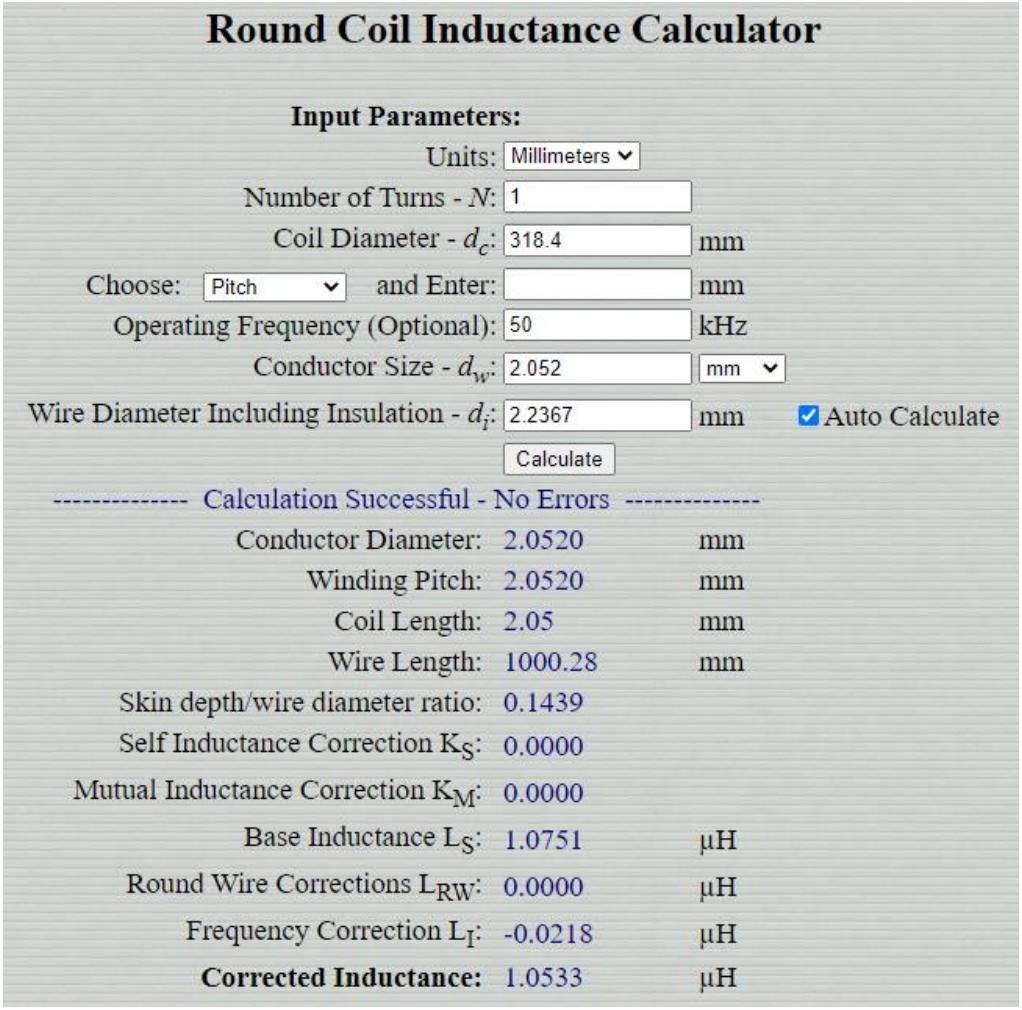

Figure 75: Online analytical prediction for one-meter loop inductor

A.5. Geometry 6 Wire Additional Plots

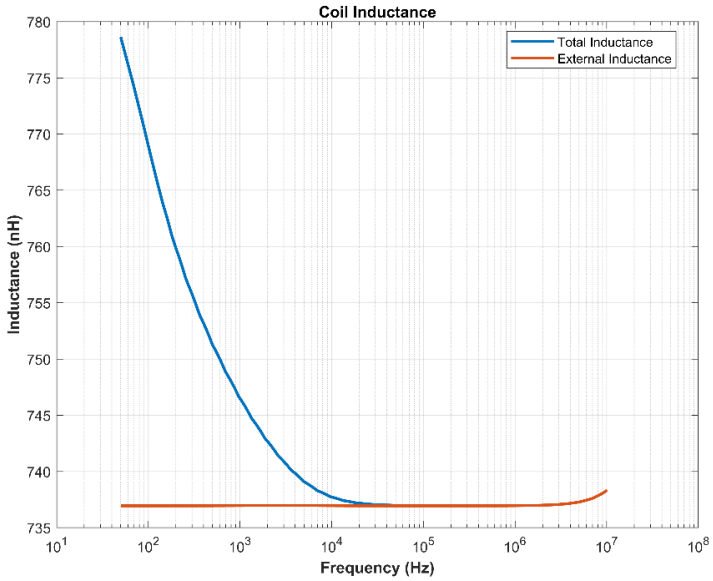

Figure 76: Total and External Inductance of the straight conductor Coil

As shown in Figure 76, the external inductance is constant across frequency, the magnitude drop of total inductance is explained solely by skin effect in the geometry.

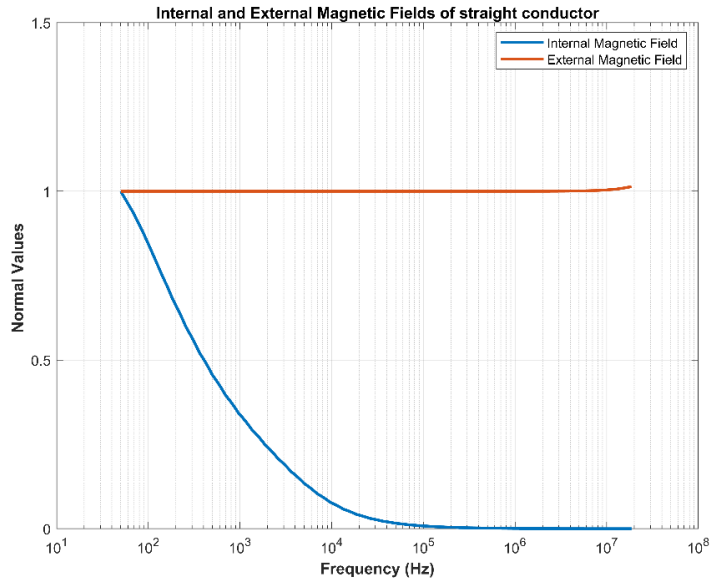

Figure 77: Normalized Magnetic field (mf.normH) Internal and External fields around the straight conductor

Similarly, the external magnetic fields of Figure 77, shows a similar trend as the external inductance trend of Figure 76, while the internal fields exhibit a similar profile to the magnitude drop in inductance. Therefore, the internal fields is solely responsible for the skin effect (skin-depth) penetration which results to the drop in internal inductance for this geometry.

A.6. Additional Test Set-up Pictures for Geometry 2

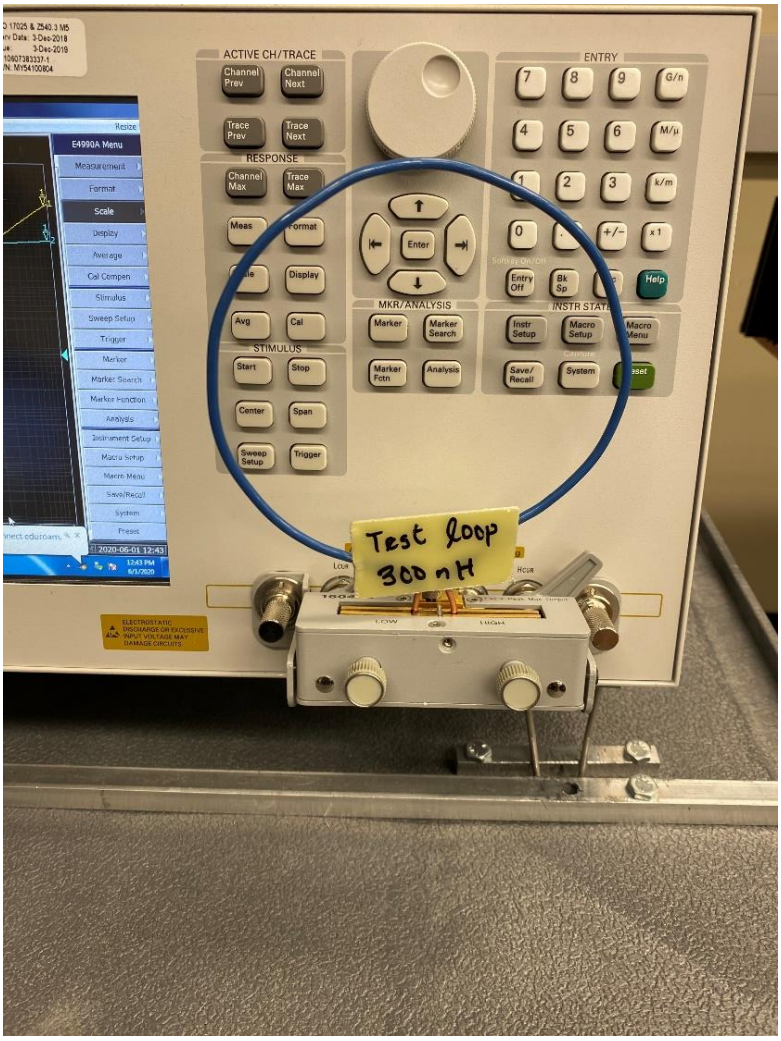

Figure 78: Empirical setup of a 300nH loop conductor

A.7. Additional Results for Geometry 8

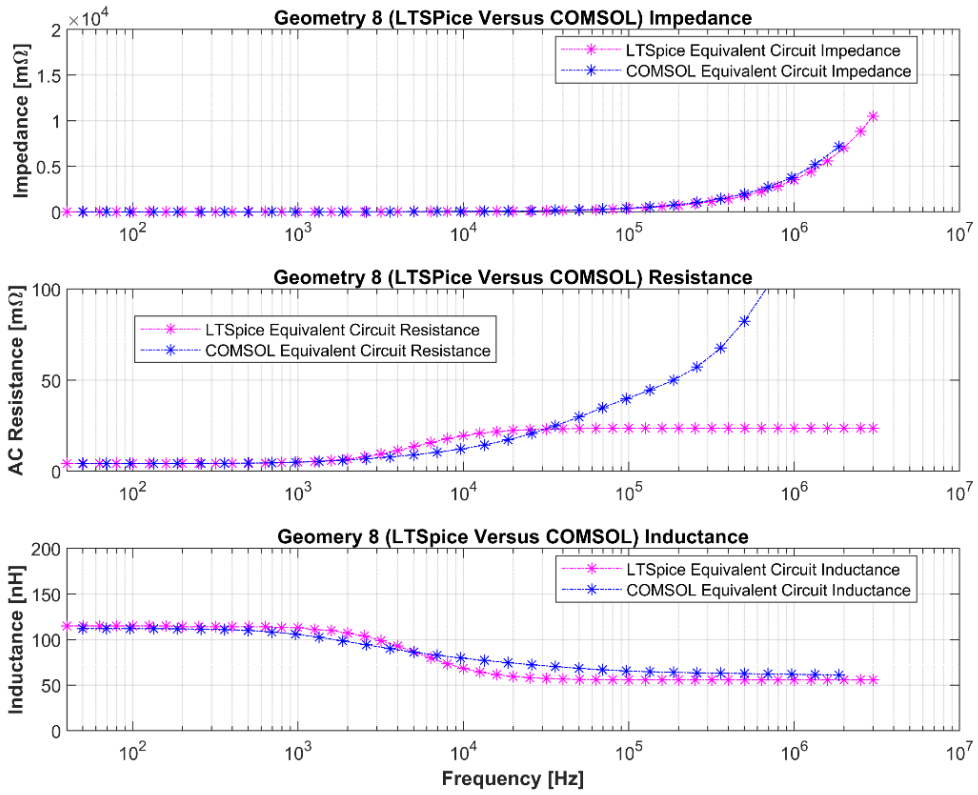

Figure 79: Geometry 8 COMSOL Versus LTSpice Simulation

Figure 79 shows a good match between the COMSOL prediction and the LTSpice simulation for the impedance of the rectangle loop (Geometry 8). The cross-over frequency also limits the high-frequency prediction of the resistance. But the inductance shows good agreement between both models from DC to high-frequency.